Silicon Photonic Devices and Circuits for Data-Center Optical Interconnects

Eslam ElFiky

Department of Electrical & Computer Engineering
McGill University
Montréal, Canada

August 2019

A thesis submitted to McGill University in partial fulfillment of the requirements of the degree of Doctor of Philosophy.

Abstract

Global IP traffic will continue to grow in the foreseeable future. Different applications are driving demand for increased capacity such as cloud based services, video streaming services, and big data. Since 2008, most Internet traffic has originated or terminated in datacenters. As a result, datacenters have experienced unprecedented traffic increases, where datacenter traffic will reach more than 20.6 zettabytes by 2021, i.e., 3-fold increase since 2016. In response to demands to support capacity increases, there are significant worldwide research and commercialization efforts that are being directed toward developing high speed intra- and inter-datacenter optical interconnects (DCIs). Different material platforms are used to build optical transceivers including the silicon photonics (SiP) platform. The SiP platform has the potential to build compact, high yield, high performance, and low cost complementary metal oxide semiconductor (CMOS) compatible transceivers.

In this thesis, we explore devices and circuits for optical DCIs. This thesis can be divided into three parts. In the first part, we develop and demonstrate passive and active SiP components which are essential in photonic integrated circuits (PICs) for optical transceivers. The first device is a 3-dB beam splitter based on multi-mode interference (MMI), where we present the device design and wafer-scale experimental results. Then, we include subwavelength gratings into an asymmetric MMI to enable compact, large bandwidth, and different splitting ratios. Using cascaded MMIs, we design a C-band polarization beam splitter for coherent PICs, where we demonstrate the advantages of using a cascaded MMI design in improving the device extinction ratio. Next, we present the detailed design and experimental results of a high yield and low insertion loss polarization splitter and rotator. Different variations of this design are demonstrated aiming at different performance metrics and operating bands. Finally, we present a variable optical attenuator based on a Mach-Zehnder interferometer structure where a substrate undercut is added to the design to enable low power consumption.

In the second part, we present PICs for 200 Gb/s and 400 Gb/s intra-datacenter optical interconnects. First, a 4-lane SiP transmitter is demonstrated based on four parallel Mach-Zehnder modulators (MZMs). The crosstalk between the four MZMs is studied using small-signal and large-signal modulation. Driving the four MZMs simultaneously, 400 Gb/s aggregate rate can be achieved using relatively low voltage swing and simple digital signal processing (DSP). Then, we explore 200 Gb/s transmitters based on dual parallel multi-electrode MZMs (MEMZMs) to generate the PAM4 signal optically which results in a better signal to noise ratio compared to the electrical generation. Finally, we exploit the other polarization dimension by demonstrating a dual-polarization transmitter in a stokes vector direct detection experiment. More than 200 Gb/s can be achieved using this transmitter which doubles the capacity used for a classical intensity modulation/direct detection system and renders a better scalable approach for bitrates beyond 400 Gb/s.

In the last part, we report system-level demonstrations targeting DCI applications. First, we present a single wavelength and polarization PAM4 transmission experiment using state of the art digital-to-analog converters (DACs), analog-to-digital converters (ADCs), and a lithium niobate MZM. Then, we present the first demonstration of a 400 Gb/s transmitter optical sub-assembly (TOSA) on the coarse wavelength division multiplexing (CWDM) grid. The TOSA performance is studied versus several parameters. Results show that we can achieve more than 600 Gb/s over 20 km of single mode fiber (SMF) without optical amplification.

Résumé

Le trafic IP mondial continuera de croître dans un avenir prévisible. Différentes applications génèrent une demande pour une capacité accrue, telles que les services en nuage, les services de streaming vidéo et le 'big data'. Depuis 2008, la majeure partie du trafic Internet provient ou se termine dans des centres de données. En conséquence, les centres de données ont connu une augmentation de trafic sans précédent, qui atteindra plus de 20.6 zettaoctets d'ici 2021, soit trois fois plus qu'en 2016. Face à la demande d'augmentation de la capacité, d'importants efforts de recherche et de commercialisation sont déployés dans le monde entier pour développer des interconnexions optiques à grande vitesse au sein et entre les centres de données (DCI). Différentes plates-formes matérielles sont utilisées pour fabriquer des émetteurs-récepteurs optiques, notamment la plate-forme photonique silicium (SiP). La plate-forme SiP a le potentiel nécessaire pour construire des émetteurs-récepteurs à haut rendement, haute performance et à faible coût compatibles avec la technologie semi-conducteur à oxyde de métal complémentaire (CMOS).

Dans cette thèse, nous explorons des composants et des circuits pour les DCI optiques. Cette thèse peut être divisée en trois parties. Dans la première partie, nous développons et démontrons des composants SiP passifs et actifs essentiels aux circuits intégrés photoniques (PIC) pour émetteurs-récepteurs optiques. Le premier composant est un séparateur de faisceau 3-dB basé sur l'interférence multimodale (MMI), pour lequel nous présentons la conception et les résultats expérimentaux à l'échelle de la plaque de silicium (wafer). Ensuite, nous incluons des réseaux sub-longueur d'onde dans un MMI asymétrique afin de permettre un format compact, une large bande passante et différents ratios de division. En utilisant des MMI en cascade, nous concevons un séparateur de polarisations dans la bande C pour les PIC cohérents, où nous démontrons les bénéfices d'une conception MMI en cascade pour améliorer le ratio d'extinction du composant. Ensuite, nous présentons la conception détaillée et les résultats expérimentaux d'un séparateur-rotateur de polarisation

haut rendement et à faible perte d'insertion. Plusieurs variantes de cette conception sont présentées, visant différentes mesures de performance et bandes d'opération. Enfin, nous présentons un atténuateur optique variable basé sur une structure d'interféromètre Mach-Zehnder, dans lequel une sous-coupe de substrat est ajoutée pour permettre une faible consommation de puissance.

Dans la seconde partie, nous présentons des circuits intégrés photoniques pour interconnexions optiques intra-centres de données à 200 Gb/s et 400 Gb/s. Tout d'abord, un émetteur SiP à quatre voies basé sur quatre modulateurs Mach-Zehnder (MZM) en parallèle est démontré. La diaphonie entre les quatre MZM est étudiée en utilisant une modulation à petite et grande amplitude. En utilisant simultanément les quatre MZM, il est possible d'atteindre un débit agrégé de 400 Gb/s en utilisant une tension de commutation d'amplitude relativement basse et un traitement de signal numérique (DSP) simple. Ensuite, nous explorons des émetteurs à 200 Gb/s basés sur des MZM à électrodes multiples double-parallèles (MEMZM) pour générer le signal PAM4 de manière optique, ce qui permet d'obtenir un meilleur rapport signal/bruit par rapport à la génération électrique. Enfin, nous exploitons l'autre dimension de la polarisation en démontrant un émetteur à double polarisation dans une expérience de détection directe basée su les vecteurs de Stokes. Cet émetteur permet d'atteindre plus de 200 Gb/s, ce qui double la capacité d'un système à modulation d'intensité/détection directe classique et constitue une approche plus extensible pour les débits binaires >400 Gb/s.

Dans la dernière partie, nous présentons des démonstrations au niveau système ciblant les applications DCI. Tout d'abord, nous présentons une expérience de transmission PAM4 à longueur d'onde et polarisation uniques utilisant des convertisseurs numérique-analogique (CNA) de pointe, des convertisseurs analogique-numérique (CAN) et un MZM de niobate de lithium. Ensuite, nous présentons la première démonstration d'un sous-ensemble d'émetteur optique (TOSA) à 400 Gb/s sur la grille de multiplexage CWDM. La performance du TOSA est étudiée par rapport à plusieurs paramètres. Les résultats démontrent qu'il est possible d'atteindre plus de 600 Gb/s sur une distance de 20 km de fibre monomode (SMF) sans amplification optique.

Acknowledgments

First, I would like to express my sincere gratitude to my supervisor Prof. David Plant for his continuous support of my research, patience, motivation, enthusiasm, and immense knowledge. His guidance helped me in all the time of research and writing of this thesis. I remember his words starting my PhD, where I had no experimental expertise, that new students are privileged to be working in a well-equipped laboratory. During my PhD journey, I have never forgot his words and consider myself extremely privileged to had a chance to work in such world-class laboratory. The experience we gain in his group is only available in a handful of research groups and even in the industry. I could not have imagined having a better working environment for my PhD study. Thank you Dave for accepting me in your group and being patient and supportive to my work.

I would like to thank my friend, and my colleague, Alireza Samani with whom I worked throughout my PhD. I consider myself lucky to work cooperatively with such a knowledgeable colleague. Thank you Ali for sharing your knowledge and being there for questions. Also, I would like to thank my friends and colleagues Mohamed Sowailem and Mohamed Osman. Mohamed Sowailem has been there for long nights to support me during my first experiments, and training me in the lab. I can't find enough words to express my gratitude. Mohamed Osman has been very helpful since my undergraduate studies with sharing ideas, explaining every detail, brainstorming, and much more. Thank you Mohameds for the great help through my entire PhD.

I would like to thank my colleague David Patel for his helpful discussions, lab support, and during tape-out deadlines. He has been very helpful and patient with lots of my questions. I would like to thank my colleague Maxime Jacques for his helpful discussions and suggestions. I would also like to thank my colleague Mathieu Chagnon for his support during my first experiment and being a critic that can help me improve. I would like to thank the rest of our group that helped me along the way: Thang Hoang, Yannick D'Mello, Rui Li, Samuil Alam, Oscar Wang, Santiago Bernal, Md Ghulam Saber, Zhenping Xing, Meng Xiang, Nicolas Abadia, Amar Kumar, Deng Mao, Luhua Xu, Heba Tamazin, and Olivier Carpentier.

I would like to express my deep appreciation and pay humble respects to my parents. I could not imagine finishing this thesis without their support especially my mother's prayers to me. Also, I would like to thank my father Prof. Ahmed El-Fiky for his encouragement and support to finish this thesis.

I would like to thank my family for their support. I would like to thank my beautiful daughters Talin El-Fiky, and Ruqayyah El-Fiky. Ruqayyah being born during my PhD was very supportive by forcing me to stay in the Lab to work more since I can't work at home. Their beautiful smiles pushed me through hard times and towards reaching my goals. Finally, I would like to thank my lovely wife Aseel Mandour for being there for me through the entire PhD. You have been very supportive and patient through hard times, I know how much you sacrificed during long nights working in the lab. I love you unconditionally.

Associated Publications

The original contributions of the research work presented in this thesis resulted in the following 11 papers [1-11] (6 journal and 5 conference papers). The contribution of the co-authors is stated for each paper below. Also, I co-authored 32 journal papers [12-43] and 25 conference papers [44-68] through the collaboration with other members of the photonics systems group at McGill University and researchers in other research groups.

Journal Articles Related to the Thesis

1. **Eslam El-Fiky**, Alireza Samani, David Patel, Maxime Jacques, Mohamed Sowailem, and David V. Plant, "A 400 Gb/s O-band silicon photonic transmitter for intra-datacenter optical interconnects," *Optics Express* **27**(7), 2019. [Editor's pick]
   I conceived the idea, performed the simulation and experiment, and wrote the paper. The coauthors contributed in discussing the idea, modulator design, and editing the paper.

2. **Eslam El-Fiky**, Maxime Jacques, Alireza Samani, Luhua Xu, Md. G. Saber, and David V. Plant, "C-band and O-band silicon photonic based low power variable optical attenuators," *IEEE Photonics Journal*, vol. 11, no. 4, 2019.
   I conceived the idea, performed the simulation and experiment, and wrote the paper. The coauthors contributed in discussing the idea, and editing the paper.

3. **Eslam El-Fiky**, Alireza Samani, Mohamed Osman, Maxime Jacques, David Patel, Md. G. Saber, Luhua Xu, Zhenping Xing, Meng Xiang, and David V. Plant, "Dual Parallel Multi-electrode Traveling Wave Mach-Zehnder Modulator for 200 Gb/s Intra-datacenter Optical Interconnects," *IEEE Photonics Journal*, vol. 11, no. 1, 2019.
   I conceived the idea, performed the simulation and experiment, and wrote the paper. The coauthors contributed in discussing the idea, modulator design, and editing the paper.

4. **Eslam El-Fiky**, Mohamed Osman, Alireza Samani, Claude Gamache, Michael H. Ayliffe, Jingsi Li, Maxime Jacques, Yun Wang, Amar Kumar, and David V. Plant, "First demonstration of a 400 Gb/s 4λ CWDM TOSA for datacenter optical interconnects," *Optics Express* **26**(16), 2018.

   I conceived the idea, performed the experiment, and wrote the paper. The coauthors contributed in the transmitter design and packaging, building the experimental setup, and editing the paper.

5. **Eslam El-Fiky**, Mohamed Osman, Mohammed Sowailem, Alireza Samani, David Patel, Rui Li, MD. G. Saber, Yun Wang, Nicolas Abadia, Yannick D'Mello, and David V. Plant, "200 Gb/s transmission using a dual-polarization O-Band silicon photonic intensity modulator for Stokes vector direct detection applications," *Optics Express* **25** (24), 2017.

   I conceived the idea, performed the simulation and experiment, and wrote the paper. The coauthors contributed in discussing the idea, modulator design, building the experimental setup, and editing the paper.

6. **Eslam El-Fiky**, Mathieu Chagnon, Mohammed Sowailem, Alireza Samani, Mohamed Osman, and David V. Plant, "168-Gb/s Single Carrier PAM4 Transmission for Intra Data Center Optical Interconnects," IEEE Photonics Technology Letters, vol. 29, 2017.

   I conceived the idea, performed the experiment, and wrote the paper. The coauthors contributed in building the experimental setup, and editing the paper.

Conference Articles Related to the Thesis

7. **Eslam El-Fiky**, Alireza Samani, Md Samiul Alam, Mohamed Sowailem, Olivier Carpentier, Maxime Jacques, Laurent Guenin, David Patel, David V. Plant, "A 4-lane 400 Gb/s silicon photonic transceiver for intra-datacenter optical interconnects,"

in *Proc. Optical Fiber Communications Conference (OFC)*, 2019.
I conceived the idea, performed the simulation and experiment, and wrote the paper. The coauthors contributed in discussing the idea, cell design, building the experimental setup, and editing the paper.

8. **Eslam El-Fiky**, Yun Wang, Santiago Bernal, Claude Gamache, Eric Panorel, Amar Kumar, Alireza Samani, Maxime Jacques, Ping-chiek Koh, David V. Plant, "High extinction ratio and broadband O-band polarization splitter and rotator on silicon-on-insulator," in *Proc. Optical Fiber Communications Conference (OFC)*, 2019.
I conceived the idea, performed the simulation and experiment, and wrote the paper. The coauthors contributed in discussing the idea, analyzing the experimental data, and editing the paper.

9. **Eslam El-Fiky**, Yannick D'Mello, Yun Wang, James Skoric, Md G. Saber, Amar Kumar, Alireza Samani, Luhua Xu, Rui Li, David Patel, and David V. Plant, "Ultra-Broadband and Compact Asymmetrical Beam Splitter Enabled by Angled Sub-Wavelength Grating MMI," in *Proc. Conference on Lasers and Electro-Optics (CLEO)*, 2018.
I conceived the idea, performed the experiment, and wrote the paper. The coauthors contributed in discussing the idea, device simulations, building the experimental setup, and editing the paper.

10. **Eslam El-Fiky**, Mohammed Sowailem, Alireza Samani, Mohamed Osman, David Patel, Mathieu Chagnon, David V. Plant, "Dual Polarization O-Band Silicon Photonic Intensity Modulator for Stokes Vector Direct Detection Systems," in *Proc. Optical Fiber Communications Conference (OFC)*, 2017.
I conceived the idea, performed the simulation and experiment, and wrote the paper. The coauthors contributed in discussing the idea, device design, building the experimental setup, and editing the paper.

11. **Eslam El-Fiky**, Alireza Samani, David Patel, David V. Plant, "A High Extinction Ratio, Broadband, and Compact Polarization Beam Splitter Enabled by Cascaded MMIs on Silicon-on-Insulator," in *Proc. Optical Fiber Communications Conference (OFC)*, 2016.

    I conceived the idea, performed the simulation and experiment, and wrote the paper. The coauthors contributed in building the experimental setup, and editing the paper.

Journal Articles Not Directly Related to the Thesis

12. Alireza Samani, **Eslam El-Fiky**, Mohamed Osman, Rui Li, David Patel, Thang Hoang, Maxime Jacques, Mathieu Chagnon, Nicolas Abadia, and David V. Plant, "Silicon Photonic Mach-Zehnder Modulator Architectures for on Chip PAM-4 Signal Generation," *Journal of Lightwave Technology*, Vol. 37, no.13, 2019.

13. Alireza Samani, **Eslam El-Fiky**, Mohamed Osman, David Patel, Rui Li, Maxime Jacques, and David V. Plant, "180 Gb/s single carrier single polarization 16-QAM transmission using an O-band silicon photonic IQM ," *Optics Express* **27**(10), 2019.

14. Md Ghulam Saber, Gemma Vall-Llosera, David Patel, Alireza Samani, Rui Li, Mohamed Morsy-Osman, Mathieu Chagnon, **Eslam El-Fiky**, Ramón Gutiérrez-Castrejón, Patryk J. Urban, Boris Dortschy, Fabio Cavaliere, Stephane Lessard, and David V. Plant, "Silicon-based optical links using novel direct detection, coherent detection and dual polarization methods for new generation transport architectures," *accepted at Optics Communications*, 2019.

15. Md Ghulam Saber, **Eslam El-Fiky**, Zhenping Xing, Mohamed Morsy-Osman, David Patel, Alireza Samani, Md Samiul Alam, Kh Arif Shahriar, Luhua Xu, Gemma Vall-Llosera, Boris Dortschy, Patryk J Urban, Fabio Cavaliere, Stephane Lessard, and David V. Plant, "25 and 50 Gb/s/λ PAM-4 Transmission Over 43 and 21 km Using

A Simplified Coherent Receiver on SOI," *IEEE Photonics Technology Letters*, vol. 31, no. 10, 2019.

16. Luhua Xu, Yun Wang, Deng Mao, **Eslam El-Fiky**, Zhenping Xing, Amar Kumar, Md Ghulam Saber, Maxime Jacques, and David V Plant, "Broadband 1310/1550-nm wavelength demultiplexer based on multimode interference coupler with tapered internal photonic crystal for the SOI platform ," *Optics Letters* **44**(13), 2019.

17. Maxime Jacques, Alireza Samani, **Eslam El-Fiky**, David Patel, Zhenping Xing, and David V Plant, "Optimization of thermo-optic phase-shifter design and mitigation of thermal crosstalk on the SOI platform ," *Optics Express* **27**(8), 2019.

18. Luhua Xu, Yun Wang, **Eslam El-Fiky**, Deng Mao, Amar Kumar, Zhenping Xing, Md Ghulam Saber, Maxime Jacques, and David V. Plant, "Compact Broadband Polarization Beam Splitter Based on Multimode Interference Coupler with Internal Photonic Crystal for the SOI Platform," *Journal of Lightwave Technology*, Vol. 37, no.4, 2019.

19. Meng Xiang, Zhenping Xing, Xueyang Li, **Eslam El-Fiky**, Mohamed Morsy-Osman, Qunbi Zhuge, and David V. Plant, "Experimental study of performance enhanced IM/DD transmissions combining 4D Trellis coded modulation with precoding," *Optics Express* **26**(25), 2018.

20. Yannick D'Mello, **Eslam El-Fiky**, James Skoric, Amar Kumar, Michael Hui, Yun Wang, Laurent Guenin, David Patel, and David V. Plant, "Compact, Angled Polarization Splitter: Characterization of Broadband Performance and Fabrication Tolerance," *IEEE Photonics Journal*, vol. 10, no. 6, 2018.

21. Md Ghulam Saber, Mohamed Osman, David Patel, Alireza Samani, **Eslam El-Fiky**, MS Alam, KA Shahriar, Zhenping Xing, Maxime Jacques, Boris Dortschy, Gemma Vall-Llosera, Patrick Urban, Fabio Cavaliere, Stephane Lessard, and David V. Plant,

"Demonstration of a 120° hybrid based simplified coherent receiver on SOI for high speed PON applications," *Optics Express* **26**(24), 2018.

22. Luhua Xu, Yun Wang, Amar Kumar, **Eslam El-Fiky**, Deng Mao, Heba Tamazin, Maxime Jacques, Zhenping Xing, Md Ghulam Saber, and David V. Plant, "Compact high-performance adiabatic 3-dB coupler enabled by subwavelength grating slot in the silicon-on-insulator platform," *Optics Express* **26**(23), 2018.

23. Nicolas Abadia, Md Ghulam Saber, Frank Bello, Alireza Samani, **Eslam El-Fiky**, Yun Wang, John F Donegan, and David V. Plant, "CMOS-compatible multi-band plasmonic TE-pass polarizer," *Optics Express* **26**(23), 2018.

24. Zhenping Xing, Alireza Samani, Meng Xiang, **Eslam El-Fiky**, Thang M Hoang, David Patel, Rui Li, Meng Qiu, Md Ghulam Saber, Mohamed Morsy-Osman, and David V. Plant,"100 Gb/s PAM4 transmission system for datacenter interconnects using a SiP ME-MZM based DAC-less transmitter and a VSB self-coherent receiver," *Optics Express* **26**(18), 2018.

25. Md Ghulam Saber, Mohamed Morsy-Osman, Michael Hui, **Eslam El-Fiky**, Gemma Vall-Llosera, Boris Dortschy, Patryk J Urban, Fabio Cavaliere, Stephane Lessard, and David V. Plant, "DSP-Free 25-Gbit/s PAM-4 Transmission Using 10G Transmitter and Coherent Amplification," *IEEE Photonics Technology Letters*, vol. 30, no. 17, 2018.

26. Maxime Jacques, Alireza Samani, David Patel, **Eslam El-Fiky**, Mohamed Morsy-Osman, Thang Hoang, Md Ghulam Saber, Luhua Xu, John Sonkoly, Michael Ayliffe, and David V. Plant, "Modulator material impact on chirp, DSP, and performance in coherent digital links: comparison of the lithium niobate, indium phosphide, and silicon platforms," *Optics Express* **26**(17), 2018.

27. Meng Xiang, Zhenping Xing, **Eslam El-Fiky**, Mohamed Morsy-Osman, Qunbi Zhuge, and David V. Plant, “Single-lane 145 Gbit/s IM/DD transmission with faster-than-Nyquist PAM4 signaling,” *IEEE Photonics Technology Letters*, vol. 30, no. 13, 2018.

28. Yun Wang, Luhua Xu, Han Yun, Minglei Ma, Amar Kumar, **Eslam El-Fiky**, Rui Li, Nicolas Abadia Calvo, Lukas Chrostowski, Nicolas A. F. Jaeger, and David V. Plant, “Polarization-Independent Mode-Evolution-Based Coupler for the Silicon-on-Insulator Platform,” *IEEE Photonics Journal*, vol. 10, no. 33, 2018.

29. Mohamed Morsy-Osman, Mohammed Sowailem, **Eslam El-Fiky**, Tristan Goodwill, Thang Hoang, Stephane Lessard, and David V. Plant, “DSP-free ‘coherent-lite’ transceiver for next generation single wavelength optical intra-datacenter interconnects,” *Optics Express* **26**(7), 2018.

30. Rui Li, David Patel, **Eslam El-Fiky**, Alireza Samani, Zhenping Xing, Yun Wang, and David V. Plant, “56 Gb/s DAC-less and DSP-free PAM-4 Based on Silicon Photonic Dual-drive Michelson Interferometric Modulator,” *Optics Express* **26**(5), 2018.

31. Luhua Xu, Yun Wang, Amar Kumar, David Patel, **Eslam El-Fiky**, Zhenping Xing, Rui Li, and David V. Plant, “Polarization Beam Splitter Based on A MMI Coupler with SWGs Birefringence Engineering on SOI”, *IEEE Photonics Technology Letters*, vol. 30, no. 4, 2018.

32. Md Ghulam Saber, Yun Wang, **Eslam El-Fiky**, David Patel, Kh Arif Shahriar, MD Samiul Alam, Maxime Jacques Zhenping Xing, Luhua Xu, Nicolas Abadia, and David V. Plant, “Transversely Coupled Fabry-Perot Resonators with Bragg Grating ReflectorsI,” *Optics Letters* **43**, 2017.

33. Thang M. Hoang, Mohammed Sowailem, Qunbi Zhuge, Zhenping Xing, Mohamed Morsy-Osman, **Eslam El-Fiky**, Sujie Fan, Meng Xiang, and David V. Plant, “Single

wavelength 480 Gb/s direct detection over 80km SSMF enabled by Stokes Vector Kramers Kronig transceiver," *Optics Express* **25**(26), 2017.

34. Rui Li, David Patel, Alireza Samani, **Eslam El-Fiky**, Yun Wang, Zhenping Xing, Luhua Xu, and David V. Plant, "Analysis and Experimental Study of a Silicon Photonic Single MRM-Assisted MZI PAM-4 Modulator," *IEEE Photonics Journal*, vol. 9, no. 6, 2017.

35. Yun Wang, Luhua Xu , Amar Kumar, Yannick D'Mello, David Patel, Zhenping Xing, Rui Li, Md Ghulam Saber, **Eslam El-Fiky**, and David V. Plant,"Compact Single-Etched Sub-wavelength Grating Couplers for O-Band Application", *Optics Express* **25** (24), 2017.

36. Kuo Zhang, Qunbi Zhuge, Haiyun Xin, Mohamed Morsy-Osman, **Eslam El-Fiky**, Lilin Yi, Weisheng Hu, and David V. Plant,"Intensity directed equalizer for the mitigation of DML chirp induced distortion in dispersion unmanaged C-band PAM transmission," *Optics Express* **25** (23), 2017.

37. Mohammed Sowailem, **Eslam El-Fiky**, Mohamed Osman, Qunbi Zhuge, Thang M. Hoang, Stephane Paquet, Carl Paquet, Ian Woods, Odile Liboiron-Ladouceur, and David V. Plant, "Self-Homodyne System for Next generation Intra-Datacenter Optical Interconnects," *Optics Express* **25** (22), 2017.

38. Rui Li, David Patel, Alireza Samani, **Eslam El-Fiky**, Zhenping Xing, Mohamed Morsy-Osman, and David V. Plant, "Silicon Photonic Ring-assisted Mach-Zehnder Interferometer for 50 Gb/s DAC-less and DSP-free PAM-4 Transmission," *IEEE Photonics Technology Letters*, vol. 29, no. 12, 2017.

39. Rui Li, David Patel, **Eslam El-Fiky**, Alireza Samani, Zhenping Xing, Mohamed Morsy-Osman, and David V. Plant, "High-speed low-chirp PAM-4 transmission based on push-pull silicon photonic microring modulators," *Optics Express* **25** (12), 2017.

40. Alireza Samani, David Patel, Mathieu Chagnon, **Eslam El-Fiky**, Rui Li, Maxime Jacques, Nicolas Abadia, Venkat Veerasubramanian, and David V. Plant, "Experimental parametric study of 128 Gb/s PAM-4 transmission system using a multi-electrode silicon photonic Mach Zehnder modulator," *Optics Express* **25** (12), 2017.

41. Md Ghulam Saber, Zhenping Xing, David Patel, **Eslam El-Fiky**, Nicolas Abadia, and David V. Plant, "A CMOS Compatible Ultracompact Silicon Photonic Optical Add-Drop Multiplexer with Misaligned Sidewall Bragg Gratings," *IEEE Photonics Journal*, vol. 9, no. 3, 2017.

42. Rui Li, David Patel, Alireza Samani, **Eslam El-Fiky**, Zhenping Xing, Mohammed Sowailem, Quihang Zhong, and David V. Plant, "A 80 Gb/s silicon photonic modulator based on the principle of overlapped resonances," *IEEE Photonics Journal*, vol. 9, no. 3, 2017.

43. Alireza Samani, V. Veerasubramanian, **Eslam El-Fiky**, David Patel, and David V. Plant, "A Silicon Photonic PAM-4 Modulator Based on Dual-Parallel Mach–Zehnder Interferometers," *IEEE Photonics Journal*, vol. 8, no.1, 2016.

Conference Articles Not Directly Related to the Thesis

44. Alireza Samani, Olivier Carpentier, **Eslam El-Fiky**, Maxime Jacques, Amar Kumar, Yun Wang, Claude Gamache, Ping-chiek Koh, David V. Plant, "Highly Sensitive, 112 Gb/s O-band Waveguide Coupled Silicon-Germanium Avalanche Photodetectors," in *Proc. Optical Fiber Communications Conference (OFC)*, 2019.

45. Zhenping Xing, David Patel, **Eslam El-Fiky**, Meng Xiang, Rui Li, Md Ghulam Saber, Luhua Xu, Michael Hui, David V. Plant, "SiPh Self-coherent Transmitter Circuit with on-chip CSPR Control Capability based on a Tunable Power Splitter," in *Proc. Optical Fiber Communications Conference (OFC)*, 2019.

46. Yannick D'Mello, **Eslam El-Fiky**, James Skoric, Yun Wang, Amar Kumar, David Patel, David V. Plant, "Extremely compact and broadband polarization beam splitter enabled by customized port angles," in *Proc. Laser Science Conference*, 2018.

47. Thang Hoang, Qunbi Zhuge, Zhenping Xing, Mohamed Sowailem, Mohamed Morsy-Osman, Meng Xiang, **Eslam El-Fiky**, Sujie Fan, and David V. Plant, "Direct Detection Optical Transmission Systems Employing Stokes Vector Kramers Kronig Transceivers," in *Proc. Signal Processing in Photonic Communications conference (SPPCOM)*, 2018.

48. Heba Tamazin, **Eslam El-Fiky**, Yun Wang, Yannick D'Mello, and David V. Plant, "Ultra-broadband Compact Adiabatic Coupler in Silicon-on-Insulator for Joint Operation in the C- and O-Bands," in *Proc. Conference on Lasers and Electro-Optics (CLEO)*, 2018.

49. **Eslam El-Fiky**, Peter De Heyn, Mohamed Osman, Ashwyn Srinivasan, Alireza Samani, Marianna Pantouvaki, Mohammed Sowailem, Joris Van Campenhout, David V. Plant, "112 Gb/s PAM4 Transmission over 2 km SMF Using a C-band GeSi Electro-Absorption Modulator," in *Proc. Optical Fiber Communications Conference (OFC)*, 2018.

50. Zhenping Xing, David Patel, Thang M. Hoang, Meng Qui, Rui Li, **Eslam El-Fiky**, Meng Xiang, David V. Plant, "100 Gb/s 16-QAM Transmission over 80 km SSMF Using Silicon Photonic Modulator Enabled VSB-IM/DD System," in *Proc. Optical Fiber Communications Conference (OFC)*, 2018.

51. Rui Li, David Patel, **Eslam El-Fiky**, Alireza Samani, Zhenping Xing, Yun Wang, David V. Plant, "56 Gb/s DAC-less and DSP-free PAM-4 Based on Silicon Photonic Dual-drive Michelson Interferometric Modulator," in *Proc. Optical Fiber Communications Conference (OFC)*, 2018.

52. Kuo Zhang, Qunbi Zhuge, Haiyun Xin, Mohamed Osman, **Eslam El-Fiky**, Lilin Yi, Weisheng Hu, and David V. Plant,"Intensity-directed Equalizer for Chirp Compensation Enabling DML-based 56Gb/s PAM4 C-band Delivery over 35.9km SSMF," in *Proc. European Conference on Optical Communication (ECOC)*, 2017.

53. Yannick D'Mello, James Skoric, **Eslam El-Fiky**, David Patel, David V. Plant, "Numerical analysis and optimization of a multi-mode interfernce based polarization beam splitter," in *Proc. COMSOL Conference*, 2017.

54. Yun Wang, Luhua Xu, Amar Kumar, David Patel, Zhenping Xing, Rui Li, Md Ghulam Saber, Yannick D'Mello, **Eslam El-Fiky**, and David V. Plant, "Broadband subwavelength grating coupler for O-band application", in *Proc. Group IV Photonics (GFP)*, 2017.

55. Yun Wang, Luhua Xu, Amar Kumar, David Patel, Zhenping Xing, Rui Li, Md Ghulam Saber, Yannick D'Mello, **Eslam El-Fiky**, and David V. Plant, "O-Band Sub-Wavelength Grating Coupler", in *Proc. IEEE Photonics Conference (IPC)*, 2017.

56. Nicolas Abadia, Xiangyang Dai, Qiaoyin Lu, Wei-Hua Guo, **Eslam El-Fiky**, David V. Plant, and John F. Donegan, "Novel Polarization Beam Splitter Based on p-i-n Structure for an Indium Phosphide Platform," in *Proc. International Conference on Transparent Optical Networks (ICTON)*, 2017. [Invited]

57. Md Ghulam Saber, **Eslam El-Fiky**, David Patel, Mohamed Morsy-Osman, David V. Plant, Gemma Vall-llosera, Patryk J Urban, and Boris Dortschy, "A silicon-on-insulator 120^o Optical hybrid based on 3x3 multimode interference coupler ," in *Proc. Photonics North*, 2017.

58. Rui Li, David Patel, **Eslam El-Fiky**, Zhenping Xing, Luhua Xu, David V. Plant, "A C-band push-pull dual-ring silicon photonic modulator for 20 km SSMF transmission

without CD compensation," in Proc. *Conference on Lasers and Electro-Optics (CLEO)*, 2017. [Invited]

59. Md Ghulam Saber, Zhenping Xing, **Eslam El-Fiky**, David Patel, Luhua Xu, Nicolas Abadia, and David V. Plant, "Transversely Coupled Fabry-Perot Resonators in SOI," in *Proc. Conference on Lasers and Electro-Optics (CLEO)*, 2017.

60. Md Ghulam Saber, Zhenping Xing, David Patel, **Eslam El-Fiky**, Nicolas Abadia, Yun Wang, and David V. Plant, "A Compact Optical Add-Drop Multiplexer with Misaligned Sidewall Bragg Gratings in a Mach-Zehnder Interferometer in SOI," in *Proc. Conference on Lasers and Electro-Optics (CLEO)*, 2017.

61. Luhua Xu, Yun Wang, David Patel, **Eslam El-Fiky**, Zhenping Xing, Rui Li, Md Ghulam Saber, Maxime Jacques, and David V. Plant, "Polarization-Independent Adiabatic 3-dB Couplers for Silicon-on-Insulator," in *Proc. Conference on Lasers and Electro-Optics (CLEO)*, 2017.

62. Alireza Samani, Mathieu Chagnon, **Eslam El-Fiky**, David Patel, Maxime Jacques, Venkat Veerasubramanian, David V. Plant, "Silicon Photonics Modulator Architectures for Multi-Level Signal Generation and Transmission ," in *Proc. Optical Fiber Communications Conference (OFC)*, 2017.

63. Rui Li, Alireza Samani, **Eslam El-Fiky**, David Patel, Qiuhang Zhong, David V. Plant, "56-Gbps OOK Transmission Using Silicon Microring Assisted Mach-Zehnder Interferometer," in *Proc. Conference on Lasers and Electro-Optics (CLEO)*, 2016.

64. **Eslam El-Fiky**, Ziad A. El-Sahn, Hossam M. H. Shalaby, "WDM-IDMA Solution for NG-PON2 Enabled by Coherent Technology and Colorless ONUs," in *Proc. IEEE Conference on Photonics (IPC)*, 2014.

65. **Eslam El-Fiky**, Ziad A. El-Sahn, Hossam M. H. Shalaby, "Coherent PONs for

Next Generation Access: OIDMA versus OCDMA," in *Proc. IEEE International Conference on Computing, Networking and Communications (ICNC)*, 2014.

66. **Eslam El-Fiky**, Ziad A. El-Sahn, Hossam M. H. Shalaby, "Coherent Long Reach OIDMA-PONs Enabled By Electronic Dispersion Compensation," in *Proc. Asia communications and photonics conference (ACP)*, 2013.

67. **Eslam El-Fiky**, A. M. Morsy, Ziad A. El-Sahn, Hossam M. H. Shalaby,"Coherent OIDMA technique for next generation long reach PONs," in *Proc. Conference on Lasers and Electro-Optics (CLEO)*, 2013.

68. Ahmed M. Morsy, **Eslam El-Fiky**, Hossam M. H. Shalaby, "Performance Analysis and Comparison of Optical IDMA and Optical CDMA Techniques Using Unipolar Transmission Scheme," in *Proc. IEEE European Conference on Network and Optical Communications (NOC)*, 2013.

Contents

Abstract **i**

Résumé **iii**

Acknowledgments **vi**

Associated Publications **viii**

Contents **xxiv**

List of Figures **xxxi**

List of Tables **xxxii**

List of common acronyms **xxxiii**

1 Introduction **1**

1.1 Motivation 1

1.2 Organization of the Thesis 4

1.3 Original contributions 5

2 Introduction to the silicon photonics platform **10**

2.1 Overview 10

2.2 Laser source 13

2.3 Passive components 14
2.4 Active components 17
2.4.1 Modulators 17
2.4.2 Photo-detectors 19

3 Passive and active silicon photonic devices 21
3.1 Overview 21
3.2 O-band MMI 3-dB splitter 22
3.2.1 Introduction 22
3.2.2 Design and simulation results 22
3.2.3 Device fabrication and experimental results 24
3.3 Asymmetric MMI splitter 27
3.3.1 Introduction 27
3.3.2 Design and Simulation Results 28
3.3.3 Fabrication and Experimental Results 31
3.4 C-Band Polarization Beam Splitter 32
3.4.1 Introduction 32
3.4.2 Design and Simulation Results 33
3.4.3 Fabrication and Experimental Results 34
3.5 High yield and broadband polarization splitter and rotator 36
3.5.1 Introduction 36
3.5.2 Device design and Simulation results 36
3.5.3 Device fabrication and experimental results 40
3.5.4 Wafer-level experimental results 42
3.6 Low power variable optical attenuators 43
3.6.1 Introduction 43
3.6.2 Design and simulation results 44
3.6.3 Device fabrication 45

3.6.4 Experimental setup and results 46
3.7 Conclusion 52

4 Active silicon photonic integrated circuits for intra-datacenter optical interconnects 54

4.1 Introduction 54
4.2 A 400 Gb/s O-band silicon photonic transmitter for intra-datacenter optical interconnects 57
4.2.1 Design and fabrication 57
4.2.2 DC and small-signal characterization 59
4.2.3 Large-signal experimental setup and results 61
4.3 Dual Parallel Multi-electrode Traveling Wave Mach-Zehnder Modulator for 200 Gb/s Intra-datacenter Optical Interconnects 68
4.3.1 Design and fabrication 68
4.3.2 DC and small-signal characterization 69
4.3.3 Large-signal experimental setup 72
4.3.4 Large-signal experimental results 73
4.4 200 Gb/s DP-PAM transmitter with SV-DD 76
4.4.1 Device design 77
4.4.2 DC characterization, and small-signal characterization 77
4.4.3 Experimental setup 79
4.4.4 Experimental Results 81
4.5 Conclusion 89

5 System Level PAM4 demonstrations 91

5.1 Overview 91
5.2 Single polarization and wavelength PAM4 demonstration in the O-band . . 91
5.2.1 Motivation 91

5.2.2 Experimental Setup . . . 92
5.2.3 Results and Discussion . . . 94
5.3 400 Gb/s CWDM-TOSA . . . 97
5.3.1 Motivation . . . 97
5.3.2 Experimental setup . . . 99
5.3.3 Experimental results . . . 101
5.4 Conclusion . . . 106

6 Conclusion and Future Work 108
6.1 Overview . . . 108
6.2 Summary of original contributions . . . 108
6.2.1 Passive and active silicon photonic devices . . . 110
6.2.2 Active silicon photonic circuits . . . 112
6.2.3 System-level demonstrations . . . 113
6.3 Future Work . . . 115
6.3.1 Short term research . . . 115
6.3.2 Long term research . . . 116

References 118

List of Figures

2.1 Silicon photonic technology cross-section. 11
2.2 Material refractive index for (a) silicon and (b) silicon-dioxide. 11
2.3 PIC schematics for IM/DD based transceivers 12
2.4 PIC schematics for coherent based transceivers 13
2.5 TE mode optical field at 1550 nm for (a) channel and (b) rib waveguides. . 14
2.6 Effective refractive index for channel waveguide at (a) 1550 nm and (b) 1310 nm. 15
2.7 Effective refractive index for rib waveguides at (a) 1550 nm and (b) 1310 nm. 16
2.8 (a) Effective refractive index and (b) group index for rib waveguides at 1310 nm. 16
2.9 Loss per 90° bend for the fundamental TE mode in channel and rib waveguides. 17
2.10 Schematics for the (a) TWMZM cross-section and (d) PD cross section. . . 19
2.11 (a) PD responsivity and (b) Opto-electric bandwidth of the PD. 20

3.1 Schematic layout for the designed MMI. 22
3.2 Field profile propagation through (a) 1×N MMI and (b) 2 × 2 MMI. . . . 23
3.3 (a) Simulated transmission versus wavelength and (b) power imbalance between both ports of the MMI. 24
3.4 Schematic layout for the MZI test structure. 25

3.5 (a) Transmission spectrum measurements for both ports of the MZI, and (b) extracted splitting ratio for a single MMI. 26
3.6 (a) Image of the fabricated wafer, and (b) mean splitting ratio over the entire wavelength range across the wafer. 27
3.7 Proposed SWG-AMMI schematic. 28
3.8 L_π versus wavelength for a conventional MMI and the proposed SWG MMI. 29
3.9 Field-profile propagation through the AMMI using FDTD solver for different L_{cut} values. 30
3.10 (a) Simulated excess loss for the AMMI versus wavelength, and (b) simulated splitting ratio wavelength dependence for different L_{cut} values. 30
3.11 (a) Measured splitting ratio versus L_{cut} length., and (b) Splitting ratio wavelength dependence for different L_{cut} values over 100 nm bandwidth. 31
3.12 Proposed PBS schematic. 33
3.13 Field propagation through the PBS using EME solver for (a) TE, and (b) TM Polarized inputs. 34
3.14 Transmission spectrum measurements of the PBS for the (a) upper port and (b) lower port. 35
3.15 Schematic for the designed PSR. 36
3.16 The effective refractive index evolution through the first section of the polarization rotator for the first four modes versus waveguide rib width and slab width at (a) 1310 nm and (b) 1550 nm wavelengths. 37
3.17 Field propagation through the PSR at 1310 nm for (a) TE0 mode launch and (b) TM0 mode launch. 38
3.18 Mode profile evolution from a TM0 mode at the input to a TE0 mode at the output lower port. 38
3.19 Simulated transmission spectrum for the (a) upper port and (b) lower port of the C-band PSR. 39

3.20 Simulated tolerance for the (a) upper port and (b) lower port of the C-band PSR for the nominal design and two corner cases. 39
3.21 Transmission spectrum for the (a) upper port and (b) lower port of the C-band PSR without the clean-up filter. 40
3.22 Transmission spectrum for the (a) upper port and (b) lower port of the C-band PSR with the clean-up filter 41
3.23 Transmission spectrum for the (a) upper port and (b) lower port of the O-band PSR. 42
3.24 Wafer-level ER for the (b) upper port and (c) lower port. 43
3.25 (a) Layout schematic of the VOA and (b) transmission versus wavelength for different 3-dB couplers. 45
3.26 (a) Thermo-optic phase shifter cross-section and (b) image showing the fabricated VOA with the substrate undercut. 45
3.27 Experimental setup for the VOA testing. 46
3.28 Transmission of the VOA with and without the substrate undercut versus (a) applied voltage and (b) power consumption. 47
3.29 (a) Attenuation versus power consumption and (b) bandwidth of the VOA for the designs with and without the substrate undercut. 47
3.30 Transmission versus wavelength of the VOA (a) with substrate under cut and (b) without the substrate undercut. 48
3.31 (a) IV characteristics of the VOA and (b) attenuation versus power consumption for different thermal phase-shifter widths. 49
3.32 (a) IV characteristics of the VOA and (b) attenuation versus power consumption for different thermal phase-shifter lengths. 50
3.33 VOA bandwidth versus (a) metal heater width and (b) metal heater length. 51
3.34 (a) Bandwidth with and without the undercut, (b) attenuation versus power consumption, and (c) transmission versus wavelength for the O-band VOA. 51

4.1 (a) Layout schematic for the SiP transmitter, (b) image of the die wirebonded to a chip carrier, and (c) TWMZM cross-section. 58

4.2 (a) EE S_{11} response for the four modulators, (b) and (c) EO S_{21} response for the MZMs at 0 V and 3 V DC bias, respectively, and (d) EO crosstalk between MZM1 (aggressor) and MZM2-4 (victims). 60

4.3 Experimental setup used for the 400G PSM transmitter testing. Inset: 53 Gbaud PAM4 RF signal out of the amplifier. 61

4.4 (a) BER performance versus number of receiver FFE taps for different symbol rates, (b) BER performance versus driving voltage swing without crosstalk, (c) crosstalk impact on BER performance at different symbol rates, and (d) BER performance versus bitrate for a single lane in presence of crosstalk over different reach values at constant received signal power. 63

4.5 Eye diagrams for the four MZMs simultaneously modulated obtained after receiver DSP at 100 Gb/s net rate. 65

4.6 (a) BER versus bitrate for the four MZMs simultaneously modulated in the B2B case, and (b) BER versus received signal power with and without presence of crosstalk from other lanes. 66

4.7 (a) BER versus bitrate for different modulation formats in the B2B case, and (b-c) eye diagrams after receiver DSP for PAM2, PAM4 and PAM8 modulation formats running at 53, 53, and 35 Gbaud, respectively. 67

4.8 (a) Layout schematic for the SiP transmitter, and (b) image of the DC wirebonds and ball bumps on the 50-ohm terminations. 69

4.9 (a) Extracted phase shift versus power consumption for the thermo-optic phase shifter and (b) extracted phase shift versus DC voltage for the MEMZM's pn junction. 70

4.10 (a) Electrical S_{11} response for the fours segments, (b) EO crosstalk between both MEMZMs, and (c) EO S_{21} response for both MEMZMs at 0 V and 3 V DC bias voltages. 71
4.11 Experimental setup used to test the SiP modulator. Inset: 53 Gbaud binary signal out of the RF amplifier. 72
4.12 BER performance versus (a) number of receiver FFE taps for MEMZM2, (b) received signal powers for both MEMZMs, (c) driving voltage swing on both segments of MEMZM2, and (d) MEMZM1 crosstalk voltage swing on MEMZM2. 74
4.13 BER performance versus (a) MEMZM1 crosstalk voltage swing at different driving voltage swing for MEMZM2, and (b) bitrate over different reaches at constant received signal power where both MEMZMs are simultaneously operated. 75
4.14 SiP transmitter schematic 77
4.15 (a) and (b) Transmission spectra for upper modulator diodes, (c) phase shift versus bias voltage for upper modulator diodes, (d) and (e) transmission spectra for lower modulator diodes, and (f) phase shift versus bias voltage for lower modulator diodes 78
4.16 (a) EO S_{21} for the upper modulator, (b) EO S_{21} for the lower modulator, and (c) EE S_{11} for both modulators at 1.5 V. 79
4.17 Experimental setup used to test the SiP modulator. 80
4.18 BER and SNR performance for the 112 Gb/s DP-PAM2 signal versus received power for (a-b) the B2B case at different SOPs and (c-d) over different reaches at random SOP. 82
4.19 BER and SNR performance for the 168 Gb/s DP-PAM4 signal versus received power for the (a-b) B2B case at different SOPs and (c-d) random SOP over different reaches. 83

4.20 Eye diagrams for PAM2 and PAM4 modulation formats obtained after receiver DSP at different bitrates and reaches. 85
4.21 (a) BER versus bitrate for PAM2 and PAM4 modulation formats for B2B, 2 km, and 10 km reaches, and (b) BER versus bitrate for PAM4 modulation format using 6×2 and 4×2 MIMO. 87

5.1 Experimental setup block diagram. Insets: (a) Transmitter DSP, (b) Receiver DSP, and (c) 84 Gbaud PAM4 eye diagram of the RF signal driving the MZM. 93
5.2 (a) B2B BER performance versus bitrate for PAM4 modulation format at 10 dBm received power. (b) 84 Gbaud PAM2 and PAM4 eye diagrams. . . 94
5.3 (a) 84 Gbaud PAM4 B2B BER performance versus number of FFE filtering taps for different received signal power, and (b) BER versus received power for 84 and 88 Gbaud NRZ and PAM4 modulation formats in the B2B configuration. 95
5.4 BER versus reach for 84 and 88 Gbaud PAM4 at (a) 9.5 dBm launch power to the SMF, and (b) 8 dBm received signal power. 96
5.5 (a) An image for the TOSA soldered to the RF board in the test bed, and (b) experimental setup used for the 400G CWDM-TOSA testing. Insets: 53 Gbaud RF signal out of the amplifier, and optical spectrum out of the TOSA. 99
5.6 (a) Light-current characteristics, and (b) measured optical spectra for the four CWDM lasers. 101
5.7 (a)-(h) Optical eye diagrams for the four received lanes at the demultiplexer output equalized using a 5 tap FFE on the digital sampling oscilloscope in the B2B (top) and 2 km (bottom) cases. 101

5.8 (a) BER performance versus received OMA for the four lanes running at 53 Gbaud each in the B2B case equalized using a 5 tap FFE, and (b) BER performance versus received OMA for the four lanes running at 64 Gbaud each in the B2B case equalized using a 5 tap FFE. 102
5.9 (a) BER performance for all lanes running at 400 Gb/s aggregate net rate over different reaches using 5 tap receiver FFE, and (b) 75 Gbaud per lane (600 Gb/s) BER performance over different reaches using 11 tap FFE. . . 103
5.10 (a) BER performance versus number of receiver FFE taps for lane 0 running at 75 Gbaud in the B2B and 10 km cases, and (b) BER versus bitrate using 5 and 31 receiver FFE taps at -5 dBm received signal power for lane 0. . . 104
5.11 (a) BER versus bitrate after 40 km reach using 31 FFE taps, and (b) BER versus TOSA case temperature at constant received signal power for 400 Gb/s net rate over 10 km reach. 104
5.12 BER versus (a) baud rate and (b) bitrate for different modulation formats over different reaches, and (c) eye diagrams after receiver DSP for PAM4 and PAM8 modulation formats running at 53 and 35 Gbaud, respectively. . 105

6.1 Summary of original contributions. 109
6.2 Dual Polarization DAC-less PAM4 transmitter 116

List of Tables

3.1 Dimensions of the optimized MMI design. 23
3.2 Dimensions of the optimized AMMI design. 29
3.3 Dimensions of the PBS 34

5.1 Comparison of our work with previous 400 Gb/s demonstrations. 98

List of common acronyms

ADC	**A**nalog to **D**igital **C**onverter
AMF	**A**dvanced **M**icro **F**oundry
AMMI	**A**symmetric **M**ulti **M**ode **I**nterference
ANT	**A**pplied **N**ano **T**ools
B2B	**B**ack **T**o **B**ack
BER	**B**it **E**rror **R**ate
BOA	**B**ooster **O**ptical **A**mplifier
BOX	**B**uried **Ox**ide
CMOS	**C**omplementary **M**etal **O**xide **S**emiconductor
CW	**C**ontinuous **W**ave
CWDM	**C**oarse **W**avelength **D**ivision **M**ultiplexing
DAC	**D**igital to **A**nalog **C**onverter
DC	**D**irect **C**urrent
DCI	**D**ata **C**enter Optical **I**nterconnects
DD	**D**irect **D**etection
DD-LMS	**D**ecision **D**irected **L**east **M**ean **S**quares
DP	**D**ual **P**olarization
DP-MEMZM	**D**ual Parallel **M**ulti **E**lectrode **M**ach **Z**ender **M**odulator
DP-PAM2	**D**ual **P**olarization 2-level **P**ulse **A**mplitude **M**odulation
DP-PAM4	**D**ual **P**olarization 4-level **P**ulse **A**mplitude **M**odulation
DSO	**D**igital **S**ampling **O**scilloscope
DSP	**D**igital **S**ignal **P**rocessing
DWDM	**D**ense **W**avelength **D**ivision **M**ultiplexing
EAM	**E**lectro **A**bsorption **M**odulator
EBeam	**E**lectron **Beam**

EDFA	**E**rbuim **D**oped **F**iber **A**mplifier
EE	**E**lectrical **E**lectrical
EME	**E**igen **M**ode **E**xpansion
EML	**E**xternally **M**odulated **L**aser
EO	**E**lectro **O**ptic
ER	**E**xtinction **R**atio
FDTD	**F**inite **D**ifference **T**ime **D**omain
FFE	**F**eed **F**orward **E**qualizer
FIR	**F**inite **I**mpulse **R**esponse
FSR	**F**ree **S**pectral **R**ange
HD-FEC	**H**ard **D**ecision **F**orward **E**rror **C**correction
ICR	**I**ntegarted **C**oherent **Receiver**
IL	**I**nsertion **L**oss
IQ	**I**nphase **Q**uadrature
IM	**I**ntensity **M**odulation
IME	**I**nstitute of **M**icro **E**lectronics
InP	**In**dium **P**hosphide
ISI	**I**nter **S**ymbol **I**nterference
KP4-FEC	**KP4** **F**orward **E**rror **C**correction
LCA	**L**ightwave **C**omponent **A**nalyzer
LIDAR	**LI**ght **D**etection **A**nd **R**anging
LMS	**L**east **M**ean **S**quares
MEMS	**M**icro **E**lectro **M**echanical **S**ystems
MEMZM	**M**ulti **E**lectrode **M**ach **Z**ender **M**odulator
MIMO	**M**ultiple **I**nput **M**ultiple **O**utput
MMI	**M**ulti **M**ode **I**nterference
MPW	**M**ulti **P**roject **W**afer

MRM	**M**icro **R**ing **M**odulator
MZI	**M**ach **Z**ehnder **I**nterferometer
NRZ	**N**on **R**eturn to **Z**ero
OADM	**O**ptical **A**dd **D**rop **M**ultiplexer
OIF	**O**ptical **I**nternetworking **F**orum
OMA	**O**ptical **M**odulation **A**mpltiude
OSA	**O**ptical **S**pectrum **A**nalyzer
PAM	**P**ulse **A**mplitude **M**odulation
PAM2	2-level **P**ulse **A**mplitude **M**odulation
PAM4	4-level **P**ulse **A**mplitude **M**odulation
PAM8	8-level **P**ulse **A**mplitude **M**odulation
PBC	**P**olarization **B**eam **C**ombiner
PBS	**P**olarization **B**eam **S**plitter
PCB	**P**rinted **C**ircuit **B**oard
PD	**P**hoto **D**etector
PDFA	**P**raseodymium **D**oped **F**iber **A**mplifier
PIC	**P**hotonic **I**ntegrated **C**ircuit
PLC	**P**lanar **L**ightwave **C**ircuits
PSM	**P**arallel **S**ingle **M**ode
PSR	**P**olarization **S**plitter **R**otator
QAM-16	16-ary **Q**audrature **A**mplitude **M**odulation
QAM	**Q**audrature **A**mplitude **M**odulation
QSFP	**Q**uad **S**mall **f**orm factor **P**luggable
RC	**R**aised **C**osine
RRC	**R**oot **R**aised **C**osine
RTO	**R**eal **T**ime **O**scilloscope
SiP	**S**ilicon **P**hotonics

SMF	**S**ingle **M**ode **F**iber
SMSR	**S**ide **M**ode **S**uppression **R**atio
SNR	**S**ignal to **N**oise **R**atio
SOI	**S**ilicon **O**n **I**nsulator
SOP	**S**tate **O**f **P**olarization
SPP	**S**eries **P**ush **P**ull
SPS	**S**ample **P**er **S**ymbol
SV-DD	**S**tokes **V**ector **D**irect **D**etection
SVR	**S**tokes **V**ector **R**eceiver
SWG	**S**ub **W**avelength **G**rating
TDL	**T**unable **D**elay **L**ine
TE	**T**ransverse **E**lectic
TEC	**Te**mprature **C**ontroller
TIA	**T**rans **I**mpedance **A**mplifier
TM	**T**ransverse **M**agnetic
TOSA	**T**ransmitter **O**ptical **S**ub **A**ssembly
TWMZM	**T**raveling **W**ave **M**ach **Z**ender **M**odulator
VOA	**V**ariable **O**ptical **A**ttenuator
VODL	**V**ariable **O**ptical **D**elay **L**ine
WDM	**W**avelength **D**ivision **M**ultiplexing

Chapter 1

Introduction

1.1 Motivation

Global Internet traffic will continue to grow in the foreseeable future owing to the unprecedented increases in application driven traffic demand such as video streaming, online gaming, cloud-based storage and services, internet of things, and big data. Since 2008, peer-to-peer traffic ceased to dominate the Internet traffic and most Internet traffic has originated or terminated in a datacenter [1]. Datacenter traffic is forecasted to grow three-fold in the period from 2016 to 2021 to reach 20.6 zettabytes, where more than 70% of this data traffic stays within the datacenter [1]. To cope with such increases, significant research and development efforts have been directed towards optical datacenter interconnects (DCI) which can be divided to intra-datacenter and inter-datacenter optical interconnects. Intra-datacenter optical interconnects operating over single mode fiber (SMF) links ranging from 500 m to 10 km incorporate high speed pluggable modules such as quad small form-factor pluggable (QSFP). Pluggable modules include optical transceivers, beside drivers and other circuitry, that must meet stringent specifications such as low cost, low power consumption, high yield, and small form factor. Currently, 100 Gb/s optical transceivers based on 4 lanes $\times$ 25 Gb/s non-return to zero (NRZ) signaling are being shipped in volume for service providers and hyper scale datacenters. The four lanes are 4 parallel single mode (PSM) fibers for the 500 m reach and 4 wavelength-division multiplexing (WDM) channels for the 2 and 10 km reaches on the LAN-WDM grid, i.e., 800 GHz spacing, or coarse WDM (CWDM) grid, i.e., 20 nm spacing [2, 3].

The next generation of intra-datacenter optical transceivers will be running at 200 Gb/s and 400 Gb/s which are expected to replace 100 Gb/s in early 2020. Scaling from 100 Gb/s to 200 or 400 Gb/s requires the increase of single lane bitrate and/or number of lanes. Increasing the single lane bitrate requires the increase of the symbol rate and/or the modulation format order. Several ≥100 Gb/s single carrier results have been recently reported using pulse amplitude modulation (PAM), dual polarization PAM, and discrete multi-tone (DMT) [4–7]. In 2017, the IEEE standardized the 200Gbase and 400GBase Ethernet specifications where 4-level PAM (PAM4) has been selected as the modulation format for the SMF optical links [8]. For the 200 Gb/s intra-datacenter links, the transceivers will operate at 25 Gbaud PAM4 signaling, excluding the overhead, over four parallel SMFs, four CWDM channels, and four LAN-WDM channels for the 500 m, 2 km, and 10 km reaches, respectively. For the 400 Gb/s intra-datacenter links, the standard over 500 m reach of SMF is: 50 Gbaud PAM4 $\times$ 4 PSM fibers. On the other hand, eight WDM lanes each operating at 25 Gbaud on the LAN-WDM grid are used for the 2 and 10 km reaches [8]. Also, a multi-source agreement (MSA) supported by broad industry has been recently formed which adopts 100 Gb/s per lane instead of 50 Gb/s [3].

According to the Ethernet alliance road map, future Ethernet speeds are envisioned to be 800 Gb/s and 1.6 Tb/s [9]. Assuming a bitrate of 100 Gb/s per channel, e.g., 50 Gbaud PAM4, 8 $\times$ 100 Gb/s and 16 $\times$ 100 Gb/s configurations are required using either PSM fibers or WDM to enable 800 Gb/s and 1.6 Tb/s, respectively. For the PSM configuration, 8 and 16 PSM fibers are needed per direction for the 800 Gb/s and 1.6 Tb/s, respectively. Hence, significant challenges will be faced for packaging in small form factors. On the other hand, 8 and 16 lasers in addition to a multiplexer at the transmitter side will be required for the 800 Gb/s and 1.6 Tb/s in the WDM case. This configuration will pose significant challenges on the thermal stability and packaging of optical transceivers. Hence, a scalable solution with rates beyond 100 Gb/s per channel is desirable for next generation optical interconnects.

Recently, a stokes vector receiver (SVR) has been proposed for self-coherent reception of single polarization complex modulated signals multiplexed with a tone on the other polarization [10, 11]. In [12], dual-polarization intensity modulation / direct-detection (IM/DD) has been proposed and experimentally demonstrated using a SVR and novel digital signal processing (DSP). Using the polarization dimension and a DD receiver offers a better scalable solution compared to single polarization PSM or WDM due to the reduction in the number of lasers required to achieve the same aggregate bitrate if the polarization dimension is exploited.

In addition, the point-to-point metro-access DCI (80 - 120 km) are attracting much attention due to the traffic increases in inter-datacenter traffic. DD and coherent solutions are competing for such links. DD solutions are based on NRZ/PAM4 and dense WDM (DWDM) which offers small form factor and low power consumption compared to the coherent counter-parts. However, fiber dispersion needs to be compensated using chirped fiber bragg gratings or dispersion compensation fiber. Such dispersion compensation module adds complexity specially at higher bitrates and lacks flexibility. Moreover, several techniques have been proposed to enable the dispersion compensation using DSP whilst DD system such as: single side band modulation, SVRs, Kramers-Kronig receivers, and Tomilson-Harashima precoding [13–16]. However, all systems have a complexity that approaches a full coherent system while not capable of modulating the four degrees of freedom or require much larger bandwidth components. Recently, the optical internetworking forum (OIF) has released the specifications for the 400G-ZR based on coherent dual polarization 16-ary quadrature amplitude modulation (QAM-16) [17]. Using DSP and the 7 nm CMOS node, the power consumption of the coherent solution can meet the specifications and balance with the DD solution [18]. The remaining challenge for the coherent solution will be the form factor. Moreover, the coherent solution for $80-100$ km can be unamplified due to the availability of the local oscillator (LO).

Different material platforms can be used to build either the DD or the coherent optical transceivers including the indium phosphide (InP) platform and the silicon photonics (SiP) platform [19]. The SiP platform has the potential to build compact, high yield, high performance, and low cost complementary metal oxide semiconductor (CMOS) compatible transceivers [20]. In the last few years, a plethora of SiP designs has been demonstrated ranging from device level demonstrations, e.g., multi-mode interference (MMI) couplers [21, 22], polarization beam splitters (PBSs) [23, 24], traveling wave Mach-Zehnder modulators (TWMZMs) [25, 26], to system level demonstrations, e.g., 4×25 Gb/s WDM transceiver [27], and coherent transceivers [28, 29]. Owing to the low cost and small form factor of the SiP platform, several companies are using such platform for the transceiver products such as Intel, Rockley, and Neo-photonics.

In this thesis, we work on several research areas under optical transceiver development for DCI. In the first part of the thesis, we present passive and active SiP components for DD and coherent optical photonic integrated circuits (PICs). Then, we present PICs targeting next generation intra-datacenter optical interconnects operating at 200 Gb/s and beyond. Finally, we present system-level demonstrations using commercial products for 400 Gb/s and beyond.

1.2 Organization of the Thesis

The remainder of this thesis is organized as follows.

In Chapter 2, we introduce the SiP platform detailing its advantages and disadvantages. Then, we explain the design of passive and active components in the SiP platform.

Chapter 3 presents different passive and active SiP devices operating in different optical bands. First, we present the design of an O-band 2×2 MMI coupler and present results on a wafer-level. Secondly, an asymmetric MMI (AMMI) with subwavlength grating (SWG) is reported. Next, we present the design of a MMI based PBS operating in the C-band. Next, the design of a high yield polarization splitters and rotators (PSR) is detailed and experimental results over a wafer scale are reported. Finally, we demonstrate variable optical attenuators (VOAs) targeting both O-band and C-band applications.

In Chapter 4, we focus on active SiP transmitters targeting 200 Gb/s and 400 Gb/s optical interconnects. First, we demonstrate a 400 Gb/s transmitter using 4 parallel TWMZMs for short reach optical interconnects. Then, we propose the design of a 200 Gb/s transmitter based on multi-electrode MZMs to simplify the driver requirements while not sacrificing on the bandwidth. Finally, we report the design of a dual-polarization intensity modulator which exploits the other polarization while operating in DD using a SVR.

In Chapter 5, we present two system-level demonstrations. First, 168 Gb/s single polarization and single wavelength PAM4 demonstration over 10 km in the O-band is presented. Also, we present the first demonstration of a 400 Gb/s CWDM-TOSA for intra-datacenter optical interconnects.

Finally, Chapter 6 concludes the thesis summarizing the key contributions made and list some of the potential improvements and future research work in the short and long terms.

1.3 Original contributions

The original contributions of this thesis are summarized hereafter.

Passive and active SiP devices for optical transceivers

We designed and experimentally demonstrated five different passive and active SiP based devices for PICs. The device design and performance are summarized below.

- First, we present a simple design for power splitters which are essential components of any PIC. We present broadband O-band 2×2 MMI couplers. The design target is for transverse electric (TE) mode only. The designs have been fabricated on a 200 mm wafer in a CMOS foundry. The splitting ratio is close to 3 dB over 80 nm bandwidth with a maximum imbalance of ±0.5 dB. Moreover, we presented the wafer-level splitting ratio where the mean coupling ratio has a standard deviation of only 0.042 dB across the entire wafer.

- Then, we propose and experimentally demonstrate a broadband and compact single etch asymmetric splitter using SWG based MMI coupler. We use the MMI coupler due to its superior fabrication tolerance compared to other splitter designs. Also, we add SWGs to the MMI slab to engineer the refractive index and hence yield a more compact and broadband design. By introducing a cut in one of the MMI slab sides, the symmetry is broken and hence different splitting ratios can be achieved. The design has been optimized using 3D- Finite difference time domain (FDTD) simulations, and fabricated using electron beam (EBeam) lithography. The asymmetric MMI has the size of only 23.7 µm × 3 µm. In [30], we report results for five different splitting ratios ranging from 50:50 to 85:15 over 100 nm bandwidth.

- We propose and experimentally demonstrate a C-band SiP PBS. The PBS is based on a MMI design to provide a fabrication tolerant device. Since the effective index is different for the TE and transverse magnetic (TM) polarizations, by adjusting the dimensions of the MMI, different polarizations can be directed to different MMI ports. Also, by cascading MMIs, residual crosstalk can be filtered to increase the extinction ratio (ER). The design has been verified by simulations and measurements in [31]. The PBS has achieved ERs larger than 14 dB, and 20 dB over more than 55 nm spectral range including the entire C-band for the TE and TM ports, respectively.

- We propose ultra-fabrication tolerant and broadband PSRs for C-band and O-band operation. In the C-band, the PSRs are needed in the dual polarization inphase/quadrature (DP-IQ) transmitter PIC and the integrated coherent receiver (ICR) PIC for polarization multiplexing. On the other hand, they are used in the O-band in the receiver side for polarization diversity since the input polarization is random. The PSR has mainly two sections which are the polarization rotation and the polarization splitting. For the rotator design, we use a rib waveguide to break the symmetry. For the splitter side, we used an adiabatic coupler to enable broad bandwidth and low loss. Also, we added clean-up filters to increase the ER at the output ports. In [32], we present the device design and report wafer scale data for the O-band design where the minimum ER over 80 nm bandwidth has an average of 21.82 dB and 19.05 dB with a standard deviation of 2.42 dB and 1.559 dB for the upper and lower ports, respectively.

- Finally, we present low power and broadband VOAs which are essential components for the DP-IQ and ICR PICs. The VOAs are based on a Mach-Zehnder interferometer structure. Different variations are fabricated using EBeam lithography using different input and output couplers, heater length and width, operating wavelength, and substrate undercut. Experimental results show that including the substrate undercut a 3X improvement can be achieved in the power consumption, at the expense of a reduction in electrical bandwidth, where 20 dB attenuation can be achieved using only 8 mW.

Photonic integrated circuits for datacenter optical interconnects:

- First, we present the design and experimental demonstration of a SiP MZM based four lane 400 Gb/s transmitter for PSM based intra-datacenter optical interconnects. The transmitter is based on four parallel TWMZMs with 4 mm electrode length. Preliminary results of the transmitter are presented in [33]. Then, we report the device details, small-signal, and large-signal characterization of the transmitter in [34]. Also, we study the electro-optic (EO) crosstalk between the four MZMs using small-signal characterization and confirm the results with large-signal experiment. For large-signal modulation, we characterize the performance of the transmitter versus several parameters. Although, several 100 Gb/s demonstrations have been published to date based on SiP MZMs, we believe the results of a single TWMZM of our transmitter is the best result for a MZM with a lateral PN junction in terms of driving voltage swing and equalization complexity to the best of our knowledge. Moreover, we demonstrate the first demonstration of a simultaneous modulation of a 4-lane SiP transmitter running at an aggregate rate of 400 Gb/s .

- Next, we propose a SiP transmitter targeting 200 Gb/s Ethernet specifications. The design is based on two parallel multi-segment modulators where each modulator can achieve more than 100 Gb/s. Using a multi-segmented modulator, PAM4 modulation format can be generated optically without the need for digital to analog converters (DACs) and with superior signal to noise ratio to single electrode MZMs. Moreover, it offers the flexibility in the design for lower driving voltage swing while achieving a a large bandwidth due to the short segments. The four segments have been simultaneously modulated without DSP at the transmitter side. The transmitter can achieve more than 200 Gb/s using less than 2 Vpp drive voltage on each segment. To the best of our knowledge, this represents the lowest drive voltage using a SiP segmented modulator delivering more than 100 Gb/s reported up to date [35]. Hence, the demonstrated transmitter presents a potential design for next generation 200 Gb/s intra-datacenter transceivers.

- The increases in datacenter traffic pushes for more increases in single channel bitrate. In 2017, dual polarization IM (DP-IM) with SVRs have been proposed. Hence, we experimentally demonstrate a DP-IM O-band SiP transmitter for intra-datacenter optical interconnects. The transmitter is built using two identical O-band TWMZMs. We experimentally demonstrate the transmitter in a Stokes vector direct-detection (SV-DD) system for DP-IM signals with 2-level and 4-level pulse amplitude modulation (DP-PAM2 and DP-PAM4) formats. The DD-SVR followed by offline DSP is implemented for SOP de-rotation. Preliminary results for the transmitter are reported for PAM2 modulation only in [36]. Then, more detailed study where we characterize the performance of the SV-DD system versus number of taps, received signal power, state of polarization (SOP), reach, and bitrate is presented in [37]. Results reveal that 200 Gb/s DP-PAM4 are successfully received over 2 km of SMF.

System-level PAM4 demonstrations for short reach applications:

- First, we demonstrate single polarization PAM4 in the O-band, where we study the bit error rate (BER) performance versus bitrate, number of receiver equalizer taps, received signal power, and reach. Using a commercial Lithium Niobate modulator and state of the art DAC and analog to digital converter (ADC), we experimentally demonstrate 168-Gb/s single polarization PAM4 transmission over 10 km of SMF in the O-band. At the time of the experiment, these results are the highest bitrates reported for O-band, single channel and single polarization PAM4 transmission over 10 km of SMF with DD applicable in DCI [38].

- Then, we present the first demonstration of 400 Gb/s ($4\lambda\times$ 100 Gb/s) transmitter optical sub-assembly (TOSA) on the CWDM grid, i.e., 20 nm spacing, targeting 400G-FR4 requirements over 2 km. The TOSA is based on Lumentum LLC uncooled InP external modulated laser (EML) technology and it utilizes four EMLs followed by a CWDM multiplexer. We characterize the performance of the TOSA versus received optical modulation amplitude (OMA), number of equalizer taps, reach, modulation format, TOSA case temperature, and bitrate. In [39], we show that bitrates beyond 400 Gb/s can be transmitted over up to 20 km of SMF without optical amplification.

Chapter 2

Introduction to the silicon photonics platform

2.1 Overview

The SiP platform is a technology platform that is used to build devices and PICs using silicon as the primary host material. The silicon material has many advantages such as abundance and high refractive index. Also, silicon is transparent for the telecommunications bands over SMF links, and can be used to build nearly all required functions for optical transceivers as explained in the next sections. A typical layer stack of a SiP process is shown in Fig. 2.1 [40]. The silicon layer used to define the photonic devices sits on a silicon-dioxide layer called the buried oxide layer (BOX) and hence the name silicon-on-insulator (SOI). In addition, the cladding layer is commonly silicon-dioxide as well. The material refractive index of the silicon and silicon-dioxide versus wavelength is shown in Fig. 2.2 [41]. Such high index contrast between the waveguide and cladding is the reason for the ability to build very compact devices in the SiP platform.

Compared to other material platforms such as InP, the SiP platform has the following advantages. First, the SiP platform uses years and billions of dollars invested to develop

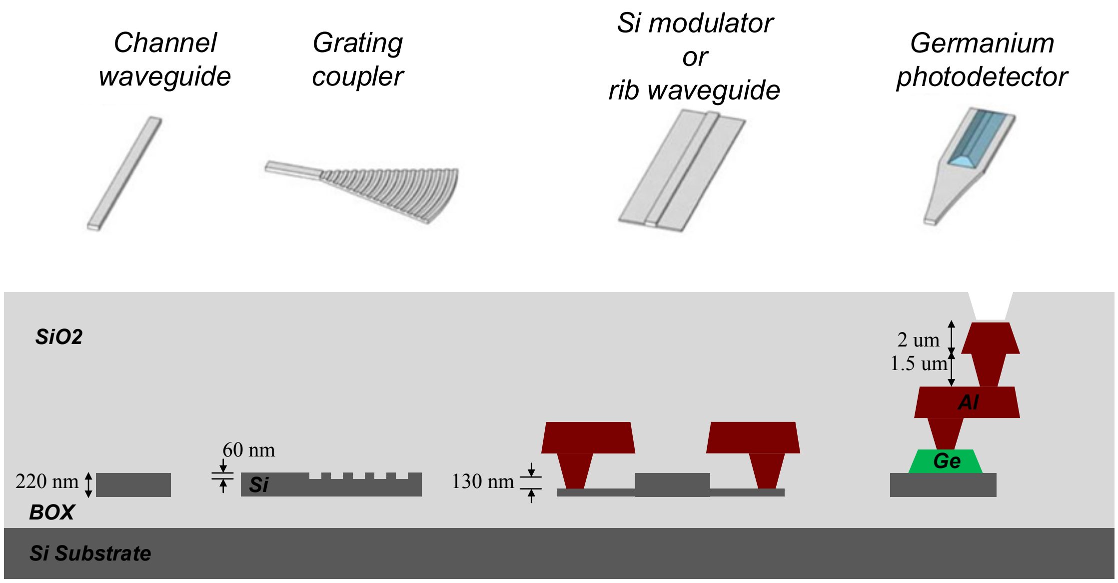

Figure 2.1. Silicon photonic technology cross-section.

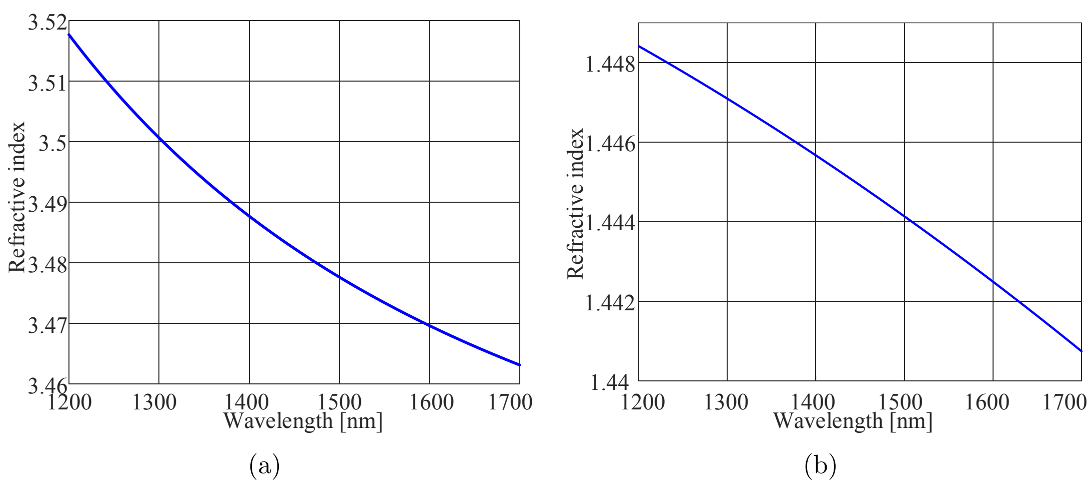

Figure 2.2. Material refractive index for (a) silicon and (b) silicon-dioxide.

the microelectronics industry processes. Hence, all tools and processes used in the CMOS industry were leveraged to develop mature photonic capabilities with very high yield [20]. Also, the SOI wafers can be much larger than the InP wafers, e.g., 300 mm versus 150 mm wafers. Finally, the whole process is significantly lower cost compared to InP due to the abundance of the silicon material, CMOS compatibility, and large wafer sizes. The main disadvantage of the SiP platform is the lack of a native laser source which will be discussed in Section 2.2.

In the last decade, the SiP platform has been used for different applications such as: optical transceivers [42], biosensing [43], nonlinear optics [44], light detection and ranging (LIDAR) systems [45], optical gyroscopes [46], and microwave photonics [47]. In this thesis, our focus is in optical devices and circuits for data-center optical interconnects. Figures 2.3 and 2.4 show the schematic diagram of transceivers for the IM/DD based intra-data center application, and the coherent based inter-data center application, respectively. It can be noted that a significant number of designs (e.g., modulators, photo-detectors (PDs), polarizing optics) are common to the PICs required for both applications. We can divide the devices into four categories: lasers, passive devices, active devices, and PICs.

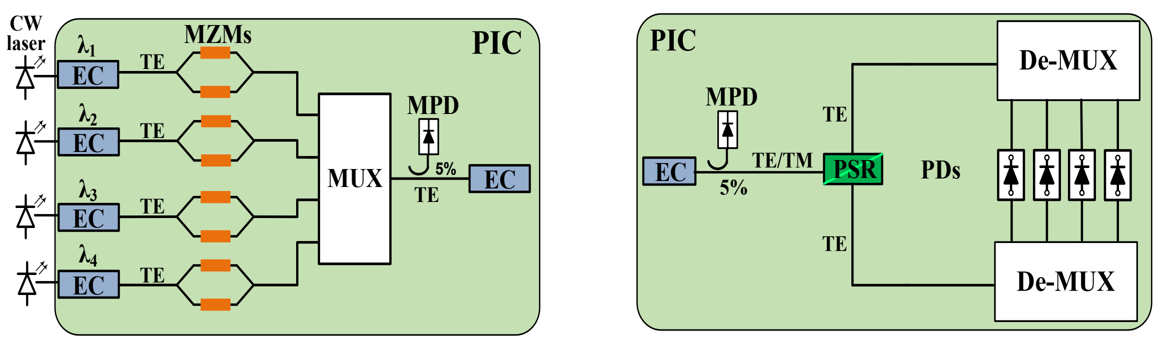

(a)

(b)

Figure 2.3. PIC schematics for IM/DD based transceivers: (a) the transmitter architecture (4-λ schematic shown), and (b) the receiver architecture (4-λ schematic shown). EC: Edge Coupler. MZM: Mach-Zehnder Modulator. MUX: Multiplexer. MPD: Monitor photo-detector. PSR: Polarization Splitter and Rotator. VOA: Variable Optical Attenuator. DEMUX: Demultiplexer. PD: photo-detector.

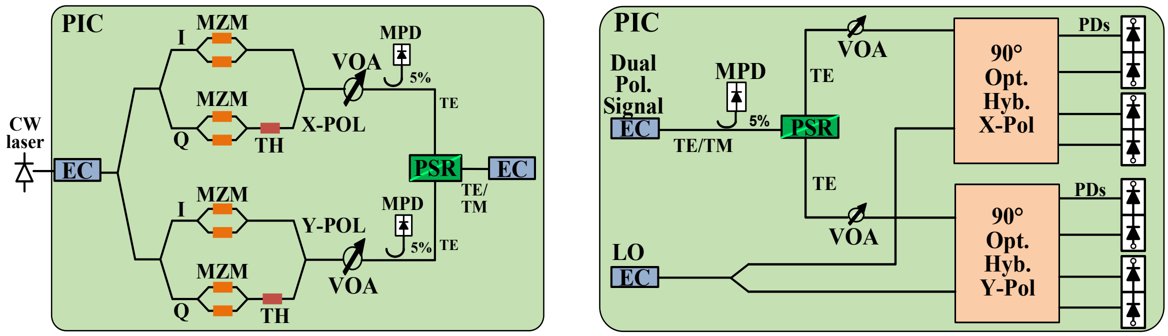

(a) (b)

Figure 2.4. PIC schematics for coherent based transceivers: (a) the transmitter architecture, and (b) the receiver architecture. EC: Edge Coupler. MZM: Mach-Zehnder Modulator. TH: Thermal Heater. VOA: Variable Optical Attenuator. MPD: Monitor Photo-detector. PSR: Polarization Splitter and Rotator. LO: Local Oscillator. PD: Photo-detector.

2.2 Laser source

The main disadvantage of the SiP platform is the lack of a gain medium or a laser. This is attributed to the fact that the silicon material has an indirect bandgap. There is a lot of research related to growing germanium for lasers integrated in silicon [48–50]. However, their performance is still far from being commercialized. The other options are wafer-level bonding [51], epitaxial growth of III-V gain medium on the SiP wafer [52], die-level bonding [53, 54], and external laser sources [55]. The first approach has been developed by UCSB, Ghent University, Intel, and Aurrion [56–58]. The wafer bonding involves bonding an unpatterned InP wafer to an SOI wafer, and processing it further to fabricate the integrated laser. However, the yield of such approach is not high and the cost due to the different wafer size is high. On the other hand, growing III-V material on the silicon wafer was reported in [52] and can lower the cost by growing the gain medium on large silicon wafers. In a more economical route, the InP-substrate having the laser III-V-gain-layers on top is first diced, and the dies are bonded where needed [59, 60]. Then, the III-V dies are processed to form the lasers. Putting the expensive III-V gain material only where needed saves on cost.

In addition, laser arrays have been flip-chip bonded to an SOI chip and coupled using edge couplers [61–63]. Moreover, semi-conductor amplifiers where butt-coupled to SOI dies where the reflectors are designed in the SOI platform to enable lasers [64, 65]. Finally, the most used approach is based on external laser sources that are coupled to the SiP chip using grating couplers or edge couplers [66]. The main advantages are adding the optical isolators and the achieved yield is very high plus using reliable laser sources.

2.3 Passive components

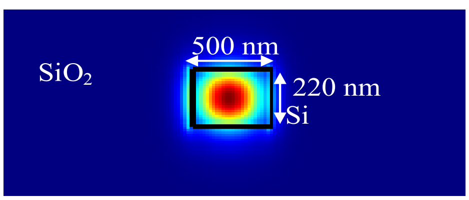

(a)

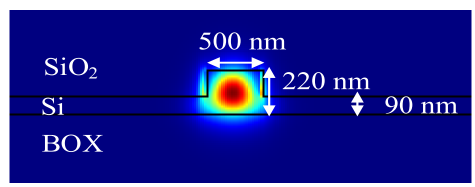

(b)

Figure 2.5. TE mode optical field at 1550 nm for (a) channel and (b) rib waveguides.

The SiP platform is an excellent platform for passive devices due to the compact footprint and low losses. Passive devices are essential components for optical transceivers shown in Figs. 2.3 and 2.4 such as coupling devices, power splitters, polarization handling, multiplexers, and etc.

The basis of all passive components is the design of the waveguide, i.e., channel and rib waveguides. The cross-section of both waveguides is shown in Fig. 2.2, and an example of the optical field for the fundamental TE mode in both waveguides is shown in Fig. 2.5. The effective index versus width of channel waveguides for the first four modes is shown in Fig. 2.6 [41]. Here, we consider a fixed thickness of the silicon core to be 220 nm which is the most commonly used in different foundries. It can be observed that the channel

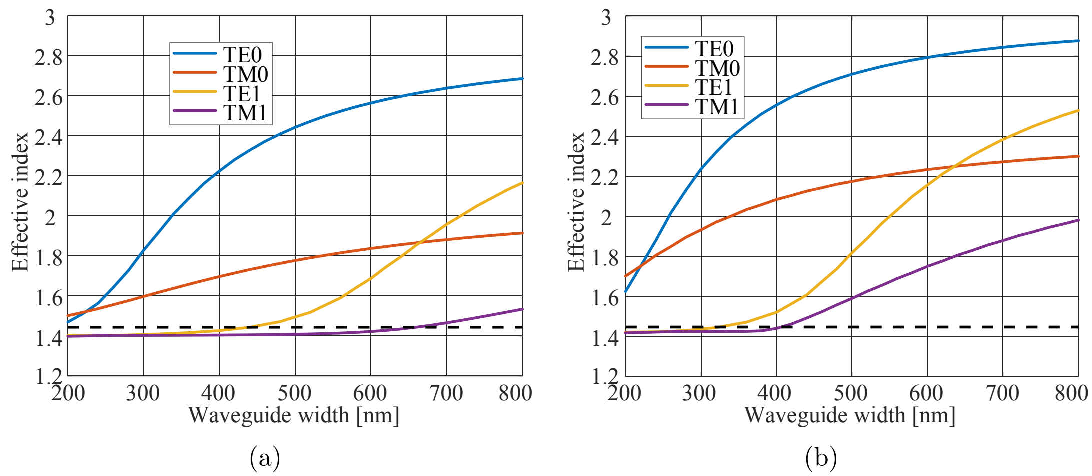

Figure 2.6. Effective refractive index for channel waveguide at (a) 1550 nm and (b) 1310 nm.

waveguide supports both mode polarizations and the single-mode cut-off is approximately 450 nm and 350 nm for the C-band and O-band cases, respectively. In our designs, we choose the waveguide width to be 500 nm and 400 nm for the C-band and O-band cases, respectively, as a good balance between the single mode condition and propagation losses. In Fig. 2.7, the effective index of the first order modes of a rib waveguide versus core waveguide width is shown. The slab thickness is fixed at 90 nm as per most SiP foundry specifications. One important observation is that the rib waveguides supports TE modes only at the shown waveguide widths which is beneficial in the polarization rotator designs reported in Chapter 3. In Fig. 2.8, we show the effective index and group index for the fundamental TE mode of a rib waveguide versus wavelength. It is observed that the SOI waveguides are dispersive due to both waveguide and material dispersion. The group index of the SOI waveguides is shown in Fig. 2.8(b) in the O-band since the MZM designs in this thesis are all in the O-band. The group index is an important parameter in the design of MZMs for the velocity matching with the microwave signal.

As observed from previous figures, the channel waveguide has higher effective index than the rib waveguide which translates to stronger optical confinement and lower crosstalk.

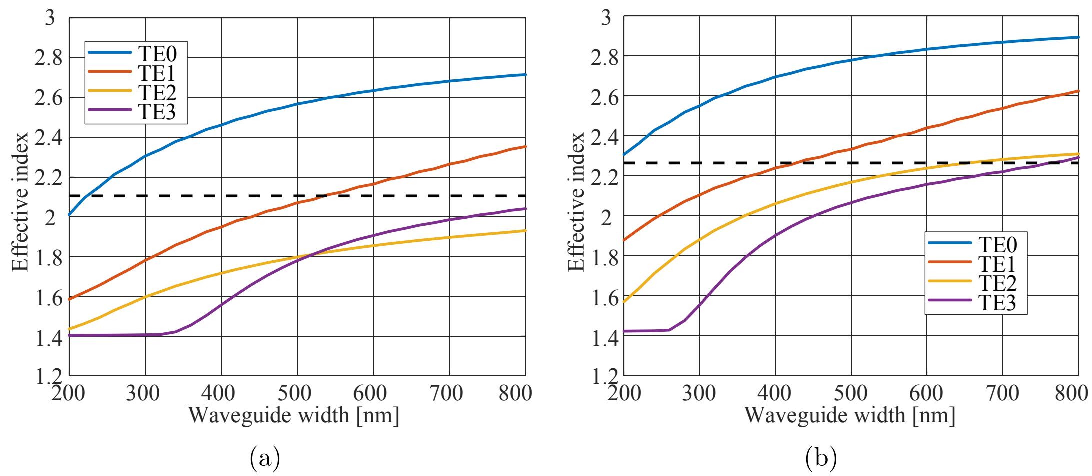

Figure 2.7. Effective refractive index for rib waveguides at (a) 1550 nm and (b) 1310 nm.

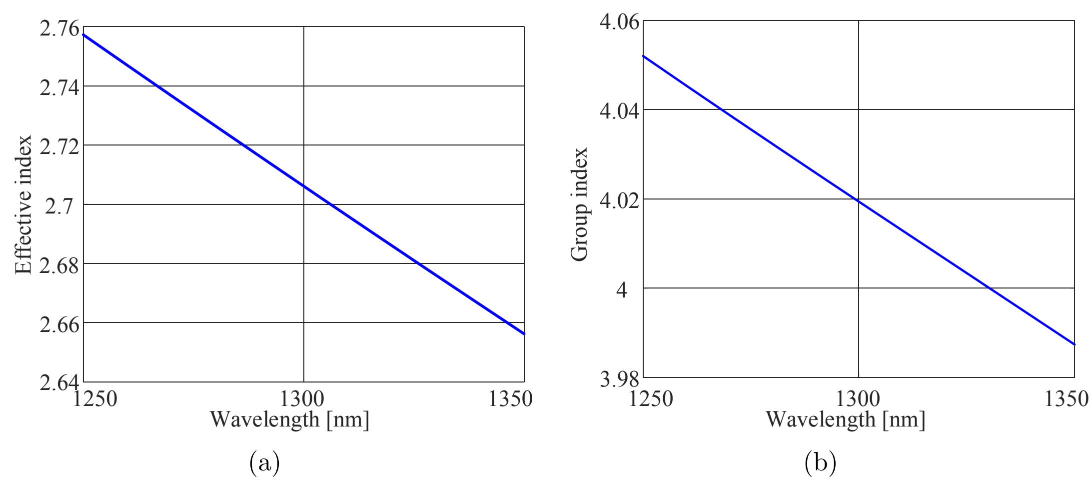

Figure 2.8. (a) Effective refractive index and (b) group index for rib waveguides at 1310 nm.

However, the propagation losses are higher due to the scattering losses from side-wall roughness. On the other hand, rib waveguides have a silicon slab region on the sides of the waveguide core which pushes the optical mode downwards as shown in Fig. 2.5(b). Hence, the mode overlap with the side-walls is lower compared to the channel waveguides which results in lower propagation losses. The reported losses for channel waveguides are in the range of 2 - 3 dB/cm and 1-1.5 dB/cm for rib waveguides in the institute of microelectronics

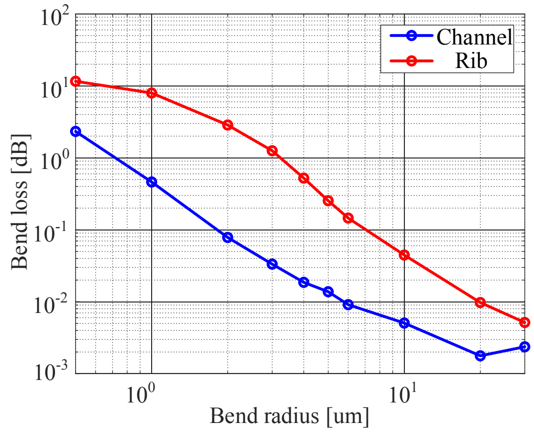

Figure 2.9. Loss per 90° bend for the fundamental TE mode in channel and rib waveguides.

(IME) process [40, 67]. On the other hand, the optical crosstalk between waveguides is higher in rib waveguides than channel waveguides. The simulated 90° bending losses is shown in Fig. 2.9. Channel waveguides have a significantly lower loss per bend compared to rib waveguides where a bend radius of 10 µm results in a bend loss below 0.01 dB [41]. Further improvements in the propagation loss in the same process can be achieved using low loss multimode straight waveguides with single mode channel waveguides for bends which is used in the designs presented in Chapter 4.

In Chapter 3, we build on the concepts shown in this section and demonstrate passive SiP designs including splitters, a PBS, and polarization splitters and rotators.

2.4 Active components

The main active components of an optical transceiver module as the PICs showed in Fig. 2.3 and Fig. 2.4 are the modulators and photodetectors.

2.4.1 Modulators

Modulation is achieved by inducing changes to the refractive index of the material. This can be achieved through electro-optic effects or the plasma-dispersion effect [68]. Among the electro-optic effects is the Pockels effect and Kerr non-linear effect. Since unstrained silicon is centrosymmetric, the Pockels effect is absent. Also, the Kerr effect is relatively weak [69]. The strongest effect for the silicon material is the plasma-dispersion effect where free carrier density changes can induce changes in the absorption coefficient and the refractive index [68, 69]. The change in the absorption coefficient and the refractive index due to the carrier concentration is given by the following equations [70]:

$$\Delta\alpha = 8.88 \times 10^{-21}\Delta N_e^{1.167} + 5.84 \times 10^{-20}\Delta N_h^{1.109} \tag{2.1}$$

$$\Delta n = -(5.4 \times 10^{-22}\Delta N_e^{1.011} + 1.53 \times 10^{-18}\Delta N_h^{0.838}) \tag{2.2}$$

where N_e, and N_h are the carrier concentrations for the electrons and holes, respectively.

To change the carrier concentration, three different PN junction structures are considered which are carrier accumulation, carrier injection, and carrier depletion [68]. Among them, the carrier depletion PN junction shows the highest bandwidth due to the reduced junction capacitance of the PN junction in the reverse bias mode.

An interferometric or a resonant structure is needed to convert the phase changes in the field due to the changes in the carrier concentration to amplitude changes. As an example of resonant structure is the micro-ring modulator (MRM). Although it is compact, it has a poor fabrication tolerance and thermal sensitivity. For high speed transceivers, a MZM is the best choice since it can be designed for large bandwidth and low thermal sensitivity [25]. A schematic of the MZM is shown in the transmitter side of Fig. 2.3(a).

The MZM can be driven in three driving configurations, i.e., single-drive, differential drive, and series push-pull (SPP). For the single drive configuration, a single PN junction is embedded to one of the arms of the interferometer and a single RF signal is used to drive the MZM. However, it suffers from lower bandwidth compared to the SPP case and chirp in the generated field. For the other two configurations, the two arms of the MZM have PN junctions. For the differential drive configuration, both arms are driven by two differential signals which ideally eliminates the chirp and haves the power consumption compared to the single drive case. For the SPP configuration, the two diodes of the PN junction are connected back-to-back. The SPP structure increases the bandwidth by halving the junction capacitance, and enables the MZM to be driven by a single RF signal. All the MZM shown in this thesis are based on SPP MZMs. Figure 2.10(a) shows a cross-section view of a MZM. In the shown schematic, the PN junction is formed by low doping concentrations to decrease the optical loss, and the high doping is used for ohmic contact. Intermediate doping levels are also added to improve the bandwidth without incurring a significant optical loss. Finally, the MZMs reported in this thesis are based on traveling wave structures to enable high bandwidth. The TWMZM bandwidth is limited by microwave losses, impedance matching, and velocity matching. The details for the design of TWMZMs can be found in [25].

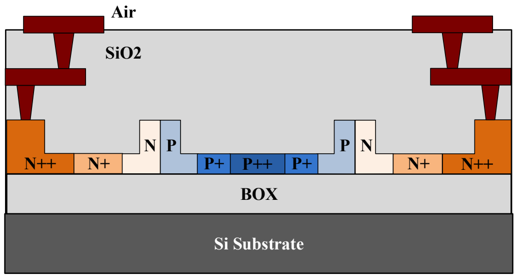

(a)

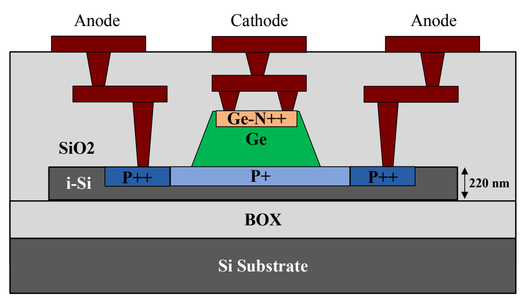

(b)

Figure 2.10. Schematics for the (a) TWMZM cross-section and (d) PD cross section.

2.4.2 Photo-detectors

As we mentioned before, one of the advantages of the silicon material is that it is transparent at telecom wavelengths making it a great material for waveguides. However, having a PD will not be possible using the silicon material which is a crucial component of optical transceivers. The solution is to epitaxially grow germanium which can absorb light at the telecommunication wavelengths until the edge of the L-band and it is CMOS compatible.

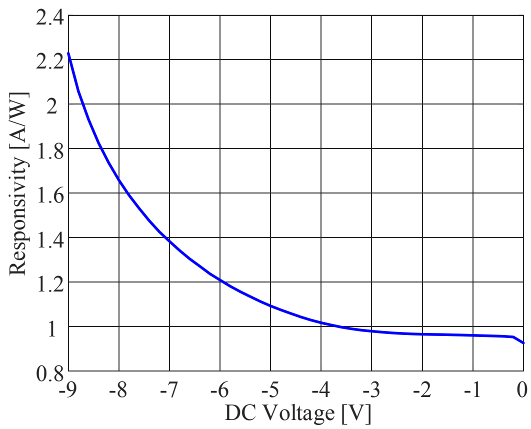

(a)

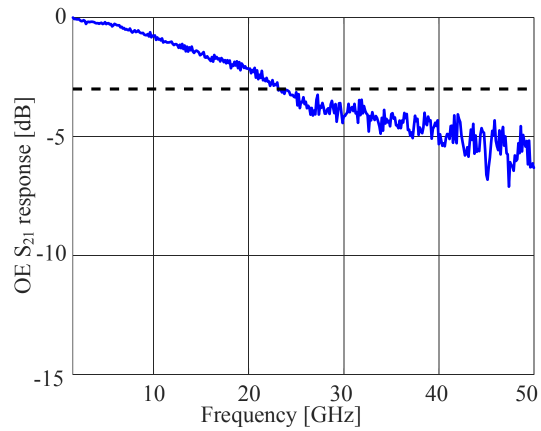

(b)

Figure 2.11. (a) PD responsivity and (b) Opto-electric bandwidth of the PD.

Several waveguide-coupled germanium on silicon PDs have been reported in the literature with excellent performance [71–73]. An example for a vertical junction PD using 500 nm germanium layer thickness is shown in Fig. 2.10(b). Figure 2.11 shows the responsivity of the PD versus the applied voltage and the opto-electric bandwidth of the PD at 1310 nm wavelength. The measured responsivity is 0.94 A/W at -2V DC bias and increases to approximately 2 A/W, i.e., a gain of 2.1, at -9V bias. The PD has approximately 22 GHz bandwidth but with a slow roll-off where the 6 dB point is observed at 50 GHz. Using a low profile germanium with thickness of 160 nm, a PD with 67 GHz bandwidth and 0.9 A/W responsivity is demonstrated [74]. Hence, SiP PDs showed comparable performance to the III-V counterparts.

Chapter 3

Passive and active silicon photonic devices

3.1 Overview

Building on the SiP basics presented in the previous chapter. In this Chapter, we present the design and experimental results for five different passive and active devices which represent key building blocks of any SiP based PIC. This chapter is organized as follows. In section 3.2, we present the design of an O-band 2×2 MMI coupler and present results over a wafer-level. In section 3.3, an AMMI with SWGs is reported. Next, section 3.4 presents the design of a MMI based PBS operating in the C-band. In section 3.5, we report high yield, low insertion loss (IL), and large bandwidth PSR designs for C-band and O-band applications. Low power consumption VOA designs are presented in section 3.6. Finally, concluding remarks are given in section 3.7.

3.2 O-band MMI 3-dB splitter

3.2.1 Introduction

Beam splitters are essential components in any PIC and 3-dB couplers are the most common splitters used in MZMs [25], switches [75], etc. Several 3-dB couplers have been reported in the literature using directional couplers [41], adiabatic couplers [76], Y-branches [77], and MMIs [78]. Although directional couplers are compact, they suffer from poor fabrication tolerance and have a limited bandwidth. Y-branches and adiabatic couplers shows better fabrication tolerance and larger bandwidth [76, 77]. In this section, we present the design and experimental results for a fabrication tolerant 3-dB coupler based on a 2 × 2 MMI. MMI based splitters have the following advantages: broad optical bandwidth, low ILs, and high fabrication tolerance compared to other splitter designs. However, they suffer from a relatively large foot-print. The measured wafer-scale data shows a high yield design where the standard deviation of the splitting ratio is below 0.05 dB across the entire wafer.

3.2.2 Design and simulation results

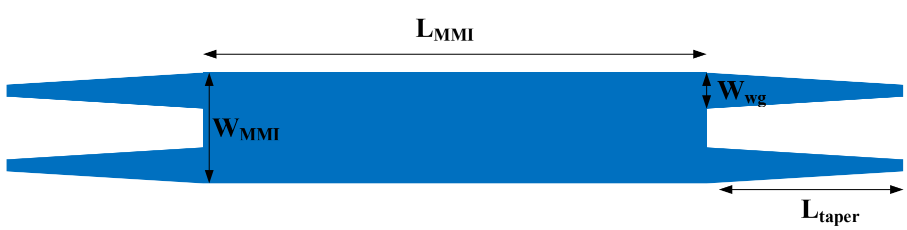

Figure 3.1. Schematic layout for the designed MMI.

The schematic for the proposed MMI is shown in Fig. 3.1. MMIs are based on the interference between the modes in the multi-mode section to provide an image of the input signal or multiple images. The beat length for the MMI is given by [21]

$$L_\pi = \frac{\lambda/2}{n_{eff0} - n_{eff1}}, \tag{3.1}$$

where λ is the operating wavelength, n_{eff0} and n_{eff1} are the effective indices of the first and second order modes, respectively.

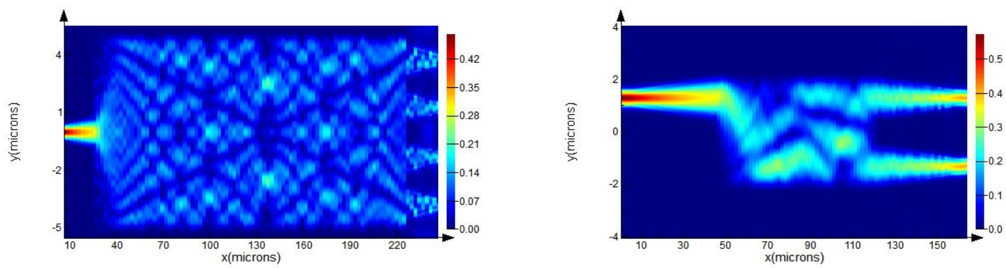

(a) (b)

Figure 3.2. Field profile propagation through (a) 1×N MMI and (b) 2 × 2 MMI.

By adjusting the length of the MMI, a single image or multiple can be directed to the output waveguides of the MMI as shown in Fig. 3.2(a). Here, we present the design of the most widely used 2 × 2 coupler and results can be extended for different designs and splitting ratios. Simulations were carried out using the Lumerical MODE eigen mode expansion (EME) solver to find the proper dimensions for the device. The resulting device dimensions are summarized in Table 3.1.

Table 3.1. Dimensions of the optimized MMI design.

Parameter	**value**
W_{MMI}	4.1 µm
L_{MMI}	75 µm
W_{WG}	1.5 µm
L_{taper}	40 µm

Figure 3.2(b) shows the field propagation through the MMI coupler for a TE polarization input. Then, we present the transmission and power imbalance through the output ports

versus wavelength in Fig. 3.3. The results shows that the MMI design has a good response close to 3-dB over more than 80 nm bandwidth with a maximum power imbalance below 0.15 dB between the output ports.

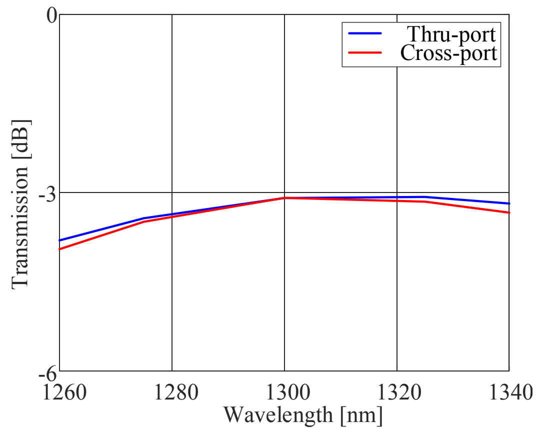

(a)

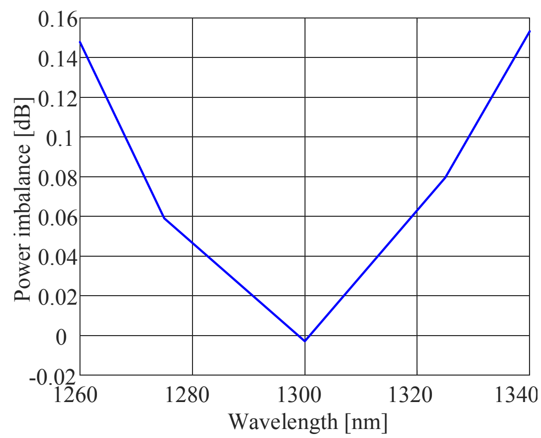

(b)

Figure 3.3. (a) Simulated transmission versus wavelength and (b) power imbalance between both ports of the MMI.

3.2.3 Device fabrication and experimental results

The MMIs were fabricated on a 200 mm SOI wafer with 220 nm nominal top silicon thickness. Vertical grating couplers are used for coupling in and out of the chip with approximately 4 dB loss at 1310 nm. To enable the characterization of the MMI, we used a Mach-Zehnder interferometer (MZI) structure where two MMIs are cascaded with a delay in one arm to create a free-spectral range (FSR) as shown in Fig. 3.4. Since the splitter is not perfectly balanced, we can extract the splitting ratio from the wavelength dependent ER of the output spectrum. This can be understood from the following equations. Using the transfer matrix method, the output electric field can be given by [79]

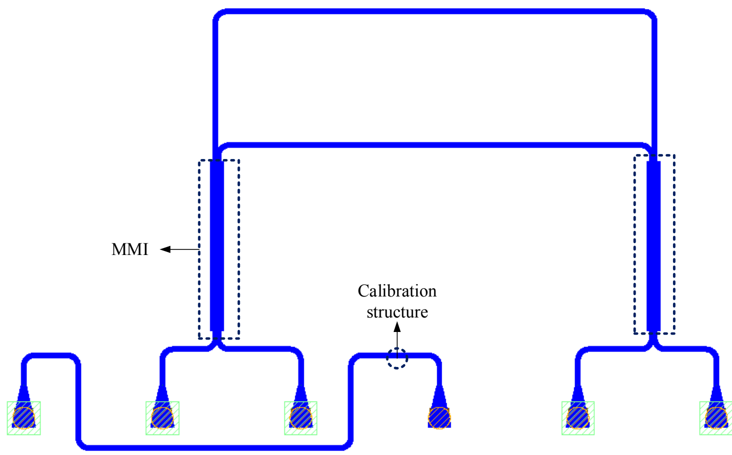

Figure 3.4. Schematic layout for the MZI test structure.

$$\begin{bmatrix} E_{out1} \\ E_{out2} \end{bmatrix} = \begin{bmatrix} \sqrt{1-k^2} & jk \\ jk & \sqrt{1-k^2} \end{bmatrix} \begin{bmatrix} e^{-j\phi_1} & 0 \\ 0 & e^{-j\phi_2} \end{bmatrix} \begin{bmatrix} \sqrt{1-k^2} & jk \\ jk & \sqrt{1-k^2} \end{bmatrix} \begin{bmatrix} E_{in1} \\ 0 \end{bmatrix} \tag{3.2}$$

where k is the coupling coefficient, $e^{-j\phi_1}$ and $e^{-j\phi_2}$ is the phase accumulated through the MZI arm for the first and second arms, respectively, and E_{in1} is the input electric field to the MZI.

$$\begin{bmatrix} E_{out1} \\ E_{out2} \end{bmatrix} = \begin{bmatrix} (1-k^2)e^{-j\phi 1}E_{in1} - k^2 e^{-j\phi 2}E_{in1} \\ jk\sqrt{1-k^2}e^{-j\phi 1}E_{in1} + jk\sqrt{1-k^2}e^{-j\phi 2}E_{in1} \end{bmatrix} \tag{3.3}$$

$$\begin{bmatrix} ER_{out1} \\ ER_{out2} \end{bmatrix} = \begin{bmatrix} \frac{1}{1-4k^2+4k^4} \\ \infty \end{bmatrix} \tag{3.4}$$

From Eq. (3.4), the ER from the second output port is independent of the splitting ratio. However, the first output port is a function of the coupling coefficient, and is equal to infinity if the splitting ratio is exactly 3-dB. Hence, the splitting ratio can be extracted

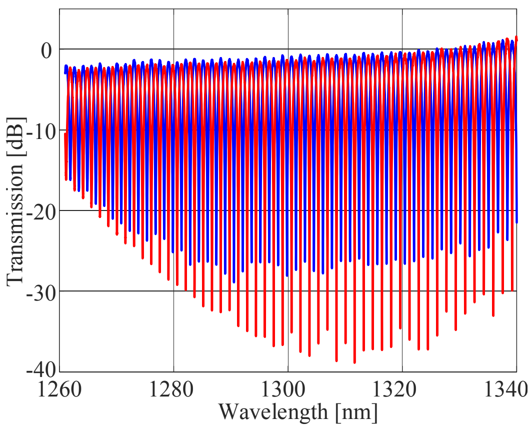

(a)

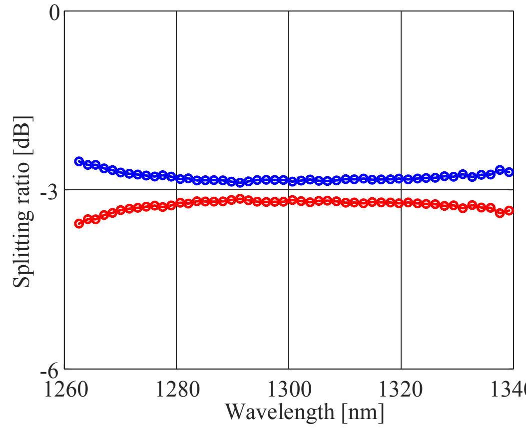

(b)

Figure 3.5. (a) Transmission spectrum measurements for both ports of the MZI, and (b) extracted splitting ratio for a single MMI.

from the measured ER of the first output port as

$$K = k^2 = \frac{1}{2} \pm \frac{1}{2}\sqrt{\frac{1}{ER_{out1}}}. \tag{3.5}$$

Figure 3.5 presents the measured transmission spectrum of the MZI structure and the extracted splitting ratio for the MMI coupler. As expected, we have a FSR of approximately 1.5 nm. Then, the ER is calculated by finding the maxima and minima of the transmission curve of output port 1. Using Eq. (3.5), the splitting ratio is extracted and plotted in Fig. 3.5(b). The measured splitting ratio is close to 3 dB with an imbalance of ± 0.5 dB and covers a bandwidth of 80 nm. The measured bandwidth was limited by the laser tuning range and the grating coupler losses. Then, we measured the same device across the entire wafer shown in Fig. 3.6(a). The mean splitting ratio over 80 nm bandwidth is shown in Fig. 3.6(b). This results show the fabrication tolerance of the MMI design across the entire wafer where the standard deviation of the splitting ratio is below 0.0423 dB across the entire wafer.

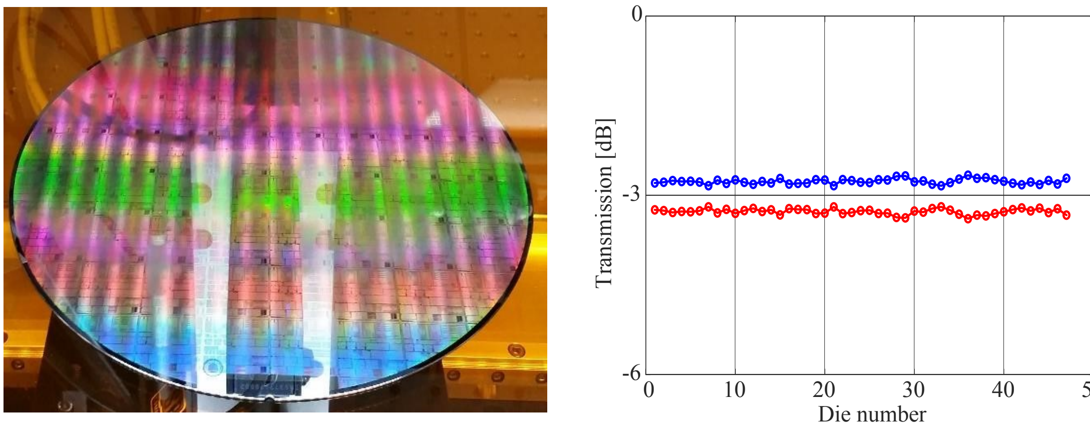

(a) (b)

Figure 3.6. (a) Image of the fabricated wafer, and (b) mean splitting ratio over the entire wavelength range across the wafer.

3.3 Asymmetric MMI splitter

3.3.1 Introduction

Asymmetrical beam splitters can be used for various applications such as power tap monitoring, wavelength demultiplexing [80], and complex modulators [81]. Several approaches can be used to achieve different splitting ratios. The simplest approach is to use a directional coupler and by varying the coupling length, different splitting ratios can be achieved [41]. Also, adiabatic couplers have been proposed for asymmetric splitting ratios by varying the end waveguide widths [82]. In [83], canonical and widened rib based MMIs have been demonstrated to achieve different splitting ratios over 50 nm bandwidth. Moreover, an AMMI based splitter has been proposed by altering the symmetry of the MMI coupler slab region by introducing a cut to one of its sides [84]. The design is based on a rib geometry providing different splitting ratios over a bandwidth of only 40 nm.

In this section, we present and experimentally demonstrate a broadband and compact single etch asymmetric splitter using SWG based MMI. The AMMI has the size of only 23.7 µm × 3 µm including 20 µm for the SWG tapers. Also, we present experimental results for five different splitting ratios in a 100 nm window including the entire C-band. Splitting ratios ranging from 50:50 to 85:15 can be attained in the C-band spectral range. The dimensions of the AMMI can be changed to achieve similar performance in the O-band.

3.3.2 Design and Simulation Results

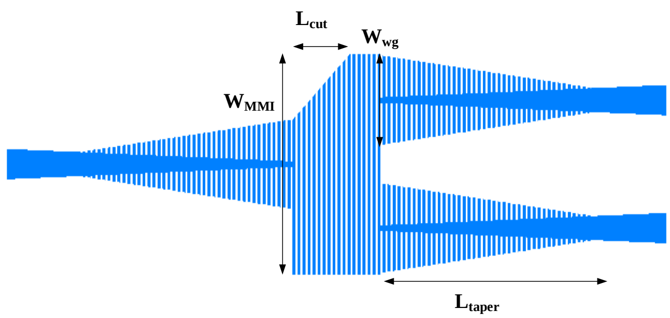

Figure 3.7. Proposed SWG-AMMI schematic.

Figure 3.7 presents the layout of the AMMI design. A cut is introduced in one side of the slab region to break the symmetry and thus vary the splitting ratio between the output ports. By changing the L_{cut} value, different splitting ratios can be achieved. Also, we use SWGs to engineer the waveguide dispersion to achieve a broadband and compact splitter [85, 86]. SWG tapers are used at the input and output of the MMI to transition from regular waveguide to SWG waveguides and vice versa.

L_π can be calculated using Eq. (3.8). Figure 3.8 shows the simulated L_π versus wavelength for a conventional MMI and the proposed SWG MMI, where the MMI width is fixed at 3 μm. Lumerical mode solver and 3D-FDTD band structure analysis have been used to get n_{eff0} and n_{eff1} for the conventional and the SWG MMI, respectively. Since the effective index is function of wavelength, L_π is also function of wavelength. Hence, the variation in the L_π over wavelength determines the operating bandwidth of the MMI. It can be observed that L_π for the conventional MMI is significantly changing versus wavelength, and hence, the MMI bandwidth is limited. On the other hand, the SWG can be used to engineer the

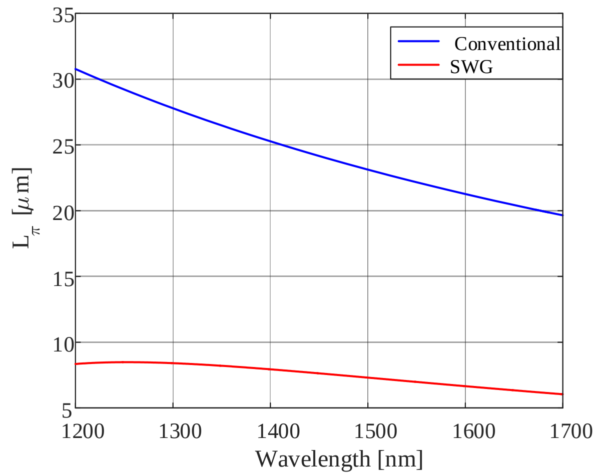

Figure 3.8. L_π versus wavelength for a conventional MMI and the proposed SWG MMI.

effective index dispersion, and have a more flat L_π, and consequently a broadband device. Moreover, L_π at 1550 nm of the conventional and SWG MMI is approximately 22 µm and 7 µm, respectively. This is approximately a 3-fold reduction in the device size compared to the conventional MMI.

Table 3.2. Dimensions of the optimized AMMI design.

Parameter	**value**
W_{MMI}	3 µm
period	0.175 µm
ff	50%
No. of periods	21
L_{cut}	Variable
W_{WG}	1 µm
L_{taper}	10 µm

The optimization of the AMMI design have been carried out using Lumerical 3D-FDTD where particle swarm optimization algorithm has been used to optimize the waveguide width (W_{WG}), grating period, and number of periods. The MMI width (W_{MMI}), fill factor (ff), and taper length (L_{taper}) have been fixed to 3 µm, 50%, and 10 µm, respectively. In table 3.2 , we summarize the parameters for the optimized design achieving different

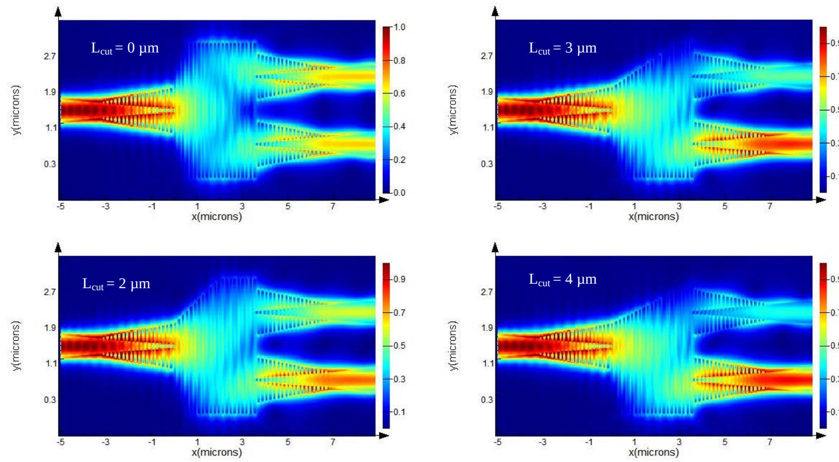

Figure 3.9. Field-profile propagation through the AMMI using FDTD solver for different L_{cut} values.

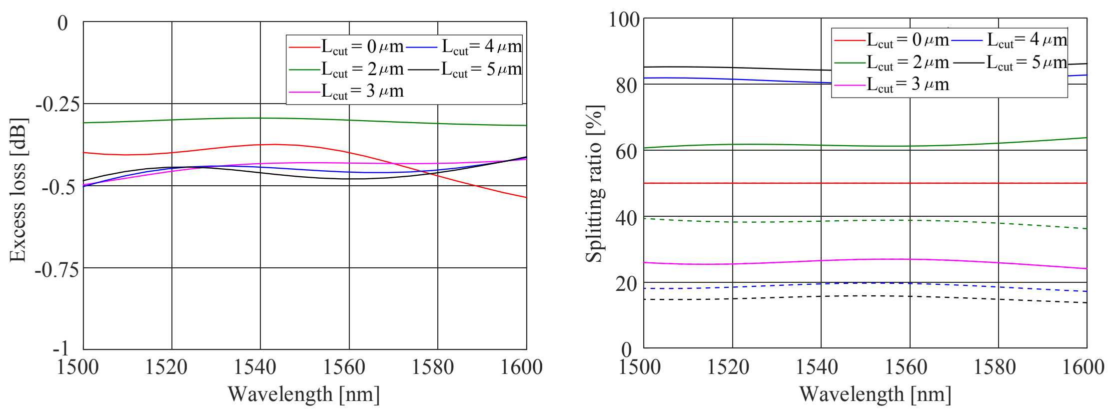

(a) (b)

Figure 3.10. (a) Simulated excess loss for the AMMI versus wavelength, and (b) simulated splitting ratio wavelength dependence for different L_{cut} values. Solid and dotted lines correspond to the lower port and upper port, respectively.

splitting ratios by varying L_{cut} from 0 to 5 µm. The AMMI has the size of only 23.7 µm × 3 µm including 20 µm for the SWG tapers. The tapers can be optimized to be more compact using exponential tapers instead of the linear tapers used in the design. The field propagation through the AMMI for different L_{cut} values is shown in Fig. 3.9. It can be observed that increasing the L_{cut}, more power is directed to the lower port and hence, the splitting ratio is varied. The wavelength dependence of the splitting ratio and the excess

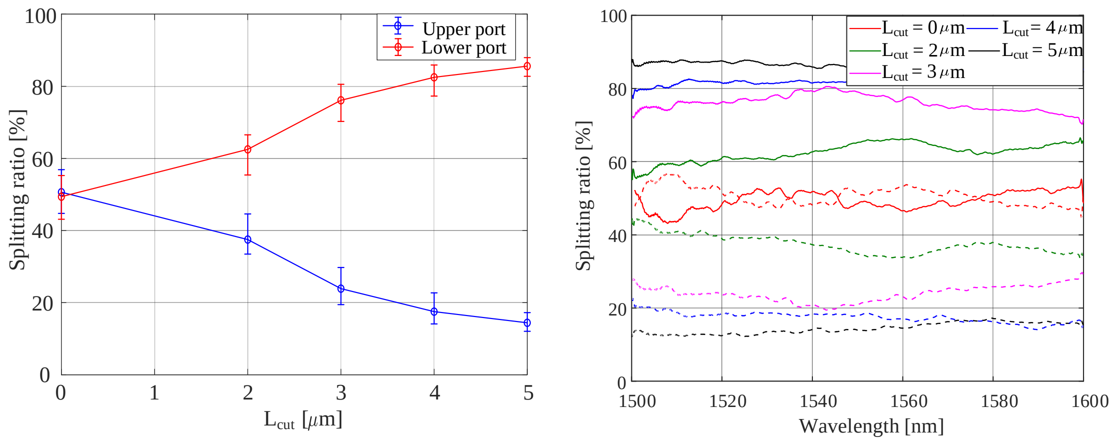

(a) (b)

Figure 3.11. (a) Measured splitting ratio versus L_{cut} length., and (b) Splitting ratio wavelength dependence for different L_{cut} values over 100 nm bandwidth. Solid and dotted lines correspond to the lower port and upper port, respectively.

losses of the AMMI are shown in Fig. 3.10. By changing the value of L_{cut} from 0 to 5 μm, we can achieve a splitting ratio that varies from 50:50 to 85:15, respectively, over more than 100 nm bandwidth. Also, the simulated AMMI excess losses are in the range of 0.25 - 0.55 dB over the entire 100 nm bandwidth.

3.3.3 Fabrication and Experimental Results

The proposed AMMI splitter was fabricated on a SOI wafer with 220 nm top silicon thickness, 2 μm BOX layer, and oxide cladding using single etch EBeam lithography at Applied Nanotools (ANT) Inc. We added five designs with different L_{cut} values. The AMMI was tested using a custom-built automated testing setup designed for passive measurements. A tunable laser connected to the input broadband grating coupler [87] and the output grating couplers connected to a Yenista CT400 passive optical component tester via a fiber array.

Figure 3.11(a) shows the mean of the measured splitting ratio over 100 nm bandwidth around 1550 nm for different values of L_{cut} ranging from 0 to 5 μm. Also, we add the maximum variation of the splitting ratio across 100 nm bandwidth as error bars on the same plot. As expected, using a symmetric MMI, i.e., $L_{cut} = 0$, yields a 50:50 splitting ratio. By introducing L_{cut}, the symmetry is broken, and the splitting ratio at the output ports can be varied. For example, using L_{cut} equals 2 µm results in a splitting ratio of 60:40. Increasing L_{cut} further to 5 µm results in a splitting ratio of approximately 85:15 which is suitable for power monitoring applications. Figure 3.11(b) shows the splitting ratio versus wavelength around 1550 nm. It can be observed that the AMMI covers a broad bandwidth of 100 nm with less than ±7% deviation from the mean.

3.4 C-Band Polarization Beam Splitter

3.4.1 Introduction

A PBS is an essential component in polarization multiplexed modulation formats aiming to increase the transmission capacity. Furthermore, the sub-micron silicon waveguides suffer from high polarization dependence due to waveguide birefringence as shown in Chapter 2. Hence, polarization diversity devices like PBSs and polarization rotators are of great importance to overcome this disadvantage [88]. Numerous PBS designs have been proposed in the literature, e.g., using MZIs [89], directional couplers [90], and MMIs [91]. Among them, MMI based PBS designs have the advantages of being more tolerant to fabrication variations, simpler fabrication, and wider bandwidth. In [91], a PBS design based on the MMI quasi-state imaging is proposed, and the device achieved 15 dB ER. However, the PBS is more than 1 mm in length, and has high IL. In addition, a PBS using two cascaded MMIs has been proposed where the device is shortened, and the ER is approximately 10 dB for both ports [92]. In this section, we present the design, simulation results, and experimental results for the proposed C-band PBS. We focused on C-band operation only in this design and the dimensions of the PBS can be re-designed to operate in the O-band region. The design is based on cascaded MMIs, where three MMIs are utilized to improve the ER. The PBS has achieved ERs larger than 14 dB, and 20 dB over more than 55 nm spectral range including the entire C-band for the TE and TM ports, respectively.

3.4.2 Design and Simulation Results

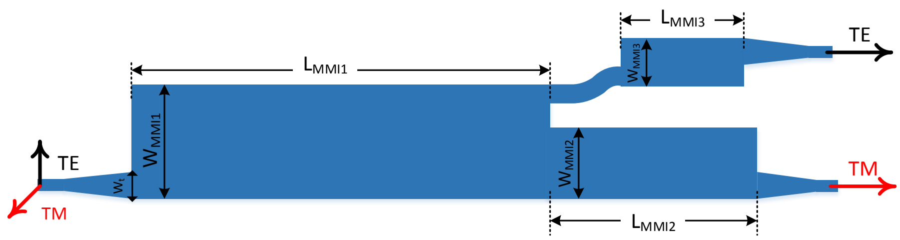

Figure 3.12. Proposed PBS schematic.

Figure 3.12 shows the schematic of the proposed PBS. Due to the difference in the effective index, the self-imaging length ($3L_\pi$), is different for each polarization, thus the first MMI length (L_{MMI1}) is designed to be equal to the first self-image of the TE polarization. As a result, the TE polarization will be guided in the upper port. Also, most of the TM polarization will be reflected to the lower side at L_{MMI1}, and by adding a second MMI in cascade with MMI1, the TM polarization can be collected [93]. The second MMI length (L_{MMI2}) is chosen to have the first TM image focused in the lower port. Since, L_{MMI1} is chosen to be the first TE image not a higher common multiple for TE and TM polarizations, residual TM polarization will be present in the upper port, leading to a degradation in the upper port ER. This can be solved by adding a third MMI with length L_{MMI3} such that the TE image is focused in the upper port [94]. The third MMI will filter the residual TM polarization and increase the ER for the upper port. An S-bend is added to connect MMI1 and MMI3 to reduce the crosstalk between MMI2 and MMI3.

Simulations were carried out using the Lumerical MODE EME solver to find the proper dimensions for the device. The resulting device dimensions are summarized in Table 1. The entire device is approximately 364 µm long and 10 µm wide. The SOI waveguide width is 500 nm where linear tapers are added at the input and outputs of the PBS.

Table 3.3. Dimensions of the PBS

Parameter	value
L_{MMI1}	262 µm
W_{MMI1}	6 µm
L_{MMI2}	50 µm
W_{MMI2}	3.8 µm
L_{MMI3}	87 µm
W_{MMI3}	2.7 µm
W_t	1.5 µm

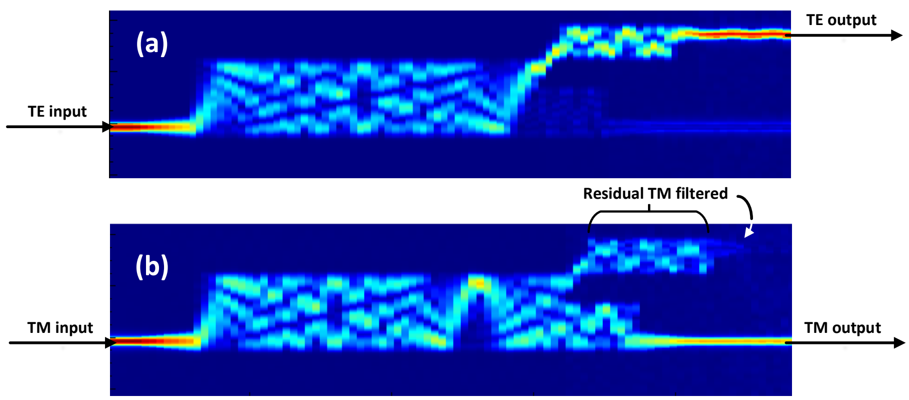

Figure 3.13. Field propagation through the PBS using EME solver for (a) TE, and (b) TM Polarized inputs.

The propagation of both polarizations through the PBS is outlined in Fig. 3.13. For the upper port, the TE polarization is almost fully focused in the output port, while the residual TM polarization is apparent in the input of MMI3 (Fig. 3.13(b)), but is negligible in the output port after being filtered by MMI3. For the lower port, the TM output is more than 60% of the input (since L_{MMI1} is the TE self image), and the TE value is negligible.

3.4.3 Fabrication and Experimental Results

The proposed PBS design was fabricated on a SOI wafer with 220 nm top silicon thickness, 3 µm BOX layer, and oxide cladding using single etch EBeam [95]. The PBS was tested using a tunable laser connected to the input grating coupler and the output grating couplers

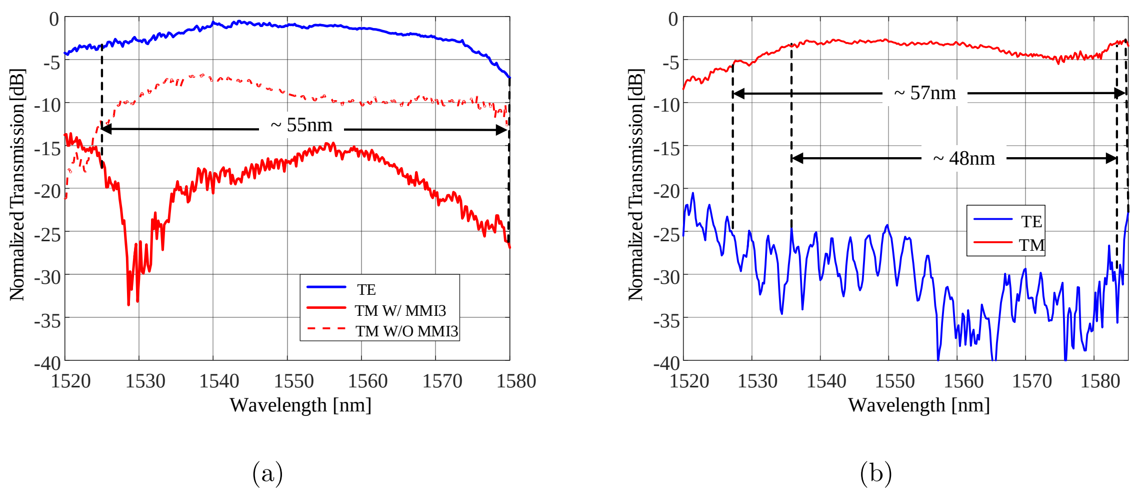

Figure 3.14. Transmission spectrum measurements of the PBS for the (a) upper port and (b) lower port.

connected to two optical power meters via a fiber array on a manual SiP test station. A polarization controller and an off-chip PBS were used to accurately set the polarization of the input light to the input grating coupler.

Figure 3.14 presents the transmission spectra normalized with a reference straight waveguide calibration structure. It can be observed from Fig. 3.14(a) that the IL for the upper port is less than 0.9 dB at 1550 nm. The measurements in Fig. 3.14(a) also indicate that adding MMI3 nearly doubles the ER. The ER at 1550 nm is approximately 8.5 dB without MMI3 and increases to 16.5 dB with MMI3. In addition, the ER is more than 14 dB in the 1525-1580 nm spectral range, i.e., covering about 55 nm which includes the entire C-band range. Fig. 3.14(b) shows that the IL is less than 2.8 dB at 1550 nm for the lower port, which is higher loss compared to the upper port due to the fact that L_{MMI1} is the TE self-imaging length. Finally, the ER exceeds 20 dB and 23 dB over more than 57 nm and 48 nm, respectively.

3.5 High yield and broadband polarization splitter and rotator

3.5.1 Introduction

In this section, we focus on another variant of polarization handling devices which is a PSR including a PBS and polarization rotation. Different PSR designs have been demonstrated in the literature [88, 96]. In [97], the PSR is designed using a directional coupler, bilevel taper, and a Mach-Zehnder interferometer, however, the PSR bandwidth is limited to 40 nm. Also, a double taper coupler based PSR has been demonstrated in [98].

In this section, we present two PSR designs that are based on a similar structure with dimensions optimized for a certain band, i.e., C-band and O-band. The target PSR specifications are <1 dB IL, >20 dB ER, high yield, and a bandwidth that covers the entire WDM grid either in the C-band or the O-band. Measurements results reveal that the C-band design can achieve an ER beyond 20 dB over 100 nm bandwidth. Similar results are measured for the O-band designs and wafer scale data for the O-band design are reported where the minimum ER over 80 nm bandwidth has an average of 21.82 dB and 19.05 dB with a standard deviation of 2.42 dB and 1.559 dB for the upper and lower ports, respectively.

3.5.2 Device design and Simulation results

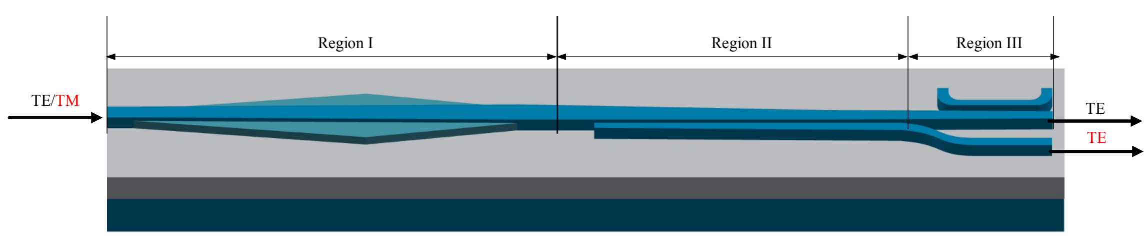

Figure 3.15. Schematic for the designed PSR. The top oxide cladding is not shown for clarity.

Figure 3.15(a) shows the schematic of the PSR. The design architecture is based on the

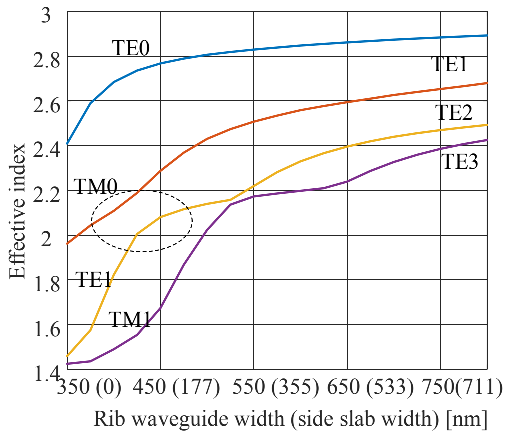

(a)

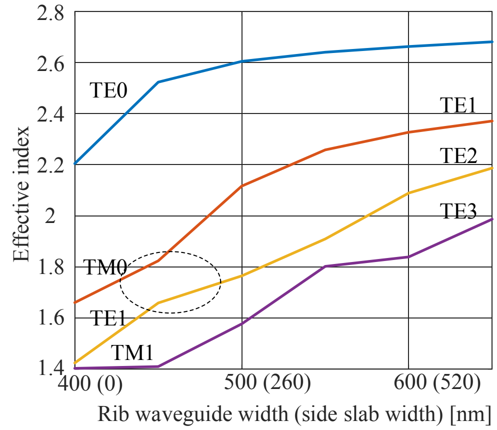

(b)

Figure 3.16. The effective refractive index evolution through the first section of the polarization rotator for the first four modes versus waveguide rib width and slab width at (a) 1310 nm and (b) 1550 nm wavelengths.

C-band PSR design in [99] which shows 13 dB ER in the C-band. However, we optimize the design significantly for the C-band and the O-band aiming at a higher ER over wider bandwidth and more importantly a fabrication tolerant design. The PSR can be divided into three main regions. Region I is the polarization rotator section. To enable polarization rotation, the vertical symmetry is broken using a rib waveguide with oxide cladding instead of using different cladding materials which simplifies the fabrication process [90]. By introducing a partially etched waveguide, the TM0 mode is rotated to the first TE (TE1) mode, and the TE0 mode is unaffected. The effective index evolution for the rib waveguide is shown in Fig. 3.16. Then, the partially etched waveguide is gradually decreased to a single etch waveguide to remove the vertical asymmetry and mitigate any TE1 mode rotation back to the TM0 mode through the rest of the PSR. At the output of region I, TE0 and TE1 modes are present in the wide waveguide. Then, region II is introduced which is an adiabatic coupler that is used to couple the TE1 mode to the lower waveguide and the TE0 mode passes through the upper waveguide. The adiabatic coupler is used to enable low loss, high fabrication tolerance, and large bandwidth for polarization splitting. The TE1

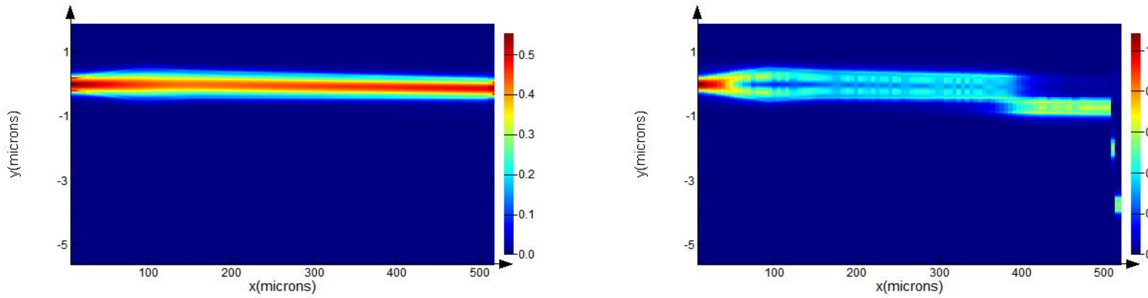

(a) (b)

Figure 3.17. Field propagation through the PSR at 1310 nm for (a) TE0 mode launch and (b) TM0 mode launch.

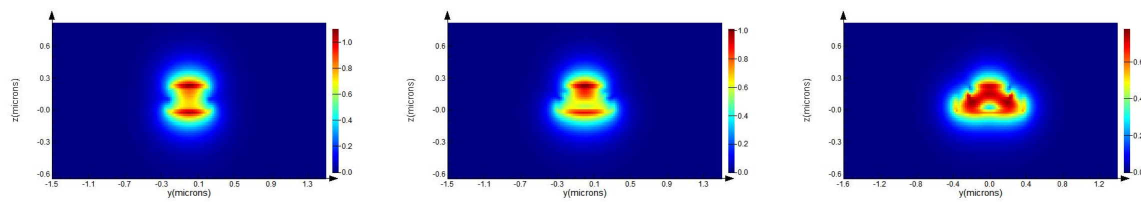

(a) (b) (c)

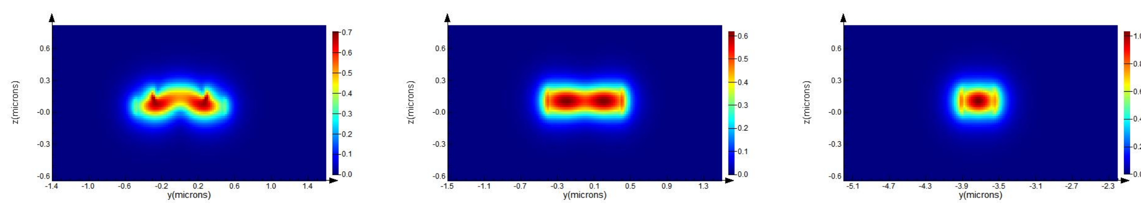

(d) (e) (f)

Figure 3.18. Mode profile evolution from a TM0 mode at the input to a TE0 mode at the output lower port.

mode slowly couples to the lower waveguide of the adiabatic coupler and evolves to a TE0 mode at the output of the lower port. In the last region, an s-bend is added to separate the outputs of the adiabatic coupler. In some designs, we added a directional coupler based filter to remove residual TM0 mode and increase the ER in the upper port, and waveguide bends to suppress the high order modes.

Lumerical Mode EME is used to simulate all the sections of the PSR and the entire PSR

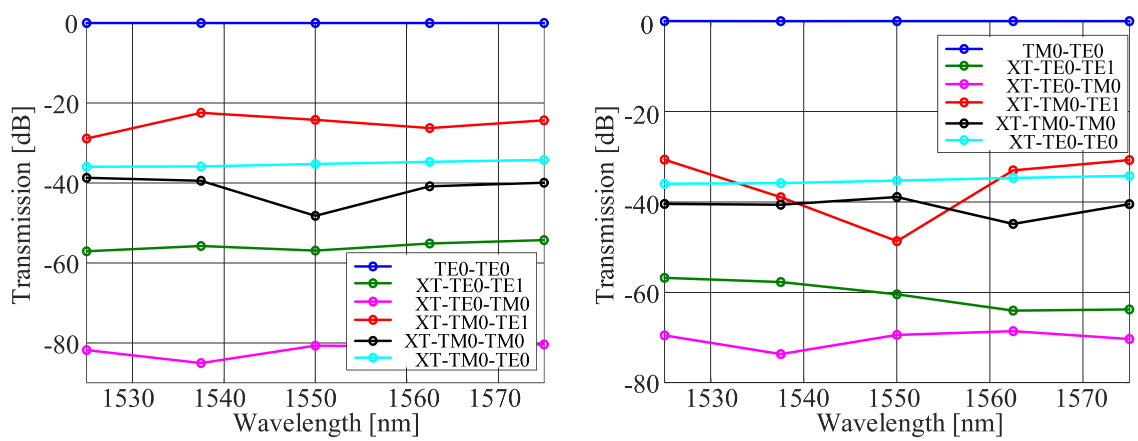

(a) (b)

Figure 3.19. Simulated transmission spectrum for the (a) upper port and (b) lower port of the C-band PSR.

including the polarization rotator and adiabatic coupler sections. The field propagation through the PSR is shown in Fig. 3.17(a-b). Also, the mode profile evolution through the different regions of the PSR at TM0 mode launch is shown in Fig. 3.18(c-f).

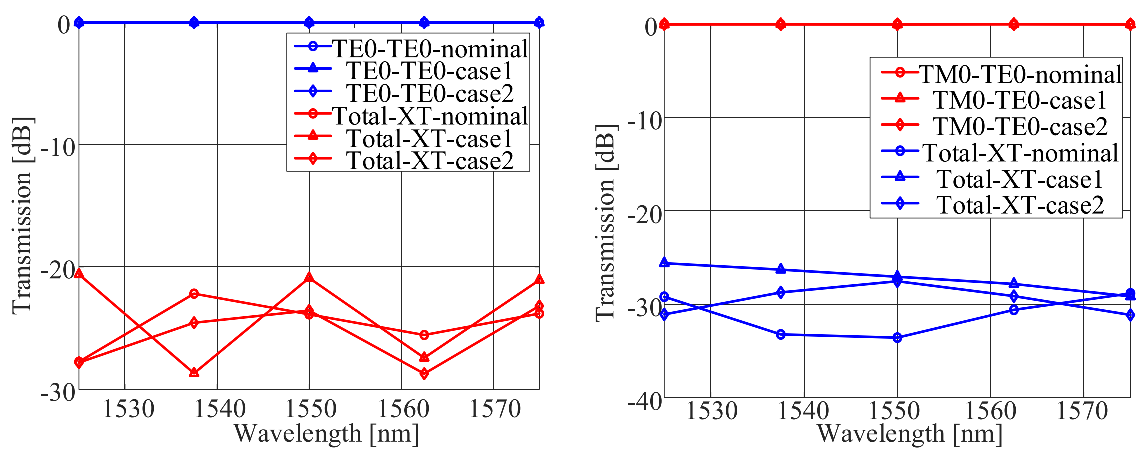

(a) (b)

Figure 3.20. Simulated tolerance for the (a) upper port and (b) lower port of the C-band PSR for the nominal design and two corner cases.

Figure 3.19 shows the simulated transmission spectrum for the PSR optimized for C-band operation. It can be observed that the IL of the PSR is negligible (< 0.1 dB). Also, the

ERs are beyond 20 dB over more than 50 nm including the entire C-band. Moreover, the TE1 mode crosstalk is the highest crosstalk in the upper port. Hence, we added waveguide bends of 5 μm bend radius in the layout to suppress the high order modes. To assess the fabrication tolerance of the designed PSR, we simulated two extreme cases according to the fabrication specifications. In case 1, we change the following: core waveguide thickness = nominal + 5 nm, slab thickness = nominal + 20 nm, waveguide width = nominal + 18 nm. In case 2, we change the same parameters in the opposite direction. In Fig. 3.20, we show the simulated fabrication tolerance of the PSR including the nominal case and the corner cases. The PSR shows no change in terms of the ILs. For the ERs, we present the total crosstalk for better clarity. Both ports show good fabrication tolerance where the ER is still higher than 20 dB for both ports at the worst cases. Finally, we simulated the differential group delay between both ports since the PSR will be used as a part of a PIC where the simulated value is approximately 0.78 ps at 1550 nm.

3.5.3 Device fabrication and experimental results

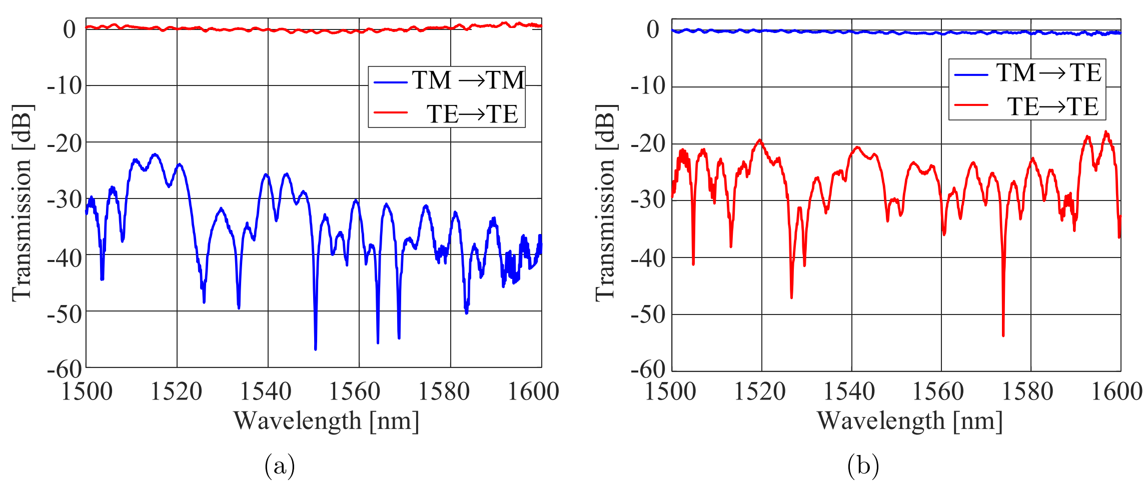

Figure 3.21. Transmission spectrum for the (a) upper port and (b) lower port of the C-band PSR without the clean-up filter.

The PSRs were fabricated on a 200 mm silicon-on-insulator wafer with 220 nm nominal

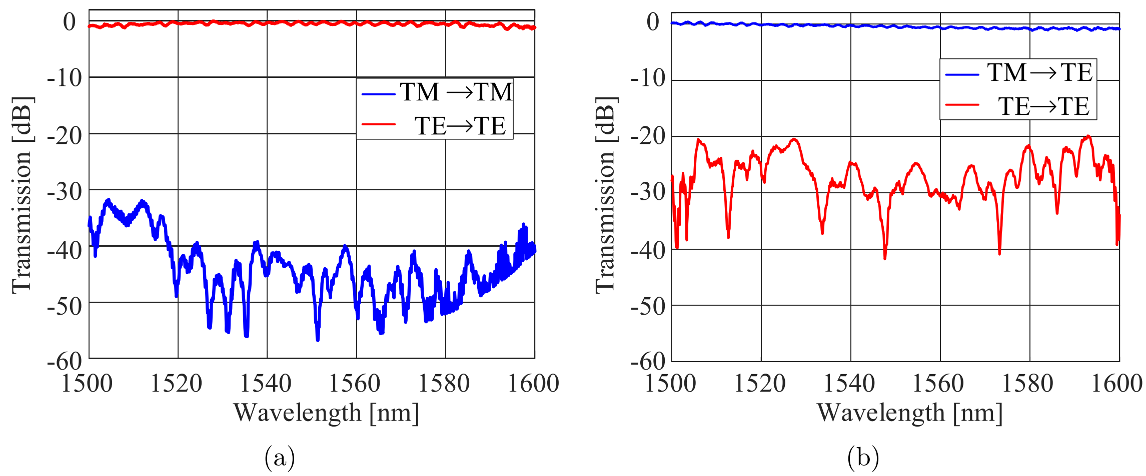

Figure 3.22. Transmission spectrum for the (a) upper port and (b) lower port of the C-band PSR with the clean-up filter

top silicon thickness. Several variations of the PSRs were fabricated on the same wafer. We varied the polarization rotator etch depth and length, adiabatic coupler gap and length, and directional coupler filters. Vertical grating couplers are used for coupling in and out of the chip with approximately 4 dB loss at 1550 nm and 1310 nm. To enable the characterization of the PSR, each design was repeated twice on each reticle to characterize the IL and ER at TE and TM launch.

The PSRs are tested in a passive automated tester including tunable lasers, motorized stages, and power meters. Figure 3.21 shows the transmission spectrum of both ports for TE and TM mode launch at the input port normalized to the grating couplers response for the PSR design optimized for the C-band and doesn't include the clean-up filter. The IL for both ports is below 0.5 dB at 1550 nm where we have $\pm$ 0.5 dB uncertainty from the grating couplers' variation which results in some gain at the spectrum edges. It can be observed that we can achieve more than 20 dB ER for the upper and lower ports over more than 90 nm including the entire C-band. In Fig. 3.22, we present the transmission results for the same design including the clean-up filter in the upper port. More than 10 dB improvement is observed in the ER of the upper port due to the addition of the directional coupler based clean-up filter which decreases the residual TM mode in the upper waveguide.

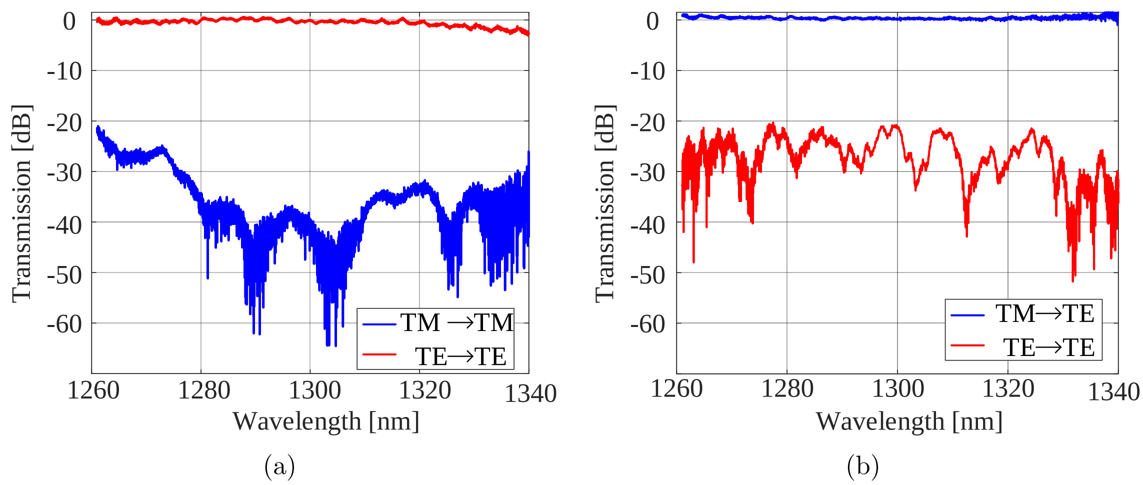

Figure 3.23. Transmission spectrum for the (a) upper port and (b) lower port of the O-band PSR.

Similarly, we measured the O-band PSR design and the results are shown in Fig. 3.23. The O-band grating couplers have a limited bandwidth which limited our measurements to 80 nm. However, the PSR design is entirely adiabatic and the operating bandwidth is larger than 80 nm which aligns with the design simulations. It can be observed that we can achieve more than 20 dB ER over 80 nm bandwidth for the upper and lower ports. Also, the upper port shows a better ER compared to the lower port which is attributed to the addition of the directional coupler clean-up filter which decreases the residual TM mode in the upper waveguide.

3.5.4 Wafer-level experimental results

To asses the yield of the PSR designs presented, we report the wafer scale data of the O-band PSR in Fig. 3.24 across all measured dies to asses the device yield. We show the minimum ER across the 80 nm bandwidth for both ports. The minimum ER over 80 nm bandwidth has an average of 21.82 dB and 19.05 dB with a standard deviation of 2.42 dB and 1.559 dB for the upper and lower ports, respectively.

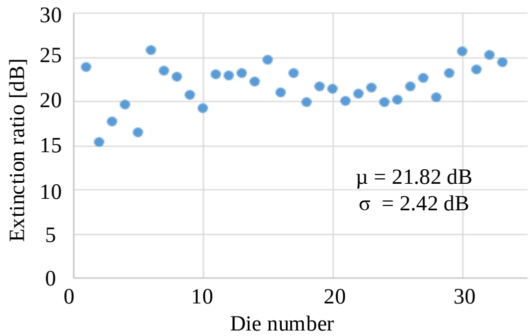

(a)

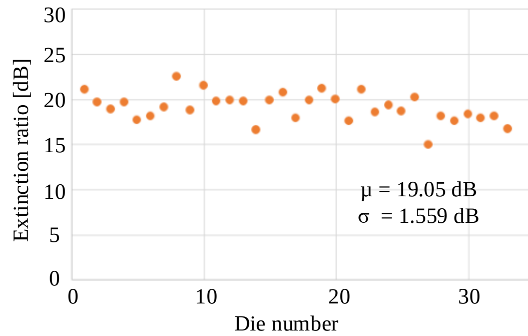

(b)

Figure 3.24. Wafer-level ER for the (b) upper port and (c) lower port.

3.6 Low power variable optical attenuators

3.6.1 Introduction

VOAs are widely used in optical networks. A VOA is used in the line cards for amplitude control of different WDM channels in optical add-drop multiplexers (OADMs) and Erbium doped fiber amplifiers (EDFAs). In such designs, VOAs based on SiP, silica or micro-electromechanical systems (MEMS) are chosen since they can provide superior performance in terms of polarization dependent loss and speed [100,101]. Moreover, a VOA is an essential component in ICRs to control the received signal power to enable a larger dynamic range for colorless reception. Hence, a VOA based on the same material platform of the ICR is preferred. For the InP platform, VOAs can be realized by using a MZI structure or a semiconductor optical amplifier driven below transparency [102]. In [103], a MZI based VOA in the InP platform is reported where it can achieve a maximum attenuation of 25 dB at 50 mW power consumption. Moreover, the silica-based planar lightwave circuit (PLC) is used for the VOA design based on a MZI structure and the thermo-optic effect [104]. However, the design suffer from high power consumption and introduce packaging challenges with the rest of the ICR. The SiP platform has been accepted as a competitive platform for ICRs due to the significant cost reduction compared to the InP platfrom while achieving good performance [105]. SiP based VOAs that are commonly used in ICRs are based on carrier injection p-i-n junction which introduces the attenuation in the signal by injecting carriers [106]. As the injected current increases, the carriers injected to the VOA absorb the guided light. Such designs require relatively high power consumption and ILs to achieve the attenuation function. For example, more than 30 mW are required to achieve 20 dB attenuation in [106]. Moreover, more than 1.5 dB IL and 60 mW power consumption are needed to achieve 20 dB attenuation in [100]. In [107], a SiP VOA based on a reflective MZI structure is proposed. The design suffer from critical drawbacks such as limited optical bandwidth and reflected power returns to the input signal path which makes such design not suitable for practical applications.

In this section, we present SiP based VOA designs based on a MZI structure and the thermo-optic effect. We present designs targeting both the C-band and O-band aiming at ICRs and SVRs. We report a power consumption for the C-band VOA, including substrate undercut, of only 5 mW and 8 mW to achieve 5 dB and 20 dB attenuation, respectively. This represents more than 3X improvement in the power consumption without including the substrate undercut. Moreover, we study the effect of the heater dimensions on the attenuation and bandwidth.

3.6.2 Design and simulation results

The design of the reported VOA is based on a simple MZI cell with 3-dB couplers at the input and output ports, and thermal phase shifters are added to the MZI arms as shown in Fig. 3.25(a). The operating band and optical bandwidth is mainly determined by the 3-dB coupler operating spectral range. Hence, we designed several splitters such as 1 $\times$ 2 MMI, 2 $\times$ 2 MMI, and Y-branch. Figure 3.25(b) presents the simulated transmission versus wavelength for different splitter designs. As expected, all designs have a close bandwidth and IL and can be used for the VOA design.

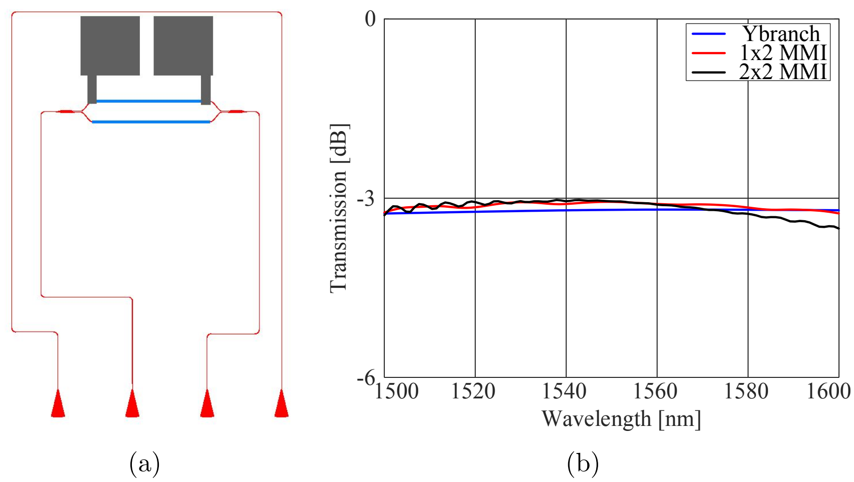

Figure 3.25. (a) Layout schematic of the VOA and (b) transmission versus wavelength for different 3-dB couplers.

3.6.3 Device fabrication

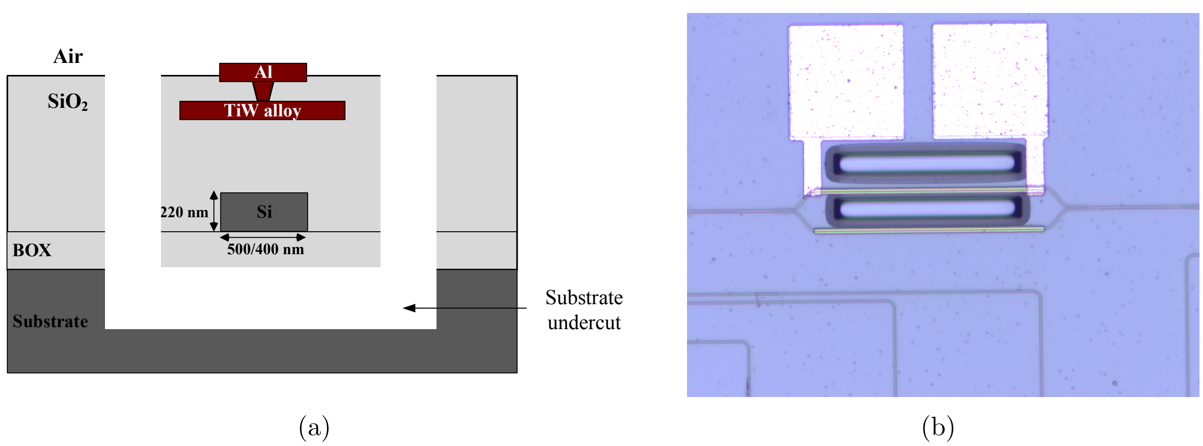

Figure 3.26. (a) Thermo-optic phase shifter cross-section and (b) image showing the fabricated VOA with the substrate undercut.

The VOAs are built using EBeam lithography at ANT. The VOAs were fabricated on a 675 µm handle SOI wafer with 220 nm top silicon thickness, 2 µm BOX layer, and oxide cladding using single etch EBeam. The heater layer uses a 200 nm thick titanium-tungsten alloy to implement the high-resistance heater. The routing layer and bonding pads are made out of a titanium-tungsten/aluminum bilayer. Using a bilayer for the routing layer ensures good electrical contact between the routing layer and the heater layer with low contact resistance. Oxide cladding is then deposited on the chips and the probing pads are exposed using the oxide window layer. Moreover, we developed an undercut process to suspend the silicon waveguides to improve the power consumption of the VOAs. Figure 3.26 shows the thermo-optic phase shifter cross-section and an image of the fabricated VOA including the undercut. Due to mechanical stability, we could only suspend one waveguide in the current process, which presents a suboptimal design in terms of power consumption. Different variations are built including C-band and O-band designs, with and without susbtrate undercut, different 3-dB couplers, different heater lengths, and different heater widths.

3.6.4 Experimental setup and results

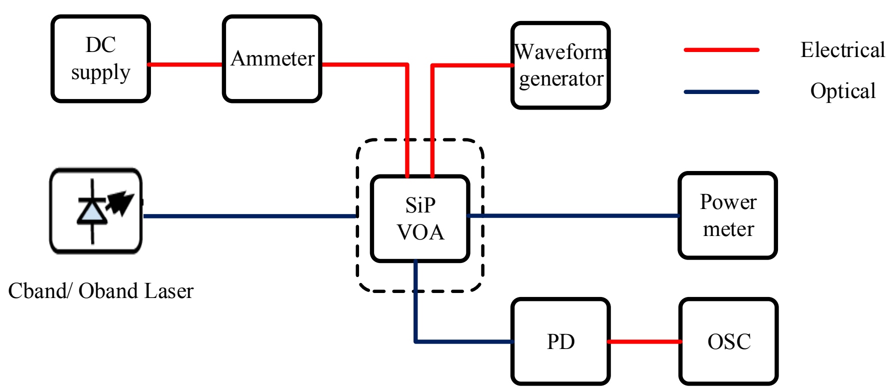

Figure 3.27. Experimental setup for the VOA testing.

The experimental setup used for the VOA testing is shown in Fig. 3.27. Two tunable lasers are used for the O-band and C-band testing. The output of the tunable laser is connected to the input grating coupler via a fiber array unit. The output of the VOA is connected to a power meter. Also, a grating coupler pair is added for alignment and losses calibration. A DC probe is used to provide the DC voltage from the DC supply for the

VOA. For small-signal measurements, a signal generator is used to provide a 100 mVpp signal to drive the VOA. The received signal is received by a 10 GHz PD followed by a signal oscilloscope.

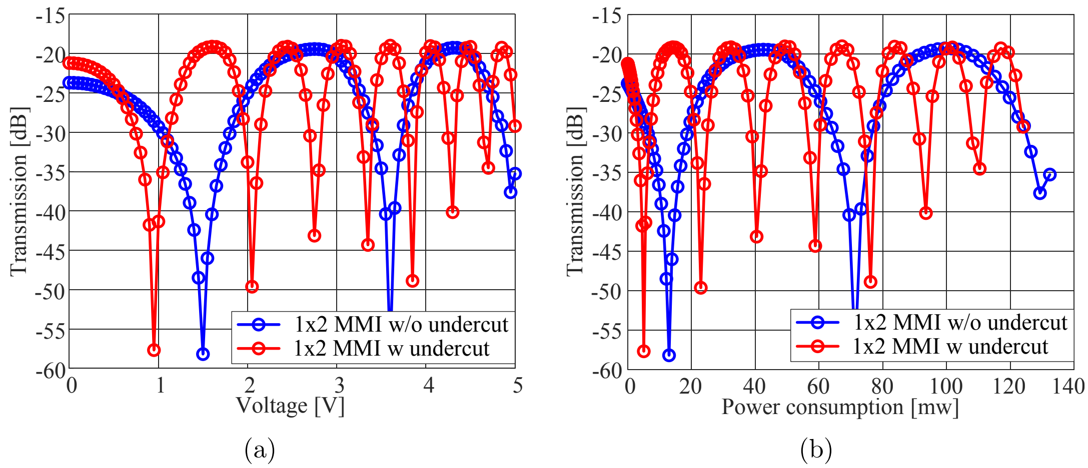

Figure 3.28. Transmission of the VOA with and without the substrate undercut versus (a) applied voltage and (b) power consumption.

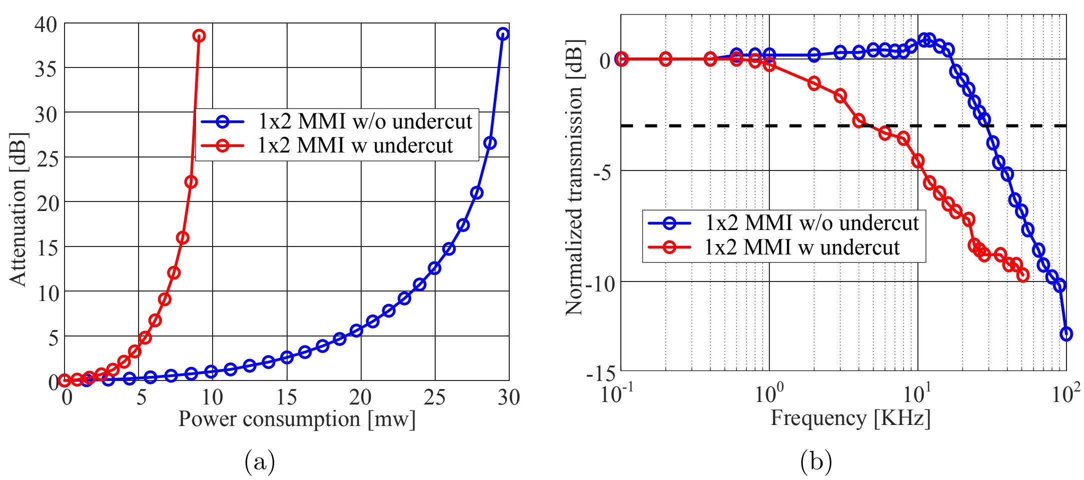

Figure 3.29. (a) Attenuation versus power consumption and (b) bandwidth of the VOA for the designs with and without the substrate undercut.

Figure 3.28 presents the transmission versus the applied voltage and power consumption at 1550 nm wavelength for a VOA with and without the substrate undercut. A 1×2 MMI

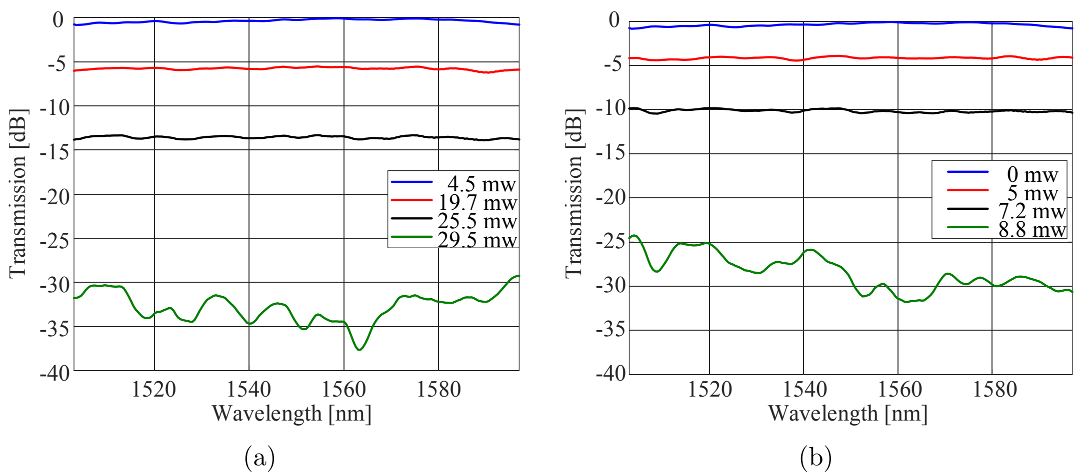

Figure 3.30. Transmission versus wavelength of the VOA (a) with substrate under cut and (b) without the substrate undercut.

is used as the 3-dB coupler for the shown results. The transmission results include losses from the grating coupler pair as well as the VOA. The fabricated designs were balanced in the layout, however, we note that the transmission is not at maximum at zero applied voltage due to fabrication imperfections. Hence, a bias voltage is needed to adjust the VOA at the maximum point. It can be observed that the required voltage to achieve a null decreases with the increase of the bias voltage. However, P_π, power needed to achieve a complete π phase shift or destructive interference, is constant at approximately 29.8 mW for the VOA design without the undercut. Adding the substrate undercut improves the P_π significantly to reach approximately 9 mW. Such improvement comes at the expense of decreased bandwidth as shown in Fig. 3.29 due to the decreased thermal conductivity [108].

In Fig. 3.29(a), we present the achievable attenuation versus the power consumption assuming the VOA is biased at maximum. The VOA without substrate undercut consumes approximately 18 mW and 27 mW to achieve 5 dB and 20 dB attenuation, respectively. Including the substrate undercut, the power consumption to achieve 5 dB and 20 dB attenuation is improved to be 5 mW and 8 mW, respectively. This represents more than 3X improvement in the power consumption. Compared to commercial SiP VOAs, this is more than 10X improvement in the power consumption at 20 dB attenuation [100]. Moreover, this represents more than 3.5X improvement compared to existing designs based on p-i-n junction in the literature [106]. The measured bandwidth of the VOA is shown in Fig. 3.29(b). The VOA with a 200 μm length phase shifter has a 3-dB bandwidth of approximately 30 KHz which decreases to approximately 6 KHz when the substrate undercut is added. Hence, a trade-off exists between the efficiency and the bandwidth of the VOA.

Figure 3.30 presents the transmission through the VOA versus wavelength including the entire C-band at different electrical power values. The grating coupler losses are calibrated in the shown results. It can be observed that both designs have a relatively flat attenuation with ripples below 1 dB, except for the bias at null, versus more than 100 nm which is governed by the MMI design.

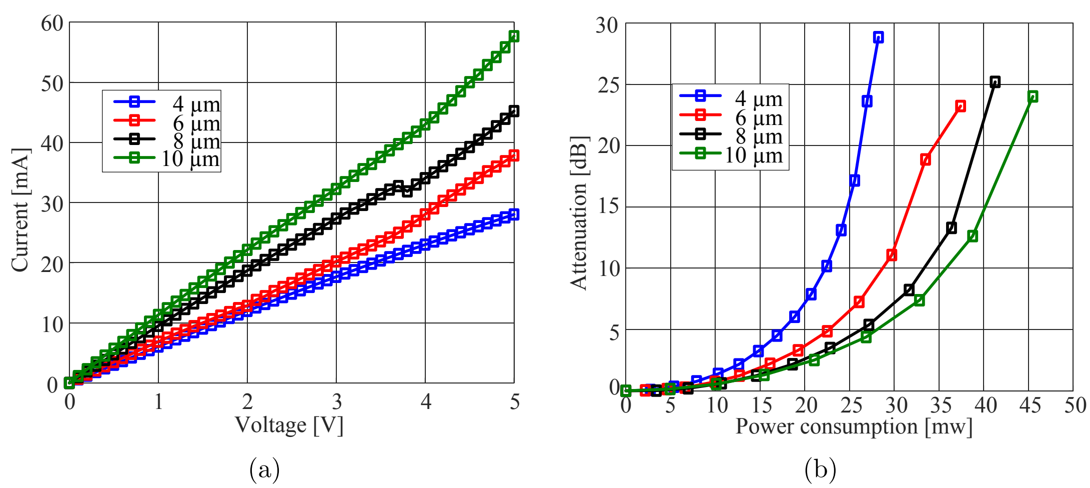

Figure 3.31. (a) IV characteristics of the VOA and (b) attenuation versus power consumption for different thermal phase-shifter widths.

Then, we sweep the dimensions of the heater phase shifter and study the VOA performance. In this study, the VOA design is based on Y-branches instead of the MMI design without the substrate undercut which results in different attenuation values. However, the same conclusion holds in Figs. 3.31 and 3.32. In Fig. 3.31, we present the performance

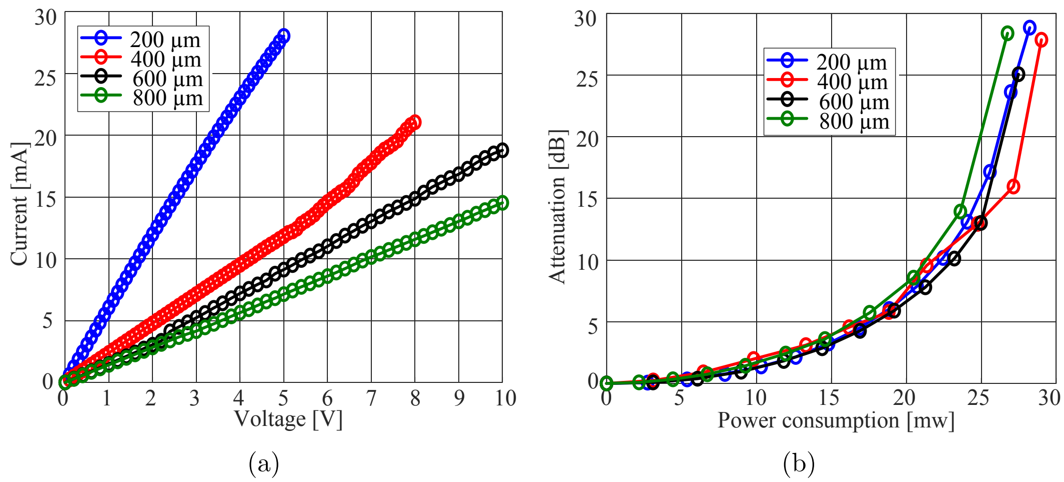

Figure 3.32. (a) IV characteristics of the VOA and (b) attenuation versus power consumption for different thermal phase-shifter lengths.

of the VOA versus the width of the metal heater. Intuitively, changing the metal heater width results in a change in its resistance as shown in Fig. 3.31(a). Increasing the width of the heater more than 4 µm results in higher power consumption to achieve the same value of attenuation as shown in Fig. 3.31(b). This is attributed to the decreased efficiency of the therm-optic effect on the heated arm, and increased crosstalk between the MZI waveguides. Figure 3.32 presents the VOA results versus the heater length. Similarly, the resistance increases with the metal heater length increases. Increasing the metal heater length increases the device footprint, ILs, and voltage. However, the power consumption is not affected. This can be understood by the cancellation of the required temperature change and the heated area versus the heater length on the power consumption calculation. Hence, the VOA heater should be designed as small as possible bearing in mind the crosstalk between the MZI arms which will increase at shorter arm lengths. In addition, we present the bandwidth of the VOA versus the metal heater dimensions in Fig. 3.33. Increasing the heater width results in a reduction in the achievable bandwidth of the VOA. On the other hand, changing the heater length has no effect on the heater bandwidth.

Finally, we present similar results for an O-band VOA where the differences are changing

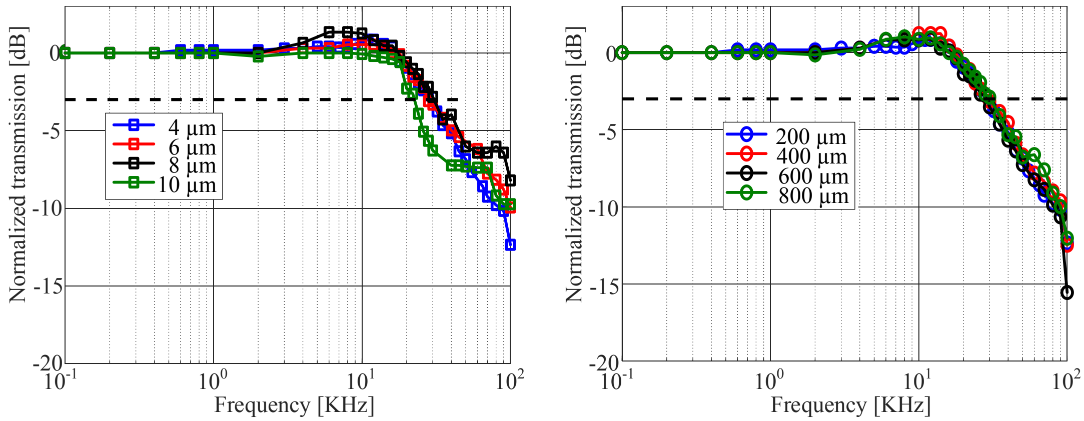

(a) (b)

Figure 3.33. VOA bandwidth versus (a) metal heater width and (b) metal heater length.

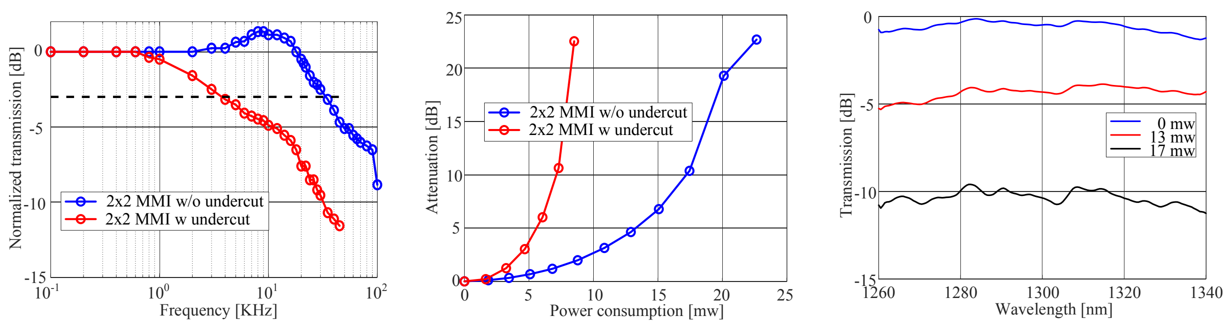

(a) (b) (c)

Figure 3.34. (a) Bandwidth with and without the undercut, (b) attenuation versus power consumption, and (c) transmission versus wavelength for the O-band VOA.

the 3-dB coupler to the Oband 2×2 MMI presented in section 3.2, and the waveguide width is reduced to 400 nm. Figure 3.34 presents the VOA bandwidth, attenuation versus power consumption, and transmission versus wavelength. More than 20 dB attenuation can be achieved using approximately 7.5 mW using a VOA with a substrate undercut. The transmission versus wavelength shows some ripples in the response which can be attributed to the used subwavelength grating couplers which have less fabrication tolerance compared to the C-band counter parts due to smaller feature size. Also, the 2×2 MMI has a smaller bandwidth compared to the 1×2 MMI.

3.7 Conclusion

In this Chapter, we proposed and experimentally demonstrated five SiP passive and active components that are essential in most PICs.

- In section 3.2, we demonstrated a 2 × 2 MMI based 3-dB coupler operating in the O-band. The device has a simulated bandwidth of more than 80 nm and a power imbalance below 0.2 dB. The splitting ratio is close to 3 dB over 80 nm bandwidth with an imbalance of ±0.5 dB. Moreover, we presented the wafer-level splitting ratio across more than 45 dies where the coupling ratio has a standard deviation of only 0.042 dB across the entire wafer which shows the high yield of the MMI design.

- Then, we present AMMI coupler including SWGs to achieve small foot print, asymmetric splitting ratios, and large bandwidth. The AMMI is designed to operate over 100 nm bandwidth including the entire C-band with splitting ratios varying from 50:50 to 90:10 depending on the length of the asymmetry. The AMMI has a compact size of only 23.7 µm × 3 µm. Experimental results show that large bandwidth covering 100 nm is achieved, where different splitting ratios are obtained with a deviation of less than ± 7%.

- In section 3.4, we presented a C-band SiP PBS based on cascaded MMIs. By cascading MMIs, residual crosstalk can be filtered to increase the ER at the output ports. The experimental results show that an ER of approximately 14 dB and 20 dB can be achieved over more than 50 nm from the upper and lower ports of the PBS, respectively.

- High yield, low IL, and broadband PSRs are demonstrated for C-band and O-band SiP transceivers in section 3.5. The design is based on three sections: polarization rotator, adiabatic coupler, and clean-up filters and bends. Simulations show the robustness of the design for fabrication variations. The measured C-band PSR has negligible ILs and ER of more than 20 dB over 90 nm bandwidth. Moreover, more than 10 dB improvement in the ER is achieved by adding the clean-up filter at the output. For the O-band PSR, we can achieve more than 20 dB ER over 80 nm bandwidth including the entire CWDM grid. Furthermore, we show wafer scale data for the O-band design where the minimum ER over 80 nm bandwidth has an average of 21.82 dB and 19.05 dB with a standard deviation of 2.42 dB and 1.559 dB for the upper and lower ports, respectively.

- Finally, low power VOAs are demonstrated in section 3.6. Several variations are designed including different splitters, different heater length and width, with and without substrate undercut, and operating wavelength. A substrate undercut process was developed to suspend the MZI waveguides to achieve low power consumption. Experimental results show that the VOA without substrate undercut consumes approximately 18 mW and 27 mW to achieve 5 dB and 20 dB attenuation, respectively. Including the substrate undercut, the power consumption to achieve 5 dB and 20 dB attenuation is improved to be 5 mW and 8 mW, respectively. This represents more than 3X improvement in the power consumption. On the other hand, the 3 dB bandwidth of the VOA is approximately 30 KHz and 6 KHz with and without the substrate undercut.

Chapter 4

Active silicon photonic integrated circuits for intra-datacenter optical interconnects

4.1 Introduction

In the previous chapter, we presented several passive and active components for PICs. In this chapter, we focus on transmitter side PICs for intra-datacenter optical interconnects. The main component of the transmitter side PIC is the modulator. Several SiP modulators have been published such as: TWMZMs [25, 109], electro-absorption modulators (EAMs) [110, 111], MRMs [112, 113], and other structures utilizing different materials like organic based modulators [114]. Although MRMs are compact, and have low driving voltages, they suffer from thermal instability. Moreover, submicron waveguide based EAMs are limited to the L-band or edge of C-band due to the germanium bandgap. On the other hand, TWMZMs have the advantages of large electrical bandwidth, large optical bandwidth, and thermal stability.

Few 200 Gb/a and 400 Gb/s demonstrations based on the SiP platform have been reported in the literature. In [115] a 400 Gb/s transmitter using four TWMZMs is presented. However, the demonstration is based on the DMT modulation format and relatively complex DSP is needed at both the transmitter and the receiver. Moreover, each MZM is tested individually and crosstalk between MZMs was not reported which is expected to degrade the performance of the transmitter. Furthermore, an eight-lane hybrid multi-chip module comprising InP lasers, SiP MZMs, and parallel SMFs, all connected via photonic wire bonds and achieving 400 Gb/s aggregate bitrate has been presented [116]. However, the demonstration is in the C-band and each lane is tested individually using RF probes while crosstalk between the modulators is expected to degrade the performance when all lanes are operated simultaneously [117].

In this chapter, we present three PICs targeting 200 Gb/s and 400 Gb/s intra-data center interconnects operating in the O-band. First, we present an O-band four-lane 400 Gb/s transmitter using four parallel SiP TWMZMs in section 4.2. The transmitter is designed for intra-datacenter optical interconnects where it is fiber rich and PSM fibers are used. The measured average EO bandwidth for the MZMs is approximately 30 GHz at 3 V DC reverse bias voltage. To enable parallel operation, minimal crosstalk should exist between the modulators. The measured EO small-signal crosstalk between the closest MZMs is below -17 dB over 50 GHz bandwidth. The crosstalk decreases below -30 dB for 750 µm spacing and more. Then, we report the performance of the transmitter in a transmission test-bed versus several parameters. Results show that 53 Gbaud PAM4 per lane can be received at a BER below the KP4 forward error correction (KP4-FEC) threshold of 2.4×10^{-4} using only a 5-tap feed forward equalizer (FFE) at the receiver when the RF signals on the other lanes are disabled. Moreover, we show that 53 and 64 Gbaud PAM4 per lane can be received at a BER below the KP4-FEC and the 7% hard decision-FEC (HD-FEC) (3.8×10^{-3}) thresholds, respectively, using only 1.8 Vpp drive voltage swing and 11 tap-FFE. To the best of our knowledge, this is the best result for 100 Gb/s net rate per SiP TWMZM with a lateral PN junction in a multi-project wafer (MPW) run using only 1.8 Vpp and 11-tap FFE. In addition, we show the effect of crosstalk from the other channels on the tested channel, and conclude that a slight degradation occur in the BER when the crosstalk voltage swing is above 2 Vpp. However, the BER is still below the KP4-FEC at maximum crosstalk for all lanes, where 400 Gb/s aggregate net rate can be transmitted at an average BER of approximately 1×10^{-4}.

In section 4.3, we present an O-band SiP transmitter for 200 Gb/s applications over parallel SMF links. In this design, we focus on having a low cost transmitter with relatively low driving voltage swing and light DSP. To achieve that, we need to overcome the disadvantage of single electrode TWMZMs where a trade-off exists between the bandwidth and the efficiency [25, 26]. Multi-electrode MZMs (MEMZMs) have been proposed to overcome such disadvantage where the voltage swing is divided across the segments while the bandwidth of each segment is significantly high [118, 119]. Also, using binary signals to drive the MEMZM, high order modulation formats can be generated instead of using more complex signal generators [119–121]. In [122], 128 Gb/s PAM4 transmission is achieved using a C-band MEMZM driven by more than 3 Vpp on each segment and relatively aggressive DSP to operate below the KP4-FEC threshold. Our transmitter is based on a dual-parallel MEMZM (DP-MEMZM) configuration where the MEMZMs have average V_π of 5 V and EO bandwidth of 38 GHz. All segments are driven simultaneously using four independent binary streams to generate two PAM4 signals in the optical domain. More than 100 Gb/s net rate per lane can be received at a BER below the KP4-FEC threshold using only 3 equalizer taps at the receiver. Also, each MEMZM can be driven by only 2 Vpp and 1 Vpp on both segments up to 128 Gb/s bitrate in the absence of crosstalk from the other MEMZM. Driving both MEMZM simultaneously, results show that 200 Gb/s net rate can be received over up to 10 km of SMF using the SiP transmitter at a BER below the KP4-FEC threshold.

Finally, we present an O-band DP SiP transmitter based on TWMZMs in a SV-DD system targeting intra-datacenter applications in section 4.4. We report the DC characterization, small-signal modulation, and large-signal modulation of the SiP transmitter for both DP-PAM2 and DP-PAM4 versus number of taps, received signal power, SOP, reach, and bitrate. The modulator consists of two TWMZMs with average $V_{\pi}L$ and 3-dB bandwidth at 1.5 V DC bias voltage of 2.88 V.cm and 24.5 GHz, respectively. Results reveal that only 5 taps are required for a 168 Gb/s DP-PAM4 signal using the 6×2 multiple-input multiple-output (MIMO) equalization at the receiver to achieve a BER below the 7% HD-FEC threshold. Also, we can achieve 112 Gb/s DP-PAM2 over 10 km of SMF at a BER of 1.17×10^{-6} at the worst case SOP. In addition, 224 Gb/s and 200 Gb/s DP-PAM4 is successfully received at a BER below the HD-FEC threshold in the B2B and 2 km cases, respectively. Finally, we compare the performance of the 6×2 MIMO to a simpler 4×2 MIMO, and discuss the superior performance of the 6×2 MIMO in the presence of SVR imperfections.

4.2 A 400 Gb/s O-band silicon photonic transmitter for intra-datacenter optical interconnects

In this section, we present the design and characterization of a 400 Gb/s SiP transmitter operating in the O-band for intra-datacenter optical interconnects. First, the device details are explained in subsection 4.2.1. The small-signal characterization of the device is presented in subsection 4.2.2. In subsection 4.2.3, the experimental setup for the large-signal modulation is introduced and the experimental results are presented.

4.2.1 Design and fabrication

Figure 4.1(a) shows the layout schematic of the SiP transmitter. The continuous wave (CW) laser is coupled to the SiP chip using a grating coupler at the input, where it is then split by three low loss Y-branches to feed the four MZMs [77]. All the MZMs are identical and the travelling wave electrodes are terminated using on-chip 50 ohm terminations. The

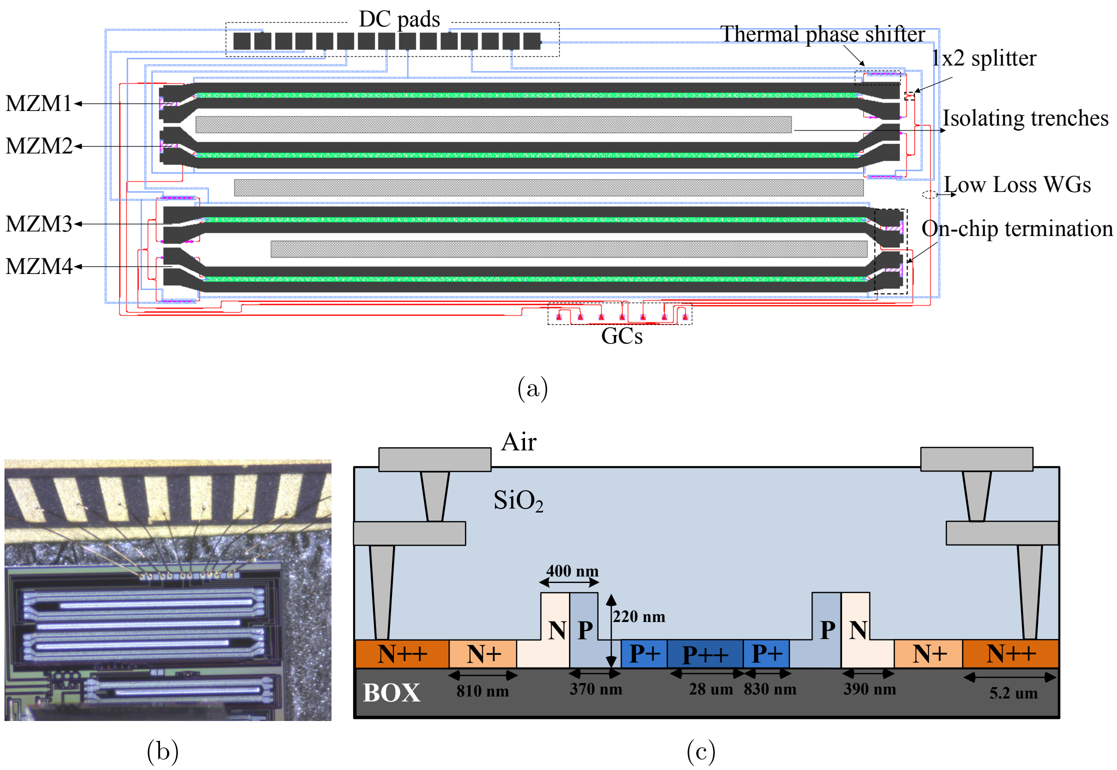

Figure 4.1. (a) Layout schematic for the SiP transmitter, (b) image of the die wirebonded to a chip carrier, and (c) TWMZM cross-section.

MZMs have approximately 360 μm spacing center-to-center. Also, 3 μm wide waveguides are used for routing to decrease the routing losses due to scattering from the waveguide sidewall roughness. The MZMs are balanced and a thermal phase shifter is added to one of the arms of each modulator to bias the modulators at the quadrature point. Moreover, isolating deep trenches are added between the MZMs to decrease the crosstalk between the modulators. The outputs of the four MZMs are connected to four grating couplers to enable parallel operation. The DC connections for the transmitter were wirebonded to a chip carrier as shown in Fig. 4.1(b).

The 400 Gb/s transmitter was fabricated in a MPW run at the advanced micro foundry (AMF) on a SOI wafer with a 220-nm-thick top silicon layer, a 2-μm-thick BOX layer, and a high-resistivity 750 Ω-cm silicon substrate using 193 nm lithography. The TWMZM cross-section is shown in Fig. 4.1(c), where the electrode design is similar to our previous TWMZM designs in [26,123]. Small modifications were made on the p-n junction geometry to enable O-band operation such as decreasing the waveguide width to 400 nm. All the modulators are 4.35 mm in length from pad center to pad center with a phase shifter length of ∼4 mm. Owing to the SPP configuration, the microwave losses decrease and the modulation bandwidth is improved compared to the conventional dual differential drive scheme. In addition, the transmitter's driver circuit is simplified due to the need of one driving RF signal per modulator.

4.2.2 DC and small-signal characterization

The fiber-to-fiber IL measured at maximum transmission was approximately 21.2 dB from the input to the output of one of the modulators. The ILs breakdown is as follows: ∼9 dB from the grating coupler pair, 6.6 dB from the splitters (splitting and excess losses), 4.1 dB modulator IL, and 1.5 dB routing losses. Using low loss edge couplers and more optimized routing will decrease the ILs by 6 - 8 dB [86, 124].

A 50 GHz Keysight lightwave component analyzer (LCA) and 50 GHz GSSG probes were used to perform the small-signal characterization for the four MZMs. Figure 4.2(a) shows the measured electrical-electrical (EE) S_{11} responses for the four MZMs. The S_{11} magnitude is well below -15 dB over 50 GHz. The EO S_{21} magnitude responses for DC bias voltages of 0 V and 3 V are shown in Figs. 4.2(b) and 4.2(c) where the four MZMs have very close results as expected. The 3-dB bandwidth is approximately 25 GHz at 0 V and increases to 30 GHz at 3 V reverse bias voltage.

Next, we characterize the crosstalk between the four MZMs in Fig. 4.2(d). The crosstalk between the transmission lines can be attributed to electric and magnetic radiative crosstalk and conductive substrate crosstalk. We added deep trenches between neighbor MZMs to reduce through-substrate conductive crosstalk, however, it helps to a small degree since most of the crosstalk is radiative between the electrode metallic lines. This conclusion is

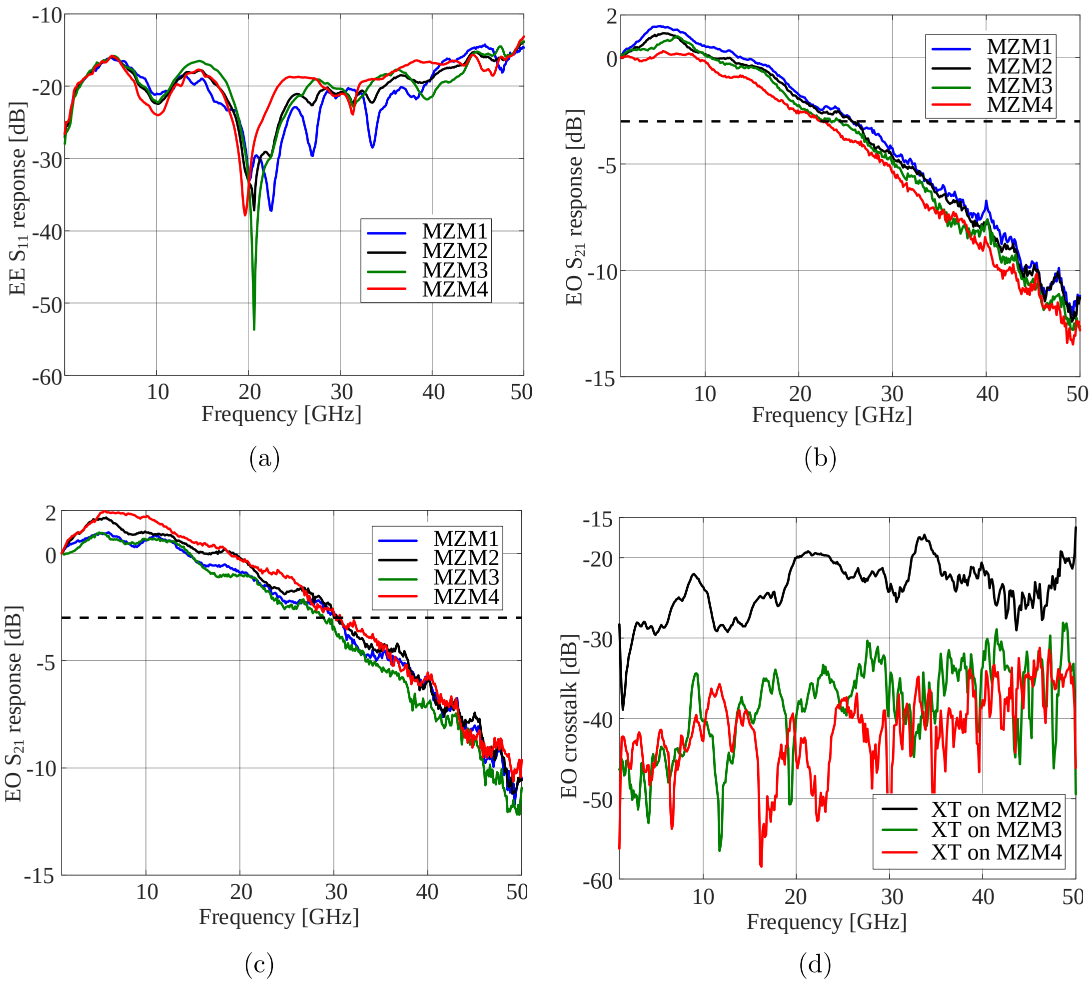

Figure 4.2. (a) EE S_{11} response for the four modulators, (b) and (c) EO S_{21} response for the MZMs at 0 V and 3 V DC bias, respectively, and (d) EO crosstalk between MZM1 (aggressor) and MZM2-4 (victims).

reached by comparing our result to the results in [117], where no trenches are added and nearly same separation of more than 600 μm is needed to have negligible crosstalk penalty. Hence, we conclude that the crosstalk is mainly due to radiation between neighbor MZMs. We find the EO crosstalk between MZM1 (aggressor), and the other MZMs (victims) using GSSG probes. On the other hand, SGGS probes, which were not available at the time of the experiment, are expected to have less crosstalk compared to the GSSG probes as shown in [125]. To measure the EO crosstalk, the RF signal from the LCA is launched into the input of MZM1 and the optical output of the victim MZM is connected to the optical port of the LCA. Then, the measured crosstalk is normalized to the victim's EO response and plotted in Fig. 4.2(d). It can be observed that the crosstalk between MZM1 and MZM2 is below -17 dB over the entire 50 GHz range, and increases with frequency. Hence, we expect that the crosstalk will have more impact on the performance at higher bitrates. Although the crosstalk value here is relatively low, we show in the next section that it is not negligible and the MZM spacing should be increased more than the used 360 µm to decrease the penalty when the MZMs are simultaneously modulated. In addition, the crosstalk between MZM1 and both MZM3 and MZM4 which are spaced by $\sim$ 750 µm and 1100 µm, respectively, is well below -30 dB and can be neglected. This agrees with the results in [117] where negligible penalty is achieved at 600 µm spacing between the SiP modulators.

4.2.3 Large-signal experimental setup and results

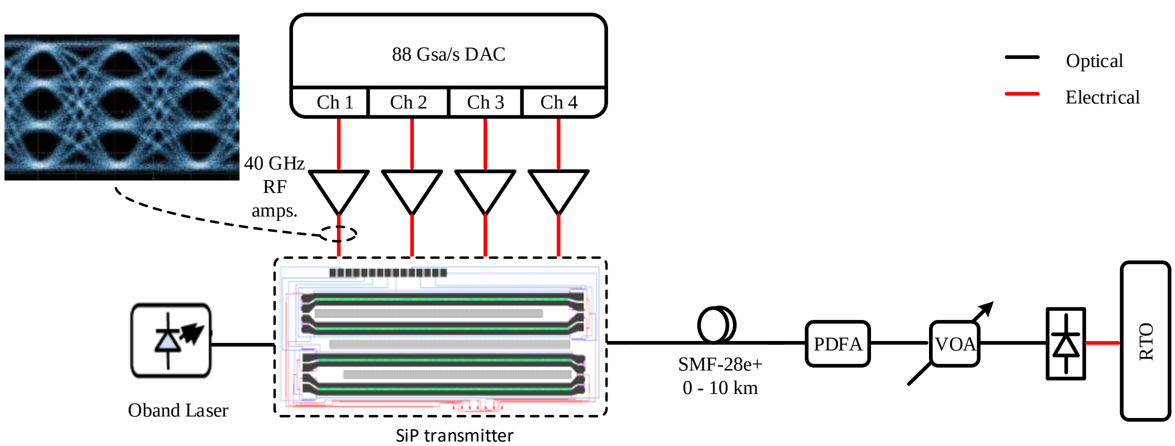

Figure 4.3. Experimental setup used for the 400G PSM transmitter testing. Inset: 53 Gbaud PAM4 RF signal out of the amplifier. DAC: digital-to-analog converter, PDFA: praseodymium-doped fiber amplifier, SMF: single mode fiber, VOA: variable optical attenuator, and RTO: real time oscilloscope.

Figure 4.3 shows the experimental setup used to characterize the 400 Gb/s transmitter. An O-band laser launches a 16 dBm CW light at 1310 nm wavelength to the SiP chip using the input grating coupler. An 8-bit DAC running at 88 GSa/s is used to generate four PAM4 signals. Then, the output RF signals from the four channels of the DAC are amplified using four 40 GHz RF amplifiers. A 53 Gbaud PAM4 eye diagram after the RF amplifier for one of the driving lanes is shown in the top-left inset of Fig. 4.3(a). At the transmitter side, we only pre-compensate the response of the DAC and RF amplifier. No pre-emphasis or non-linearity pre-compensation is used for the MZMs, and only simple level shifting for the inner levels of the PAM4 signal is done at some bitrate values. The driving signals are applied to the four modulators using 50 GHz GSSG probes. The modulated optical signal is then launched into various lengths of SMF (Corning SMF-28e+) covering reaches ranging from 500 m to 10 km. Also, a praseodymium-doped fiber amplifier (PDFA) is used to provide sufficient signal power to the 50 GHz PD which has no transimpedance amplifier stage. To sweep the received signal power, a VOA is added before the receiver. Finally, the signal out of the PD is sampled at 160 GSa/s by a 62 GHz real time oscilloscope (RTO) and stored for offline processing. The offline processing includes: resampling, FFE, symbol de-mapping, and bit error counting.

First, we measure the RF V_π using a 10 Gb/s on-off keying (OOK) driving signal. We launch the RF signal to the MZM, and monitor the optical eye diagram on the digital sampling scope (DSO). By sweeping the driving voltage swing, we find the RF V_π to be approximately 6 V. Hence, the measured bandwidth/ V_π is approximately 5 GHz/V. Next, we show the BER performance results for one of the MZMs and similar results were found for the other MZMs versus number of receiver equalizer taps, driving voltage swing, crosstalk swing voltage, bitrate, and reach. In Fig. 4.4(a), the BER performance versus the number of receiver equalizer taps is reported at different symbol rates of PAM4 modulation format in the absence of crosstalk from the other MZMs. To reiterate here, only the responses of the DAC and RF amplifiers are pre-compensated at the transmitter and the rest of the chain including the modulator and PD is left at the receiver side where a FFE is used and the taps are found adaptively using the least mean squares (LMS) algorithm. For the 53

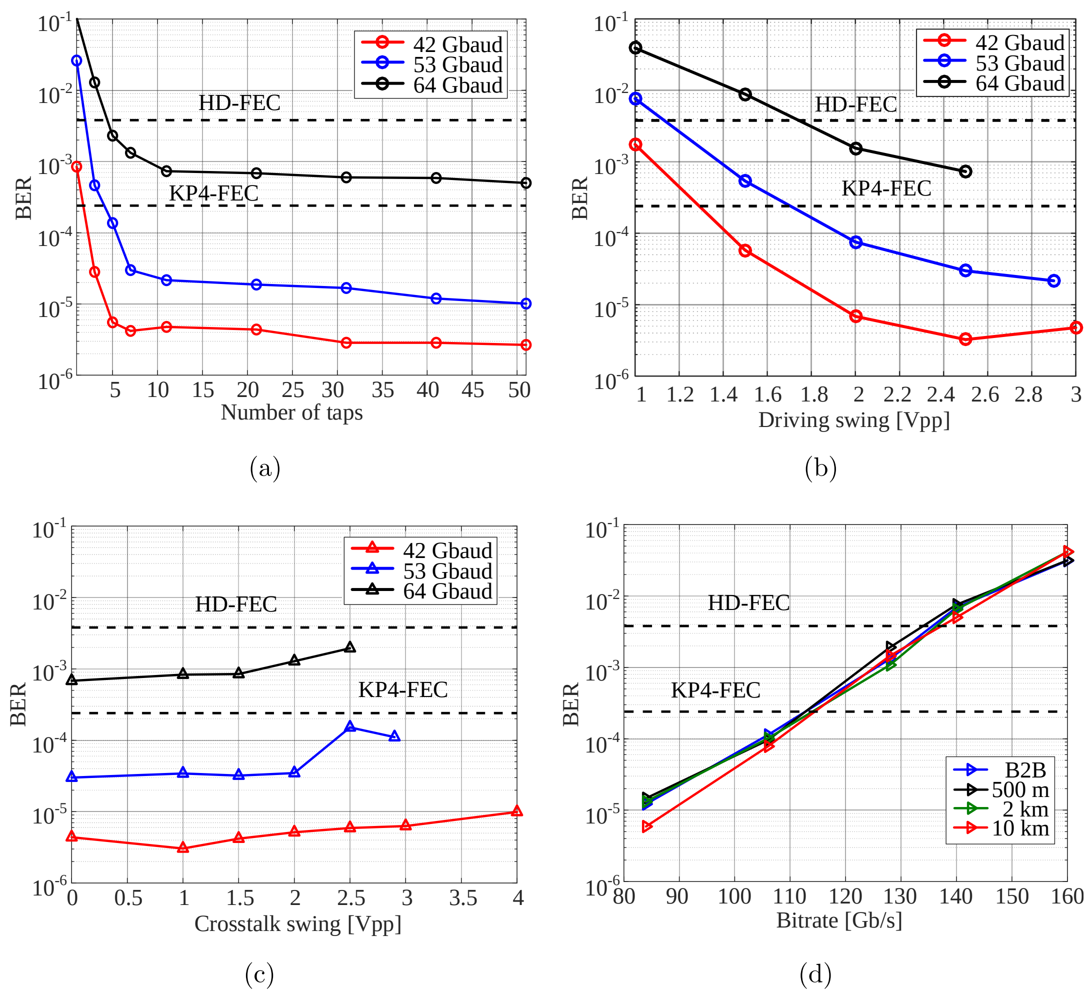

Figure 4.4. (a) BER performance versus number of receiver FFE taps for different symbol rates, (b) BER performance versus driving voltage swing without crosstalk, (c) crosstalk impact on BER performance at different symbol rates, and (d) BER performance versus bitrate for a single lane in presence of crosstalk over different reach values at constant received signal power.

Gbaud PAM4, only a 5-tap FFE at the receiver is needed to achieve a BER below the KP4-FEC threshold of 2.4×10^{-4}. Increasing the number of taps further to 41 taps improves the BER performance to reach $\sim 1 \times 10^{-5}$ at the expense of increasing the complexity. The optimal number of taps is found to be approximately 11 taps, where further increases have a small improvement in the BER. Also, we can observe a similar trend for the 42 Gbaud and 64 Gbaud symbol rates. However, we observed that a BER below the HD-FEC can only be achieved for the 64 Gbaud curve, this can be attributed to the limited driving swing, as will be discussed next, as well as the increased inter-symbol interference (ISI) and increased noise. For the rest of the results, we fix the number of taps at 11 taps.

In Fig. 4.4(b), we study the BER performance versus the driving voltage swing at different symbol rates for the PAM4 modulation format in the absence of crosstalk from the other MZMs. Less than 1.8 Vpp is needed to achieve a BER below the KP4-FEC threshold at 100 Gb/s net rate. To the best of our knowledge, this is the first time 100 Gb/s net rate is achieved using a MZM in a MPW process driven by less than 1.8 Vpp driving swing and few taps at the receiver side. Increasing the driving swing further improves the BER performance to reach approximately 2×10^{-5} at 2.9 Vpp voltage swing. Similarly, less than 1.8 Vpp is needed to achieve a BER below the HD-FEC for the 64 Gbaud case. The maximum voltage swing at 64 Gbaud is 2.5 Vpp which is the maximum achievable voltage from the RF amplifier at such symbol rate. Increasing the driving swing above 3 Vpp together with more FFE taps, we expect to reach a BER below the KP4-FEC for the 64 Gbaud symbol rate. For the rest of the results, the driving voltage swing of the lane under test is fixed at the maximum achievable voltage.

Then, we enable the RF signal on all MZMs, and study the effect of the crosstalk voltage swing of the three lanes on the lane under test in Fig. 4.4(c). We set the driving voltage swing of the lane under test to the maximum achievable swing out of the RF amplifier. At 53 Gbaud, it can be observed that driving all lanes simultaneously has a negligible effect on the BER up to a crosstalk voltage swing of 2 Vpp. The BER performance deteriorates when the crosstalk driving swing is increased to 2.5 Vpp. However, the BER is below the KP4-FEC at all crosstalk values. From that we conclude that the current 350 µm modulators spacing is not sufficient to completely mitigate the effects of crosstalk. Figure 4.4(d) presents the BER performance versus bitrate over different reach values at 7 dBm received signal power for a single MZM while all MZMs are simultaneously modulated. In this figure, the number of taps is fixed at 11 taps to decrease the system complexity and the swing is the maximum available swing after the RF amplifier. For example, at 53 Gbaud the voltage swing is 2.9 Vpp, and reaches below 1.2 Vpp for the 80 Gbaud signal. As expected, the system is loss-limited, and hence the BER is nearly constant with reaches up to 10 km of SMF at equal received signal power. The BER for 100 Gb/s signal is approximately 1×10^{-4} after 10 km propagation. The BER degrades with further increases in the bitrate to reach 4×10^{-3} at 140 Gb/s due to both the ISI and the limited voltage swing. Hence, increasing the voltage swing and using a stronger equalizer, we expect to operate below the FEC threshold.

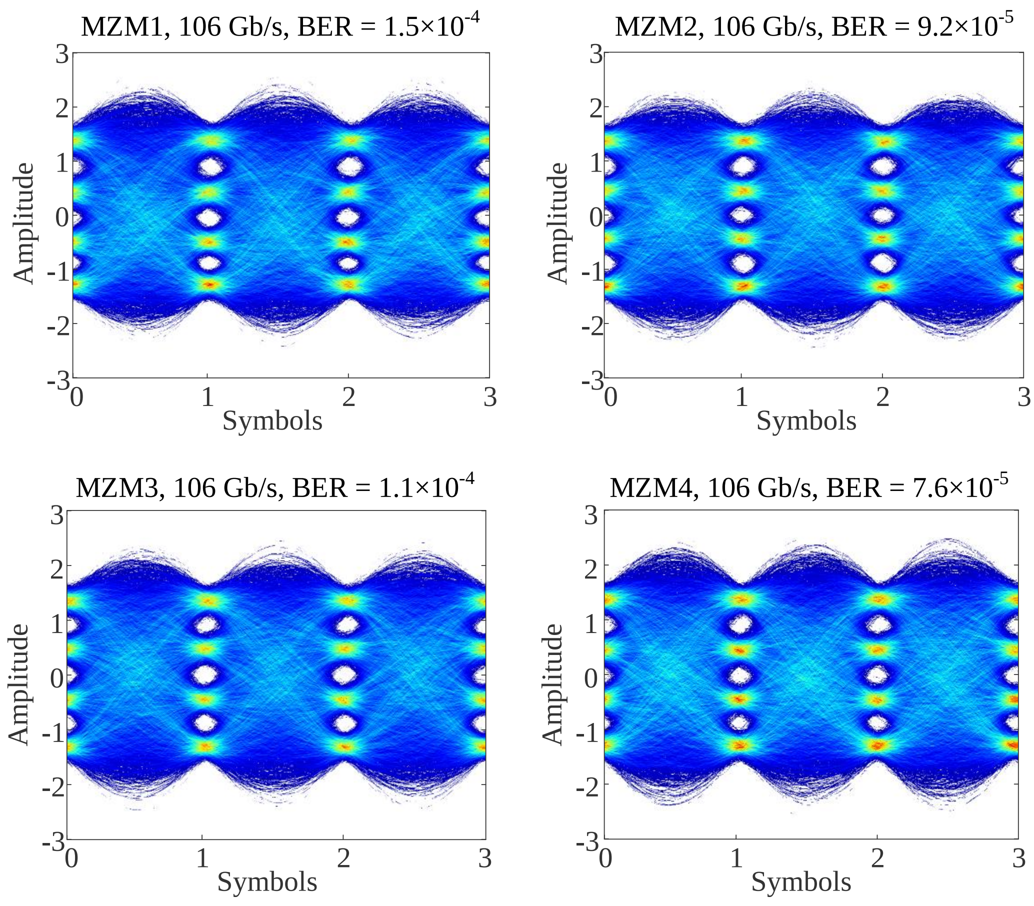

Figure 4.5. Eye diagrams for the four MZMs simultaneously modulated obtained after receiver DSP at 100 Gb/s net rate.

Next, we characterize the performance of the four lanes of the 400 Gb/s transmitter.

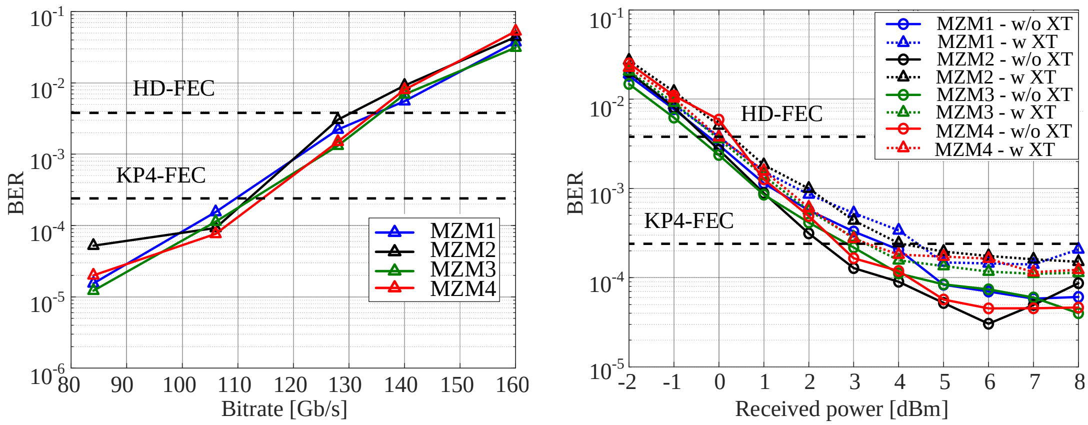

(a) (b)

Figure 4.6. (a) BER versus bitrate for the four MZMs simultaneously modulated in the B2B case, and (b) BER versus received signal power with and without presence of crosstalk from other lanes.

Figure 4.5 presents eye diagrams for the four MZMs of the transmitter driven by 53 Gbaud PAM4 signal after receiver DSP. The eye diagrams show clear open eyes from all lanes at the receiver side at 100 Gb/s net rate per lane while all lanes are simultaneously modulated. The BER performance for all MZMs versus bitrate in the B2B case at 7 dBm received signal power is shown in Fig. 4.6(a). It can be observed that all MZMs have a close performance as expected. Also, we can achieve 106 Gb/s per lane, i.e., 400 Gb/s aggregate net rate, below the KP4-FEC threshold using 2.9 Vpp drive voltage and 11 tap-FFE. To the best of our knowledge, this presents the first demonstration of 400 Gb/s in the O-band using simultaneously modulated SiP based MZMs driven by below 3 Vpp and simple DSP targeting intra-datacenter optical interconnects. The estimated power consumption to achieve 100 Gb/s net rate per lane at a BER below the KP4-FEC threshold is 9 mW and 23.36 mW with and without crosstalk from other lanes, respectively, excluding the power consumption from the thermal phase shifters for the biasing. The energy per bit for the four lanes for an aggregate rate of 400 Gb/s is 0.9344 pJ/bit. Moreover, if more spacing between the MZMs is added, the MZMs can be driven with lower voltage and crosstalk penalty can be neglected yielding energy per bit for the four lanes of only 0.36 pJ/bit.

Figure 4.6 (b) shows the received signal power of all lanes with and without crosstalk running at 53 Gbaud PAM4. It can be observed that approximately an average of 3 dBm and 4 dBm received signal power is needed to achieve a BER below the KP4-FEC threshold with and without crosstalk, respectively. Hence, ∼1 dB penalty occurs due to simultaneous modulation at high received signal powers, whereas the penalty is negligible at lower received power values since the performance is dominated by other noise sources such as receiver noise.

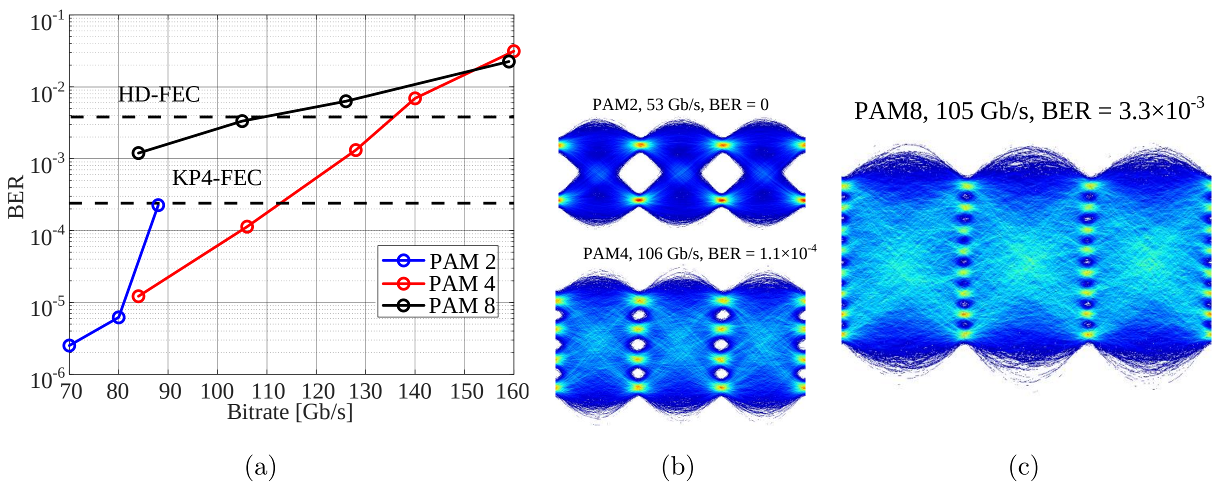

Figure 4.7. (a) BER versus bitrate for different modulation formats in the B2B case, and (b-c) eye diagrams after receiver DSP for PAM2, PAM4 and PAM8 modulation formats running at 53, 53, and 35 Gbaud, respectively.

Finally, we compare the BER performance versus bitrate for PAM2, PAM4, and PAM8 modulation formats for one lane while other lanes are enabled as shown in Fig. 4.7(a). To reiterate here, the modulator transfer function is not pre-compensated at the transmitter side. The number of receiver FFE taps is fixed at 11, 11, and 31 taps for PAM2, PAM4, and PAM8, respectively. The number of taps is increased for PAM8 modulation format since the eyes are more closed due to smaller separation and we don't apply non-linear compensation at the transmitter side and stronger DSP is needed. Eye diagrams after receiver DSP for 53, 106, and 105 Gb/s signals using PAM2, PAM4 and PAM8 modulation formats, respectively, are shown in Figs. 4.7(b) and 4.7(c). For the PAM2 signal, a bitrate up to 88 Gb/s can be received at a BER below the KP4-FEC threshold. It is interesting to notice that to achieve 100 Gb/s per lane while still having low complexity, we need to switch to PAM4 modulation format instead of PAM2. However, a higher BER is achieved and a relatively strong FEC is needed to switch from PAM2 to PAM4 modulation format. Finally, we expect for higher target bitrates another transition to PAM8 modulation format that operate at lower symbol rate at the expense of utilizing a stronger FEC and equalization.

4.3 Dual Parallel Multi-electrode Traveling Wave Mach-Zehnder Modulator for 200 Gb/s Intra-datacenter Optical Interconnects

In this section, we present the design and characterization of a ≥200 Gb/s SiP transmitter based on MEMZMs operating in the O-band for intra-datacenter optical interconnects. First, the design and fabrication are explained in subsection 4.3.1. Then, the small-signal characterization of the transmitter is presented in subsection 4.3.2. In subsection 4.3.3, the experimental setup for the large-signal modulation is introduced. The large-signal experimental results are presented in subsection 4.3.4.

4.3.1 Design and fabrication

The transmitter was fabricated in a MPW run in the same process of the design reported in section 4.2. Figure 4.8(a) shows the layout schematic of the SiP transmitter. The transmitter consists of two parallel MEMZMs based on a SPP configuration. The crosssection of the modulator is similar to the design shown in Fig. 4.1(b).

The transmitter operation can be explained as follows. The CW light is coupled to the SiP chip using a focusing grating coupler at the input, where it is then split by a low loss Y-branch to feed the two MEMZMs. We choose all the electrode segments to be equal length of 3 mm, and by using driving voltage swings of Vpp and Vpp/2 on the segments, a PAM4

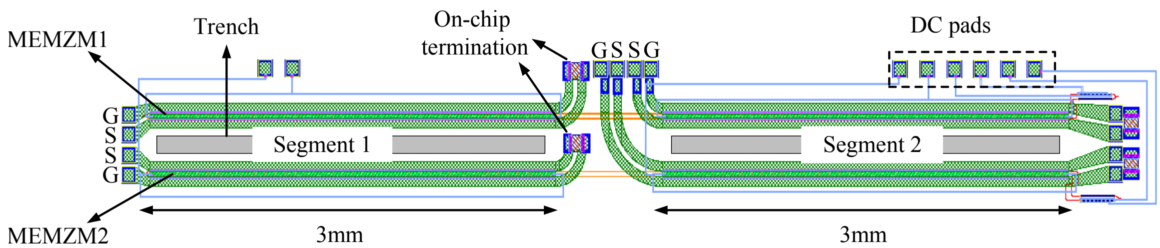

(a)

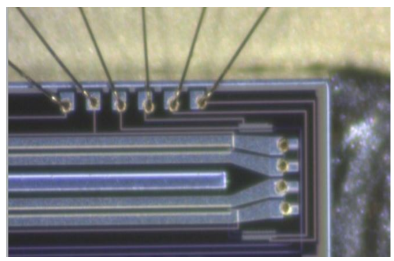

(b)

Figure 4.8. (a) Layout schematic for the SiP transmitter, and (b) image of the DC wirebonds and ball bumps on the 50-ohm terminations.

optical signal can be generated. All segments are terminated using doped silicon based on-chip 50 ohm terminations which are connected to the MEMZM's pads using ball bumping as shown in Fig. 4.8(b). The MEMZMs are spaced by 360 µm center-to-center, and a trench with 120 µm depth to the silicon substrate is added between the parallel segments to decrease the crosstalk between both MEMZMs. Both MEMZMs are balanced and a N-doped resistive heater is added to one of the arms to bias the MEMZMs at the operating quadrature point. The outputs of both modulators are connected to two grating couplers to enable parallel operation. The die was wirebonded to a chip carrier and mounted on a printed circuit board (PCB) for the DC connections.

4.3.2 DC and small-signal characterization

The fiber-to-fiber IL measured at maximum transmission was approximately 19.5 dB from the input to the output of one of the modulators. This can be attributed to ~9 dB from the grating coupler pair, 3.3 dB from the Y-branch, 6 dB modulator IL, and 1.2 dB routing losses. The major contribution in the IL is due to the grating couplers which are used in this design to enable more dense integration in the MPW. Hence, the IL can be optimized by more than 8 dB using low loss edge couplers and more optimized routing [86, 124].

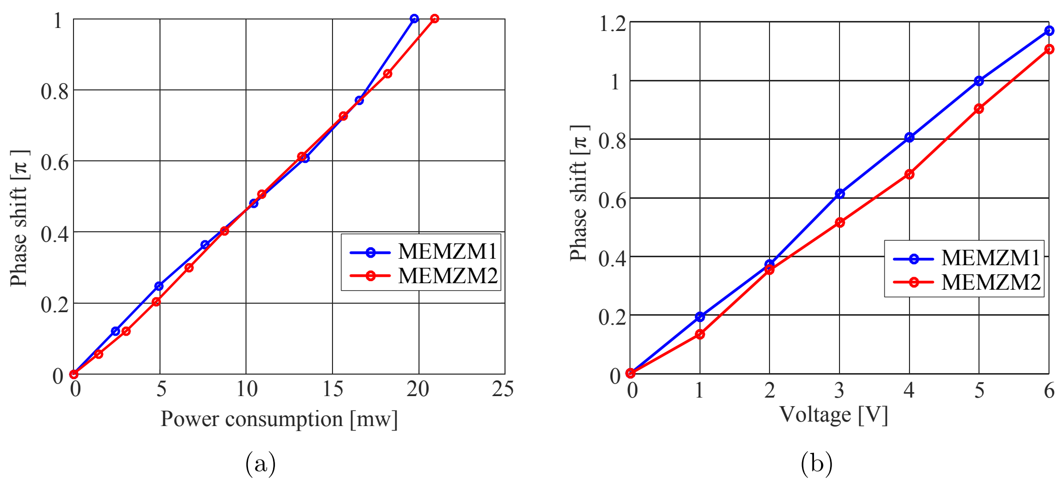

Figure 4.9. (a) Extracted phase shift versus power consumption for the thermo-optic phase shifter and (b) extracted phase shift versus DC voltage for the MEMZM's pn junction.

First, we characterize the thermo-optic phase shifters in terms of power consumption as shown in Fig. 4.9(a). The heaters consume approximately 20 mW for a π phase shift. Although the MEMZMs are balanced, a large FSR due to fabrication imperfections occurs and the output power is not generally at maximum transmission. Hence, the heaters are adjusted by monitoring the output power of each MEMZM. Also, we measure the PN junction phase shift versus the applied voltage to determine the MEMZM's V_π. The phase shift for each diode is measured, and then the average of both diodes is calculated. The extracted phase shift versus voltage is shown in Fig. 4.9(b), where a more linear behavior is observed due to the long length of the phase shifter. The V_π is measured to be 5 V and 5.5 V for MEMZM1 and MEMZM2, respectively. The calculated average $V_\pi L$ of both MEMZMs is 2.7 V.cm.

For small-signal characterization, a 50 GHz Keysight LCA and 50 GHz GSSG probes

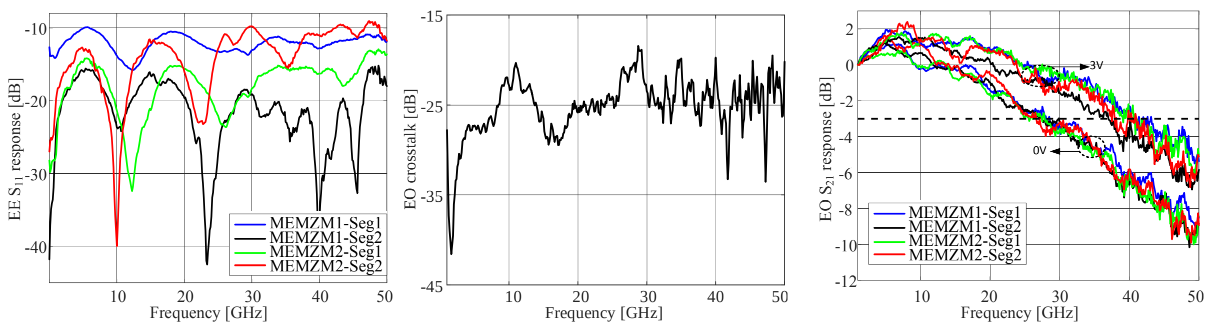

Figure 4.10. (a) Electrical S_{11} response for the fours segments, (b) EO crosstalk between both MEMZMs, and (c) EO S_{21} response for both MEMZMs at 0 V and 3 V DC bias voltages.

were used to characterize both MEMZMs. Figure 4.10(a) shows the measured EE S_{11} responses for the four segments. Then, we measure the EO crosstalk between both modulators where the effect of driving one segment of MEMZM1 on both segments of MEMZM2 is shown in Fig. 4.10(b). We show the effect of a single segment only because a four-port vector network analyzer was not available at the time of the experiment to drive both segments of MEMZM1. However, the large-signal crosstalk is fully characterized in the next section while all segments are simultaneously modulated. The RF signal is launched on segment 1 of MEMZM1 as the aggressor, and the optical output of MEMZM2 is connected to the other port of the LCA as the victim signal. Then, the measured signal is normalized to the victim EO bandwidth to get the crosstalk. The measured crosstalk is shown in Fig. 4.10(b), where the crosstalk is below 19 dB over 50 GHz range. This value is not negligible as will be shown from the large-signal modulation results, and more spacing between the two parallel MEMZMs is needed in future transmitter designs. The EO S_{21} magnitude responses for DC bias voltages of 0 V and 3 V are shown in Fig. 4.10(c) where the four segments have very close results as expected. The 3-dB bandwidth is approximately 28 GHz at 0 V and increases to 38 GHz at 3 V reverse bias voltage. The bandwidth/V_π figure of merit is 5.6 GHz/V and 5.1 GHz/V at 0 V DC bias voltage for MEMZM1 and MEMZM2, respectively.

4.3.3 Large-signal experimental setup

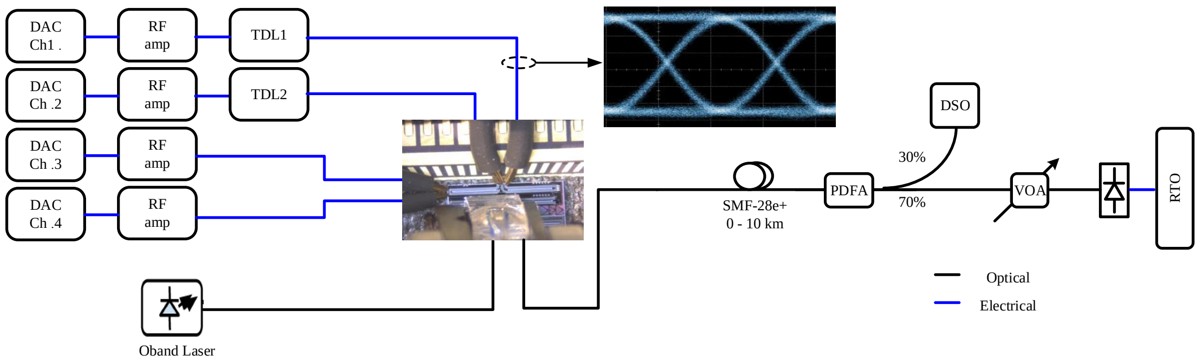

Figure 4.11. Experimental setup used to test the SiP modulator. Inset: 53 Gbaud binary signal out of the RF amplifier. DAC: digital to analog converter, RF amp: RF amplifier, TDL: tunable delay line, PDFA: praseodymium-doped fiber amplifier, DSO: digital sampling oscilloscope, VOA: variable optical attenuator, RTO: real time oscilloscope.

Figure 4.11 shows the experimental test-bed used to characterize the 200 Gb/s transmitter. An image of the transmitter under the probing station is shown in Fig. 4.11 where the RF signals are applied from the west and north. A fiber array unit is used for the input laser, output signals, and alignment gratings from the south. Also, the DC signals are applied using DC cables to the PCB. A 16 dBm CW laser at 1310 nm wavelength is launched to the SiP chip using the input grating coupler. At the transmitter side, we use a four channel DAC to generate four binary streams to drive the MEMZM, due to the unavailability of a four independent streams from a bit pattern generator. Then, the output RF signals from the four channels of the DAC are amplified using four 40 GHz RF amplifiers. Since, the target is to have a simplified transmitter, we only compensate the limited bandwidth of the DAC and RF amplifier. No pre-emphasis or non-linearity pre-compensation is used for the SiP MEMZMs. The driving 53 Gbaud binary signal from one of the channels is shown as an inset in Fig. 4.11. Also, tunable delay lines (TDLs) are used to adjust the delay between the driving signals for the segments of each modulator. The delay is adjusted by monitoring the eye diagram on the DSO. The driving signals are applied to the four segments using two 50 GHz GSSG probes. The modulated optical signal is then launched into various lengths of SMF (Corning SMF-28e+) covering reaches ranging from 500 m to 10 km. The modulated signal is received by a 50 GHz PD that has no following gain stage, and a PDFA is used to provide sufficient signal power to the PD. Finally, the signal is sampled at 160 GSa/s by a 62 GHz RTO and stored for offline processing. The offline processing includes: resampling, FFE, symbol de-mapping, and bit error counting. The receiver side FFE is used to compensate for the ISI resulting due to limited bandwidth of the MEMZM and the PD.

4.3.4 Large-signal experimental results

Next, we present the large-signal modulation results for the SiP transmitter. The BER performance is presented versus number of receiver equalizer taps, received signal power, driving voltage swing, crosstalk voltage swing, bitrate, and reach. Figure 4.12(a) shows the BER performance of the received PAM4 signal from MEMZM2 versus the number of receiver FFE taps at different symbol rates. Using only a 3-tap FFE, 53 Gbaud PAM4 per lane can be received below the KP4-FEC threshold of 2.4×10^{-4} while driven by only 2.8 Vpp and 1.4 Vpp on segment 1 and segment 2, respectively. Increasing the number of taps to 11 taps improves the BER to 1.1×10^{-5}. Similarly, 11 taps are required for the 64 Gbaud signal to operate below the KP4-FEC threshold. This is attributed to the increased symbol rate and the reduced voltage swing out of the RF amplifier at 64 Gbaud, where the driving swing is 2 Vpp and 1 Vpp for the MEMZM's segments. For the rest of the results, the number of FFE taps is fixed at 11 taps. Figure 4.12(b) presents the BER performance for both MEMZMs versus received signal power running at 53 Gbaud PAM4 where each MEMZM is tested individually and the RF signals on the other MEMZM is disabled. As expected, both MEMZMs have a very close performance and less than 3 dBm received signal power is required to achieve a BER below the KP4-FEC threshold. To reiterate here, the PD used in the experiment is not followed by a TIA, which when added will significantly improve the receiver sensitivity.

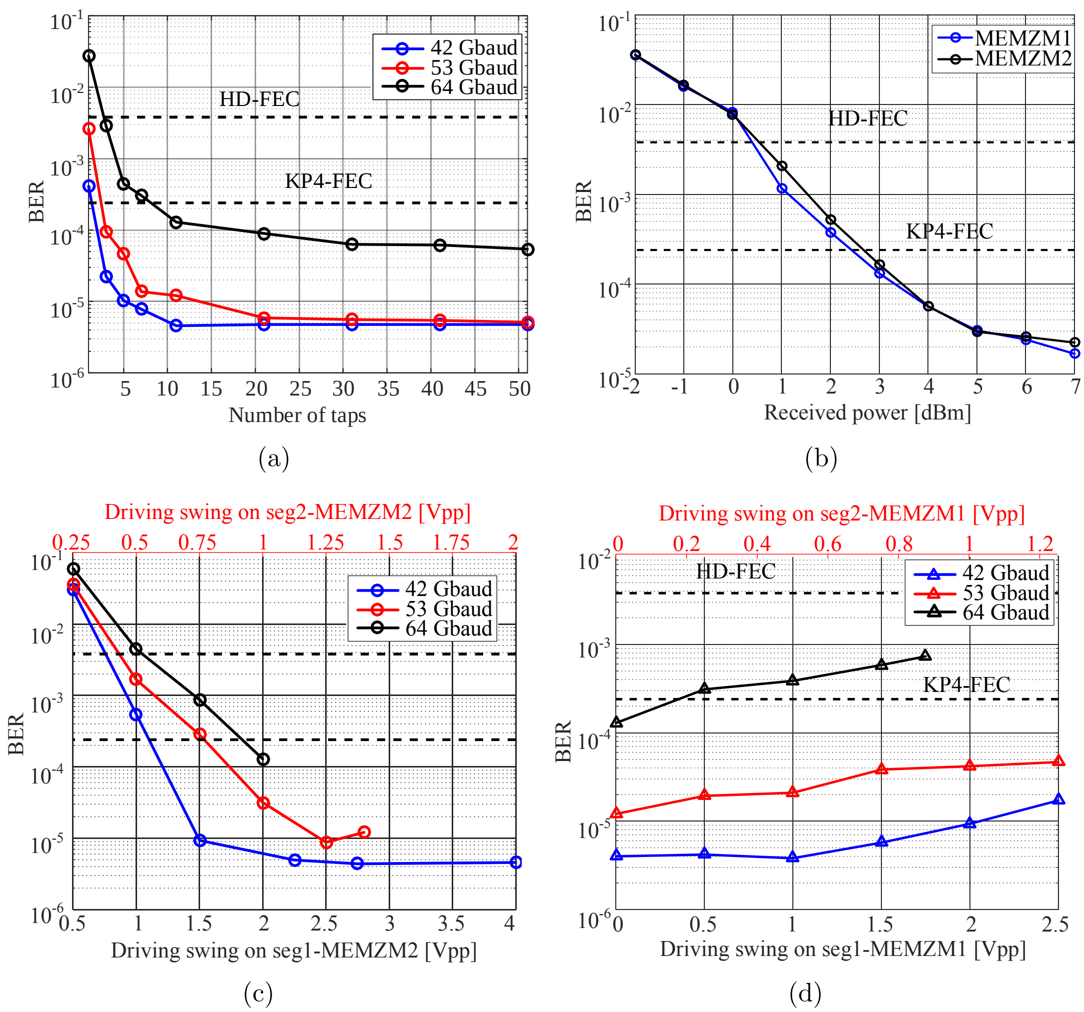

Figure 4.12. BER performance versus (a) number of receiver FFE taps for MEMZM2, (b) received signal powers for both MEMZMs, (c) driving voltage swing on both segments of MEMZM2, and (d) MEMZM1 crosstalk voltage swing on MEMZM2.

The BER performance for the PAM4 signal versus the driving voltage swing of both segments of MEMZM2 at different symbol rates, while the RF signals on MEMZM1 is disabled, is shown in Fig. 4.12(c). We sweep the drive voltage swing from 0.5 Vpp on segment 1 up to the maximum achievable swing out of the RF amplifier at each symbol rate. It can be observed that only 2 Vpp and 1 Vpp driving voltage swings on segment 1 and segment 2, respectively, are required to achieve a BER below the KP4-FEC threshold at symbol rates up to 64 Gbaud. Increasing the swing further enhances the BER performance where it reaches a BER of $\sim 1 \times 10^{-5}$ at 2.5 Vpp and 1.25 Vpp on the MEMZM's segments at 53 Gbaud. For the 42 Gbaud case, we observe an error floor above 2.5 Vpp driving swing due to the non-linearity of the SiP modulator which is not compensated to simplify the transmitter driver.

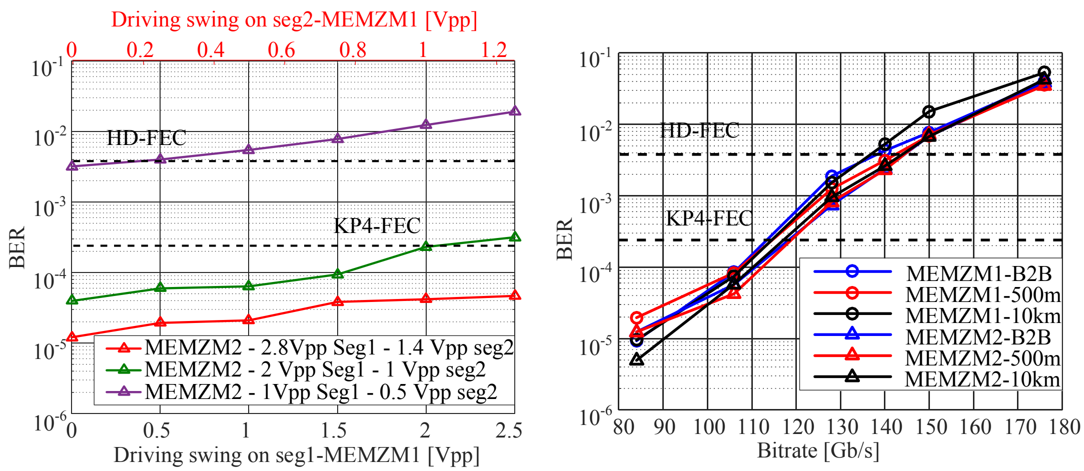

(a) (b)

Figure 4.13. BER performance versus (a) MEMZM1 crosstalk voltage swing at different driving voltage swing for MEMZM2, and (b) bitrate over different reaches at constant received signal power where both MEMZMs are simultaneously operated.

Then, we drive both MEMZMs simultaneously and assess the crosstalk penalty where the BER performance versus the crosstalk voltage swing is shown in Fig. 4.12(d). Here, we fix the swing on MEMZM2 at the maximum achievable swing at each symbol rate and sweep the driving swing voltage on MEMZM1 as crosstalk. The BER for the 53 Gbaud case increases from 1.1×10^{-5} at no crosstalk to 4.5×10^{-5} at maximum crosstalk, which signals that the spacing of 360 μm between the MEMZMs is not sufficient to completely mitigate the crosstalk effects. However, the BER per lane is well-below KP4-FEC threshold at maximum crosstalk at the target symbol rate of 53 Gbaud PAM4. In addition, we use GSSG probes in the experiment which represents the worst case scenario, while using SGGS probes was reported to have less crosstalk penalty [125]. Moreover, the BER performance degrades in the 64 Gbaud case where the BER increases to 9×10^{-4} at maximum crosstalk. Also, we present the crosstalk effect at different driving voltage swing for the modulator under test where we show three different driving voltage swings for MEMZM2 versus MEMZM1 crosstalk voltage swing in Fig. 4.13(a). It can be observed that more than 200 Gb/s aggregate rate can be achieved at a BER below the KP4-FEC threshold while both MEMZMs are simultaneously modulated using 2 Vpp and 1 Vpp drive voltage swings on the MEMZMs' segments. Finally, we present the BER performance versus bitrate per lane when both MEMZMs are driven simultaneously at same received signal power for the back-to-back, 500 m, and 10 km reaches as shown in Fig. 4.13(b). Results reveal that 200 Gb/s net rate over more than 500 m reach, typical distance for parallel SMF links for intra-datacenter optical interconnects, can be achieved at a BER below the KP4-FEC threshold.

4.4 200 Gb/s DP-PAM transmitter with SV-DD

To cope with the relentless increases in datacenter traffic. DP-IM along with a DD receiver have been proposed [12]. Using the polarization dimension, while using a DD receiver, offers a better scalable solution compared to single polarization PSM or WDM due to the reduction in the number of lasers required to achieve the same aggregate bitrate if the polarization dimension is exploited. In this section, we demonstrate a DP transmitter in a SV-DD experiment for short reach interconnects. In subsection 4.4.1, the design details and fabrication are presented. Then, the DC and small-signal characterization of the transmitter are presented in subsection 4.4.2. The experimental setup is introduced in subsection 4.4.3. The large-signal experimental results are presented in subsection 4.4.4.

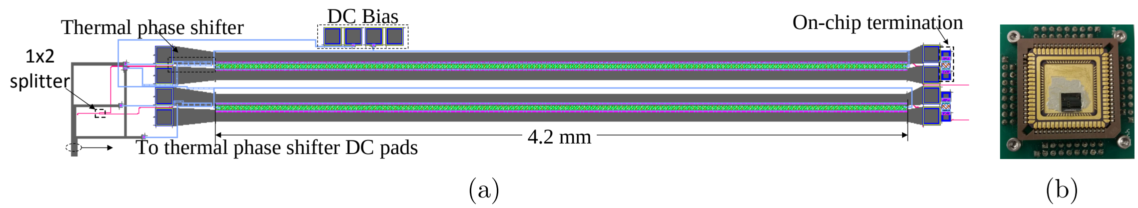

Figure 4.14. (a) Layout schematic for the SiP transmitter, and (b) micrograph of the die wirebonded to a chip carrier mounted on a PCB board.

4.4.1 Device design

The transmitter was fabricated using the same process as the previous designs except using 248 µm lithography. Figure 4.14(a) shows the layout of the SiP transmitter. A grating coupler couples the CW laser to the SiP chip , where it is then split by a 1 $\times$ 2 splitter. Each branch is connected to one of the TWMZMs. An intentional path imbalance between the modulator arms is added to allow for phase shift measurements. The outputs of both modulators were not combined on chip due to the use of booster optical amplifiers (BOAs) which amplify only one state of polarization and hence, polarization combining had to be performed off-chip after optical amplification of each polarization separately. The die was wirebonded to a chip carrier and mounted on a PCB for the DC connections (i.e., control signals of thermal phase shifters and bias of the pn junctions) as shown in Fig. 4.14(b).

4.4.2 DC characterization, and small-signal characterization

The measured transmission spectra for both arms of each modulator at different reverse bias voltages and the extracted phase shift are shown in Fig. 4.15. At maximum transmission, the fiber-to-fiber IL is measured to be $\sim$24.5 dB from the input to the output of one of the two modulators. The IL breakdown is as follows: $\sim$10 dB from grating couplers, 3.3 dB from Y-branch (splitting and excess losses), $\sim$7 dB routing losses, and 4.2 dB from the modulator. The phase shift versus voltage is extracted from the transmission spectrum for each arm (diode) of both modulators and shown in Figs. 4.15(c) and 4.15(f). A different

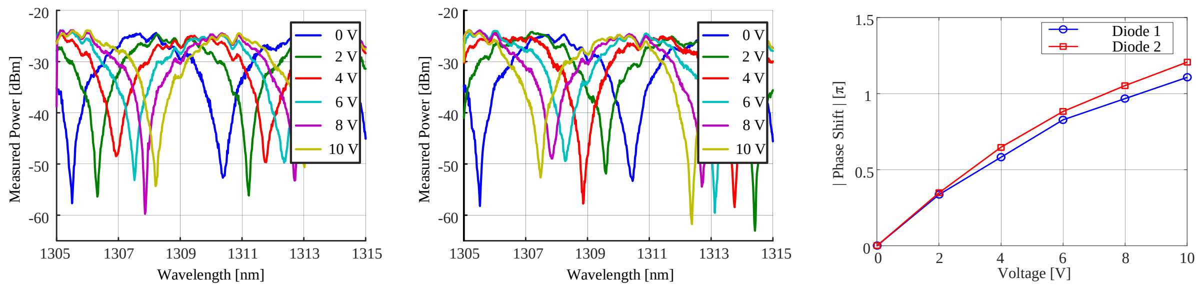

(a) Diode 1 (b) Diode 2 (c) Calculated Phase shift

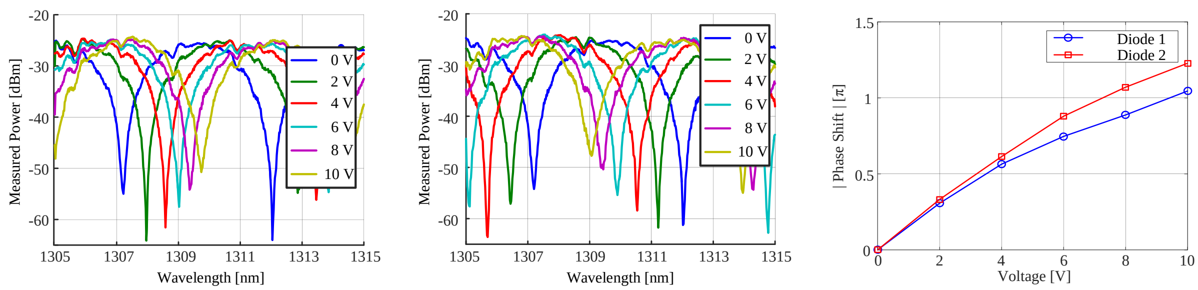

(d) Diode 1 (e) Diode 2 (f) Calculated Phase shift

Figure 4.15. (a) and (b) Transmission spectra for upper modulator diodes, (c) phase shift versus bias voltage for upper modulator diodes, (d) and (e) transmission spectra for lower modulator diodes, and (f) phase shift versus bias voltage for lower modulator diodes

phase shift is obtained from the two diodes of each modulator under the same applied voltage. This can be attributed to dopant masks misalignment during fabrication [25]. The V_π is approximately 8.25 V and 7.5 V for diodes 1 and 2 for the upper modulator, respectively. Also, the V_π is approximately 9.25 V and 7.1 V for diodes 1 and 2 for the lower modulator, respectively. This indicates an average $V_\pi L$ value of 2.83 V.cm and 2.94 V.cm for the upper and lower modulator, respectively.

A 50 GHz Keysight LCA and 50 GHz GSSG probes were used to perform the small-signal characterization for both modulators. Figures 4.16(a) and 4.16(b) show the EO S_{21} magnitude response normalized to the response at 1.5 GHz reference frequency for bias voltages of 0 V and 1.5 V. We choose only a 1.5 V bias voltage beside 0 V to do the small-signal characterization as it is the optimum DC bias that achieved the lowest BER. The 3-dB bandwidth is approximately 17 GHz at 0 V and increases to 25.5 GHz at 1.5 V

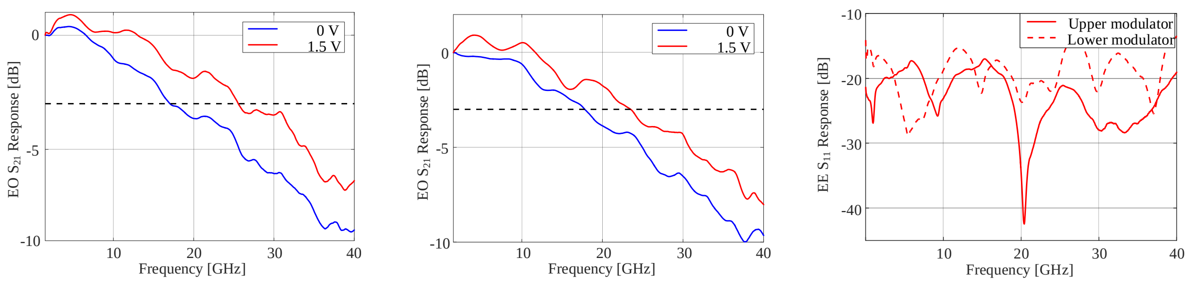

(a) (b) (c)

Figure 4.16. (a) EO S_{21} for the upper modulator, (b) EO S_{21} for the lower modulator, and (c) EE S_{11} for both modulators at 1.5 V.

reverse bias voltage for the upper modulator. Also, the 3-dB bandwidth is approximately 17.5 GHz at 0 V and increases to 23.5 GHz at 1.5 V reverse bias voltage for the lower modulator. Impedance mismatch cause the slight peaking observed in the response at 1.5 V. The measured EE S_{11} responses for both modulators are shown in Fig. 4.16(c). The S_{11} magnitude is well below -10 dB over 40 GHz for both modulators.

4.4.3 Experimental setup

Figure 4.17 introduces the experimental setup. First, transmitter DSP is applied where it includes symbol generation, raised cosine (RC) pulse shaping, a pre-emphasis filter, clipping, and quantization. The pre-emphasis filter is a finite impulse response (FIR) filter found adaptively using the LMS algorithm after the RF amplifier, and applied at 1 samples per symbol (SPS) on the generated symbols. The number of taps for the pre-emphasis filter is fixed at 75, however 99% of the filter energy is concentrated in only 21 taps. After the transmitter DSP is applied offline, the symbols are loaded into an 8-bit DAC running at 84 GSa/s. Two matched RF TDLs are used before the amplifiers to eliminate the RF skew between both channels including the modulators' skew. Then, the output RF signals are amplified using two 50 GHz RF amplifiers before being applied to the SiP transmitter using a 50 GHz GSSG probe. The driving voltage swing out of the amplifier is dependent on the baud rate, and the roll-off factor used. For example, the peak-to-peak amplitudes

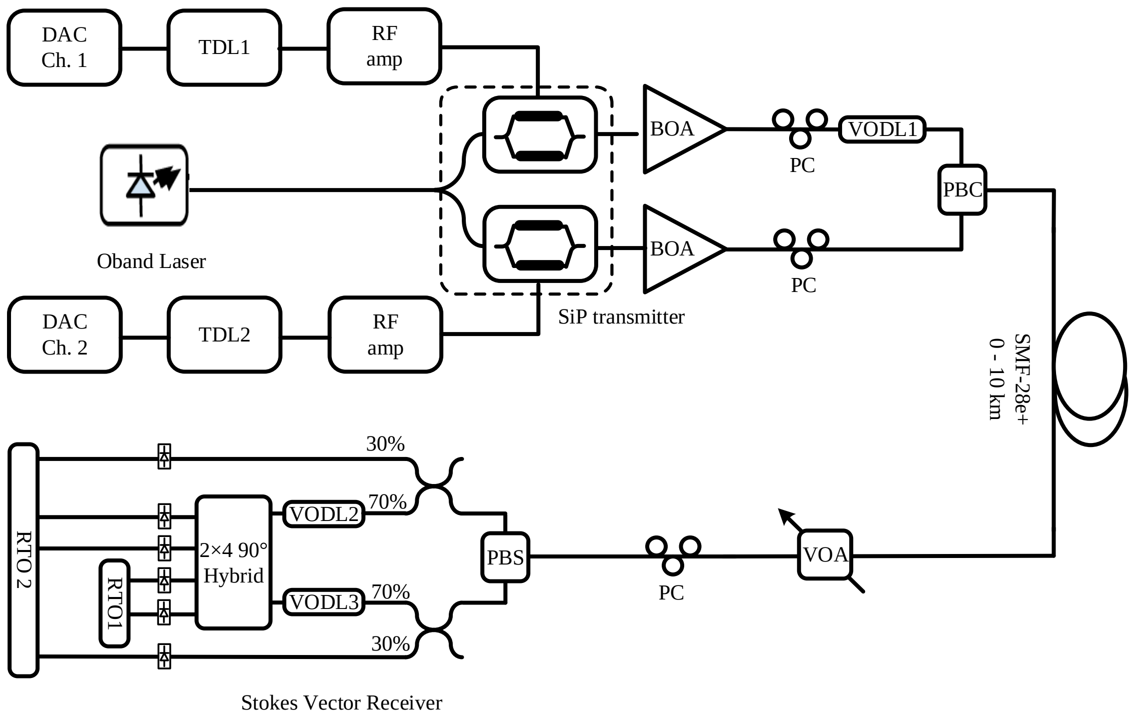

Figure 4.17. Experimental setup used to test the SiP modulator. DAC: digital to analog converter, TDL: tunable delay line, BOA: booster optical amplifier, VODL: variable optical delay line, PBC: polarization beam combiner, PC: polarization controller, VOA: variable optical attenuator, PBS: polarization beam splitter, RTO: real time oscilloscope.

of the 28, 42, and 56 Gbaud PAM-4 signals with roll-off factors of 1, 0.55, and 0.3 are 5.6 V, 4.7 V, and 3.1 V, respectively. An O-band laser operating at 1310 nm launches a 13.7 dBm optical carrier into the chip via the input grating coupler. The quadrature point is set using the thermal phase shifter of each modulator. A 1.5 V DC reverse bias voltage is applied to both modulators. This bias voltage was experimentally optimized to get minimum BER where an optimum trade off between the EO bandwidth and V_π is achieved. We reiterate here that the outputs of both modulators are not combined on chip due to the use of single polarization BOAs to compensate for the chip loss. A variable optical delay line (VODL) is added on one of the branches to be able to time align the signals on the two polarizations prior to combining by a polarization beam combiner (PBC). Then, the polarization multiplexed signal is launched into various lengths of SMF (Corning

SMF-28e+). A VOA is added to sweep the received signal power. The optical signal is then received by the SVR shown in Fig. 4.17, where the coupler splitting ratios have been chosen to be 70/30, close to the optimum ratio of 67/33 required for SOP independent operation [5]. A polarization controller (PC) is added before entering the receiver to vary the SOP and verify the performance dependence on received SOP. Since balanced PDs were not available in the O-band, single ended PDs are used in the experiment. The PDs have a bandwidth of 35 GHz and are followed by a TIA. The six signals out of the PDs are sampled at 80 GSa/s by two 33 GHz RTOs and stored for offline processing to be applied on the received electrical signals. The receiver DSP consists of resampling to 2 SPS, 6×2 real-valued MIMO equalization, symbol decision, and bit error counting. After resampling at 2 SPS, we feed the six output waveforms from the PDs to the MIMO DSP. The desired estimated outputs are the two intensities on both polarization, i.e., $\mid E_x^2 \mid$ and $\mid E_y^2 \mid$, and the taps are updated adaptively using the LMS algorithm. The MIMO DSP task is for polarization demultiplexing and residual ISI mitigation.

4.4.4 Experimental Results

Figures 4.18(a) and 4.18(b) show the BER and SNR performance versus received signal power of the 112 Gb/s DP-PAM2 signal at different SOPs in the B2B case. It can be observed that changing the SOP from completely aligned (0^o SOP) to completely misaligned (45^o SOP) has a negligible effect on the performance. This indicates the successful restoration of the transmitted dual-polarization signal using the 6×2 MIMO DSP block and proves the receiver is SOP independent as mentioned in the experimental setup. Approximately −5.5 dBm is needed to achieve a BER below the HD-FEC for a 112 Gb/s DP-PAM2 signal at any SOP in the B2B case. Increasing the received power further enhances the BER performance until reaching a BER of 1.17×10^{-6}, where the length of the captured frames is not enough to accurately measure the BER below 1×10^{-6}. Hence, we show the SNR versus received signal power in Fig. 4.18(b), where the BER is estimated to be lower than

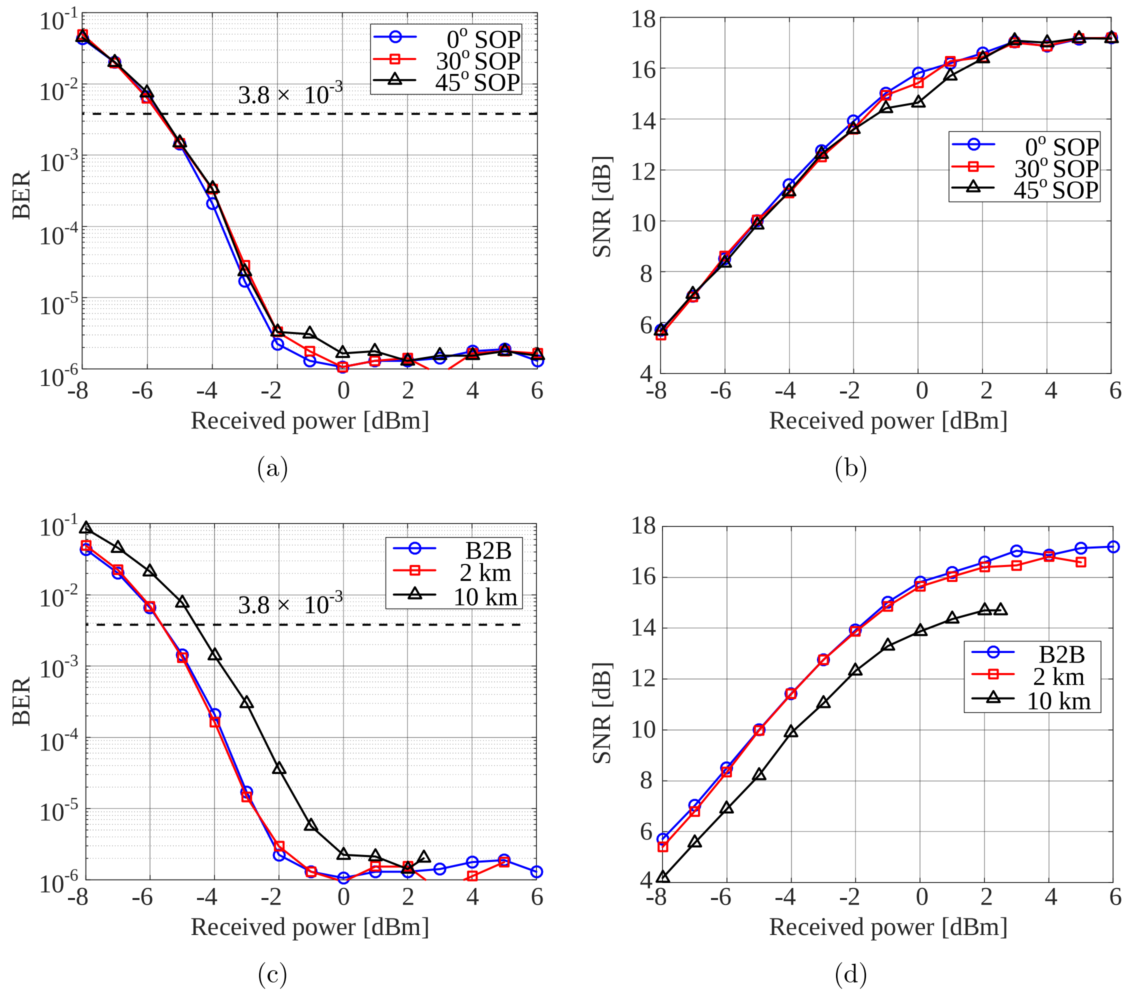

Figure 4.18. BER and SNR performance for the 112 Gb/s DP-PAM2 signal versus received power for (a-b) the B2B case at different SOPs and (c-d) over different reaches at random SOP.

1×10^{-6} at 0 dBm received signal power [126]. The SNR increases to 17 dB at 3 dBm received signal power, and then saturates with increased received power. In this regime, the SNR is no longer limited by the received signal power and is completely governed by the transmitter signal integrity. In Fig. 4.18(c), we present the BER performance versus received power over various reaches at random SOP. It can be observed that the degradation of the BER due to fiber transmission is minimal at equal received power for the 2 km case compared to the B2B case. However, the BER performance degrades when the reach

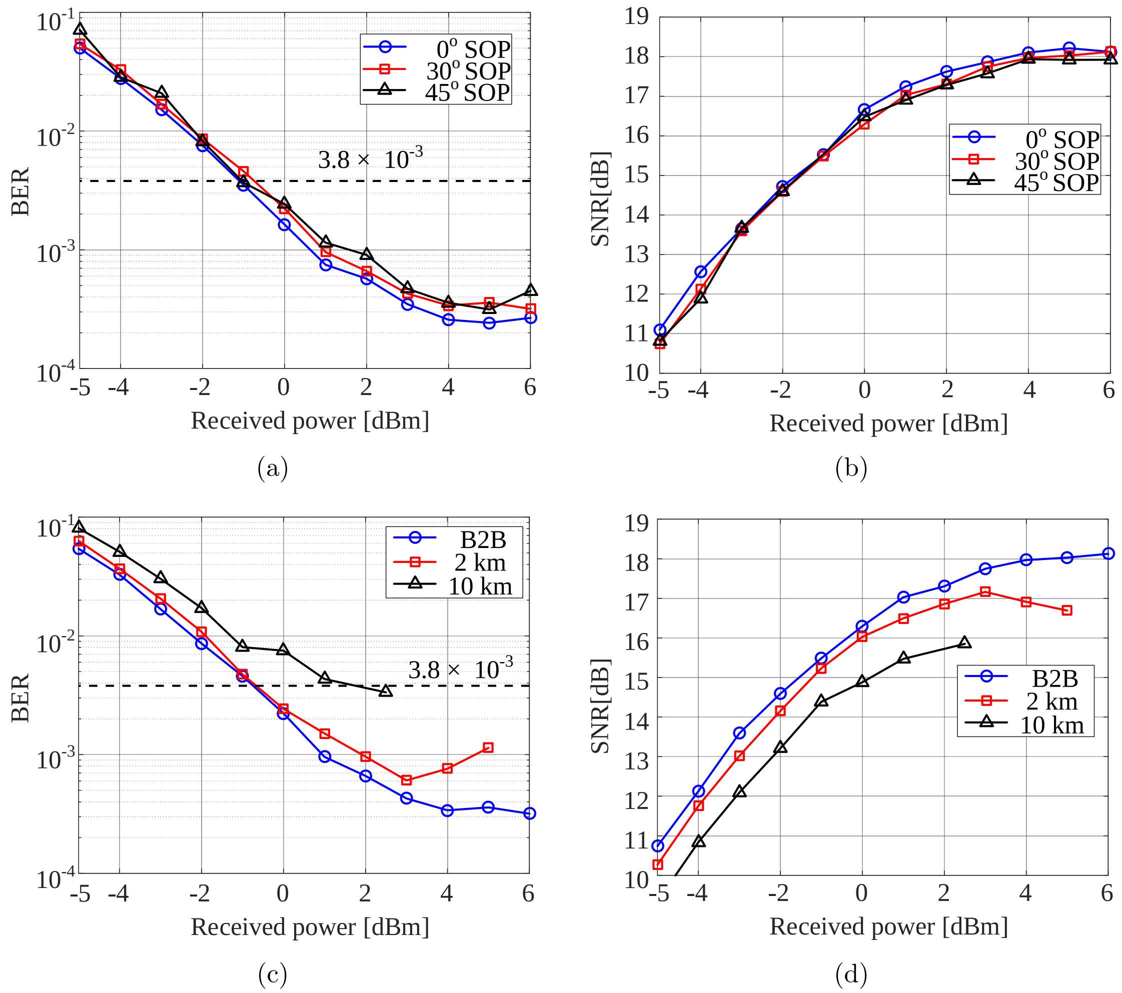

Figure 4.19. BER and SNR performance for the 168 Gb/s DP-PAM4 signal versus received power for the (a-b) B2B case at different SOPs and (c-d) random SOP over different reaches.

is increased to 10 km. A BER below the HD-FEC threshold is achieved at less than -5.5 dBm received signal power for the B2B and 2 km cases, and increases to -4.5 dBm for the 10 km case. Although this behavior is not expected in the O-band where chromatic dispersion is less significant, we observe approximately 1.5 dB SNR reduction in the 10 km case. Our explanation of this SNR reduction is based on the performance of the BOA which receives an input optical signal power exiting the SiP chip of ~ -14.5 dBm. At low input signal powers, we observed a significant amount of intensity noise in the received signal after fiber propagation over 10 km which was not significant in the B2B and 2 km cases. In contrast, the intensity noise almost vanishes when the input signal power to the BOA is above -5 dBm. Moreover, we find a dependency of this noise on the BOA current and temperature, where the noise increases with the BOA current, and decreases with increases in temperature. Hence, for the 2 km and 10 km curves, we optimized the temperature and BOA current to decrease the noise originating from the BOA after fiber propagation while having sufficient gain to amplify the input signal. We conclude that parasitic tone leakage and chirp from the BOAs is the reason for the additional intensity noise observed at the receiver, where it is pronounced after fiber propagation due to the interaction between tone leakage, chirp, and fiber dispersion. The effect is more significant on the performance of the PAM4 results as shown in the next section. Using a polarization insensitive amplifier as a pre-amplifier at the receiver side, e.g., a single PDFA should resolve this problem which was not available at the time of the experiment. Furthermore, an optical amplifier would not be used in deployed systems because packaged transceivers, including lasers, will have lower ILs.

We report the BER and SNR performance of 168 Gb/s (42 Gbaud) DP-PAM4 signal versus received power in Fig. 4.19. Similar to the DP-PAM2 results, we show that changing the SOP has a negligible effect on the performance as shown in Figs. 4.19(a) and 4.19(b). It can be observed in Fig. 4.19(a) that approximately -1 dBm received signal power is needed to achieve a BER below the HD-FEC at any received SOP. In Figs. 4.19(c) and 4.19(d), we present the performance at random SOP for different reach values. At 2 km reach, we notice a slight degradation in the BER and SNR performance compared to the B2B case. This is attributed to the BOA behavior as explained in the previous section. Furthermore, a higher driving BOA current is used for the 4 and 5 dBm received signal power points in Figs. 4.19(c) and 4.19(d). This results in the reduction of the SNR and consequently the BER increases due to the increased noise. For the 10 km reach, the SNR decreases by approximately 1.5 dB compared to the B2B case as shown in Fig. 4.19(d).

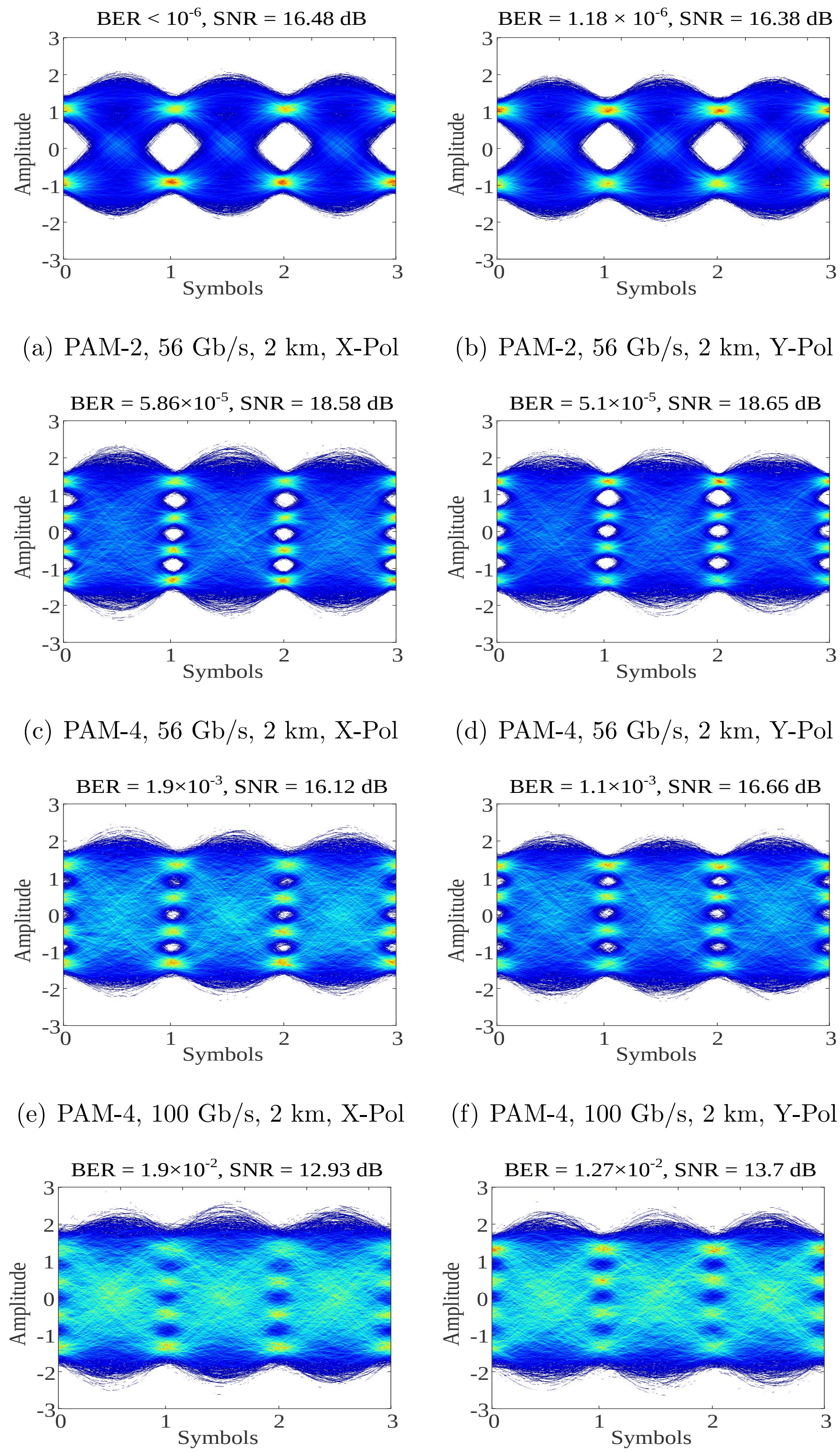

(a) PAM-2, 56 Gb/s, 2 km, X-Pol (b) PAM-2, 56 Gb/s, 2 km, Y-Pol

(c) PAM-4, 56 Gb/s, 2 km, X-Pol (d) PAM-4, 56 Gb/s, 2 km, Y-Pol

(e) PAM-4, 100 Gb/s, 2 km, X-Pol (f) PAM-4, 100 Gb/s, 2 km, Y-Pol

(g) PAM-4, 100 Gb/s, 10 km, X-Pol (h) PAM-4, 100 Gb/s, 10 km, Y-Pol

Figure 4.20. Eye diagrams for PAM2 and PAM4 modulation formats obtained after receiver DSP at different bitrates and reaches.

Hence, the BER increases and approximately 2 dBm received signal power is required to achieve a BER below the HD-FEC threshold. In the 10 km reach cases shown in Figs. 4.19(c) and 4.19(d) the maximum received signal power achievable was approximately 2.5 dBm based on maximum output power limitations of the BOA.

Figure 4.20 presents eye diagrams for the DP-PAM2 and DP-PAM4 signals at different bitrates after receiver DSP. In Fig. 4.20(a-b), a 112 Gb/s (56 Gb/s per polarization) DP-PAM2 is shown after 2 km of SMF, where a clear open eye diagram is observed.

Moreover, it is interesting to show the performance of the same signal bitrate (112 Gb/s) using the PAM4 modulation format which operates at half the symbol rate of the DP-PAM2 signal as shown in Fig. 4.20(c) and 4.20(d). The eye diagram of the 28 Gbaud signal shows a good eye opening, with a BER of 5.86×10^{-5} and 5.1×10^{-5} for the X-pol and Y-pol, respectively.

As expected, increasing the symbol rate further degrades the received signal quality, however 200 Gb/s is still achievable below the HD-FEC after 2 km of SMF with a relatively open eye diagram. Increasing the transmission to 10 km significantly degrades the performance for the 200 Gb/s compared to the 2 km reach due to the BOA behavior as discussed in the previous section. To re-iterate here, this problem is not related to the SiP transmitter but related to the BOA followed by SMF. This problem will be removed if the BOAs are used as pre-amplifiers after the polarization beam splitter or replaced by a polarization insensitive PDFA.

Figure 4.21(a) presents the BER versus the bitrate at different reaches for PAM2 and PAM4 modulation formats. The received signal power was kept at 3 dBm for the B2B and the 2 km curves, and at 2.5 dBm (the maximum available power based on BOA performance) for the 10 km curves. For the PAM2 signal, a bitrate up to 128 Gb/s over as much as 10 km can be transmitted at a BER below 4×10^{-6}. For the PAM4 signal, 224 Gb/s can be achieved in the B2B configuration below the HD-FEC threshold, where the BER increases to 4×10^{-3} after 2 km reach. Also, 200 Gb/s transmission over 2 km can

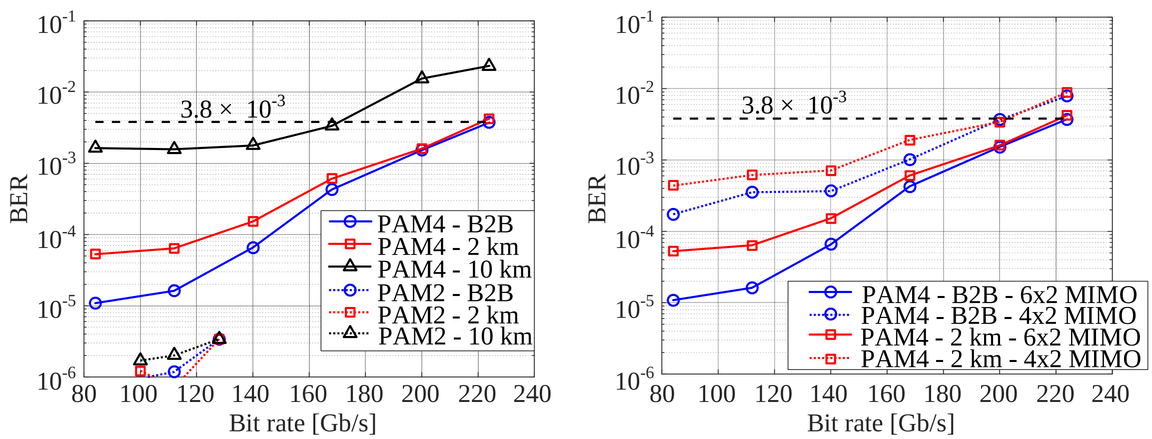

(a) (b)

Figure 4.21. (a) BER versus bitrate for PAM2 and PAM4 modulation formats for B2B, 2 km, and 10 km reaches, and (b) BER versus bitrate for PAM4 modulation format using 6×2 and 4×2 MIMO.

be achieved at a BER of 1.6×10^{-3}. Finally, only 168 Gb/s can be transmitted over 10 km with BER below the HD-FEC threshold.

As discussed in Section 4.4.3, we used 6×2 MIMO equalization for the polarization demultiplexing and residual ISI mitigation in all the previous results, where we feed the 6 electrical outputs from the real-time scopes directly to the MIMO. A simpler 4×2 MIMO can be used instead, where the differential pair outputs are first subtracted before the MIMO equalization. In Fig. 4.21(b), we compare the 6×2 and 4×2 MIMO equalization schemes for the DP-PAM4 modulation format in the B2B and 2 km cases. In our experiment, we used a custom-built O-band hybrid which had insertion losses of 6.5 dB, 7.2 dB, 6.38 dB, and 6.42 dB from input port 1 to the output ports, and 6.38 dB, 6.51 dB, 6.63 dB, and 6.87 dB from input port 2 to the output ports. Also, we used six single ended PDs, since no balanced PDs were available in the O-band, which have unequal conversion factors (V/W). The 6×2 MIMO is given by the following equation if we ignore the temporal length of the filters:

$$\begin{bmatrix} \mid E_{\hat{x}} \mid^2 \\ \mid E_{\hat{y}} \mid^2 \end{bmatrix} = \begin{bmatrix} h_{11} & h_{21} & h_{31} & h_{41} & h_{51} & h_{61} \\ h_{12} & h_{22} & h_{32} & h_{42} & h_{52} & h_{62} \end{bmatrix} \begin{bmatrix} \mid E_x^r \mid^2 \\ \mid E_y^r \mid^2 \\ S_{2p}^r \\ S_{2n}^r \\ S_{3p}^r \\ S_{3n}^r \end{bmatrix}$$

where $\mid E_{\hat{x}} \mid^2$ and $\mid E_{\hat{y}} \mid^2$ are the desired outputs, h_{ij} is the tap coefficient between input i and output j to the MIMO, $\mid E_x^r \mid^2$ and $\mid E_y^r \mid^2$ are the received DD outputs, S_{2p}^r and S_{2n}^r are the differential pairs for the S_2 parameter, and $S_{3p}^r$and S_{3n}^r are the differential pairs for the S_3 parameter. For the 4×2 MIMO, we subtract the two differential pair electrical outputs first and then feed them to the MIMO given by:

$$\begin{bmatrix} \mid E_{\hat{x}} \mid^2 \\ \mid E_{\hat{y}} \mid^2 \end{bmatrix} = \begin{bmatrix} h_{11} & h_{21} & h_{31} & h_{41} \\ h_{12} & h_{22} & h_{32} & h_{42} \end{bmatrix} \begin{bmatrix} \mid E_x^r \mid^2 \\ \mid E_y^r \mid^2 \\ S_2^r \\ S_3^r \end{bmatrix}$$

where S_2^r and S_3^r are the reconstructed stokes parameters from the differential waveforms after the direct detection terms are canceled.

Hence, the 6×2 MIMO will be capable of compensating the SVR imperfections e.g., power imbalance and the skew between the SVR outputs, and unequal PD responsivity. However, the simpler 4×2 MIMO will not be able to correct them since the differential pairs are subtracted before the MIMO and any residual common mode terms will degrade the performance. As a result, we can observe a degradation in the BER when the 4×2 MIMO is used as shown in Fig. 4.21(b). For example, the BER is $\sim 6 \times 10^{-5}$ using the 6×2 MIMO and increases to $\sim 6 \times 10^{-4}$ when using the 4×2 MIMO for 112 Gb/s DP-PAM4 in the 2 km case.

4.5 Conclusion

In this chapter, we proposed and experimentally demonstrated three PICs for DCI applications. Below we conclude the main results for the three designs

- A four lane 400 Gb/s based on MZMs is demonstrated for intra-datacenter optical interconnects. We reported the device details, small-signal, and large-signal characterization of the transmitter. The EO crosstalk between the four MZMs is studied in small-signal and large-signal. For large-signal modulation, we characterize the performance of the transmitter versus several parameters. Using only a 5-tap receiver FFE, 53 Gbaud PAM4 per lane can be received at a BER below the KP4-FEC threshold. Moreover, we show that the MZMs can be driven with a driving voltage swing below 1.8 Vpp and still achieve a BER below the KP4-FEC threshold for a 53 Gbaud PAM4 signal. Although, several 100 Gb/s demonstrations have been published to date based on SiP MZMs, we believe this is the best result for a MZM with a lateral PN junction in terms of driving voltage swing and equalization complexity to the best of our knowledge. Moreover, we demonstrate the first demonstration of a simultaneous modulation of a 4-lane transmitter running at an aggregate rate of 400 Gb/s with an average BER of approximately 1×10^{-4} for all lanes.

- We proposed an O-band 200 Gb/s SiP transmitter using two MEMZMs for short reach direct-detection applications. The MEMZMs have a V_π and EO bandwidth of 5 V and 38 GHz, respectively. Results reveal that up to 128 Gb/s per lane can be achieved using less than 2 Vpp and 1 Vpp voltage swings and 11-tap FFE at a BER below the KP4-FEC threshold. To the best of our knowledge, this presents the lowest drive voltage and number of FFE taps using a MEMZM delivering more than 100 Gb/s reported up to date. Moreover, we drive all segments simultaneously and assess the inter-MZM crosstalk. We observe a degradation in the BER performance due to the EO crosstalk, however, we can still operate at 200 Gb/s net rate over as much as 10 km at a BER below the KP4-FEC threshold using a relatively low voltage swing of 2.8 Vpp on segment 1 and 1.4 Vpp on segment 2, and 11-tap FFE at the receiver. Hence, the demonstrated transmitter presents a potential design for next generation 200 Gb/s intra-datacenter transceivers.

- A DP O-band SiP transmitter for intra-datacenter optical interconnects is experimentally demonstrated. The transmitter is tested for DP-PAM2 and DP-PAM4 formats using a DD-SVR versus various parameters. Results reveal that 112 Gb/s DP-PAM2 can be transmitted over as much as 10 km of SMF at a BER below 10^{-5} at -1 dBm received signal power and random SOP. Also, 168 Gb/s (42 Gbaud) DP-PAM4 signal can be transmitted over 2 km and 10 km at a BER below the HD-FEC at 0 dBm and 2 dBm, respectively. In addition, 224 Gb/s and 200 Gb/s DP-PAM4 is successfully received at a BER below the 7% HD-FEC in the B2B and 2 km cases, respectively. Finally, we explain the superior performance of the 6×2 MIMO compared to the 4×2 in the presence of SVR imperfections.

Chapter 5

System Level PAM4 demonstrations

5.1 Overview

In this chapter, we focus on single polarization PAM4 since it has been the selected modulation format by the 200 Gb/s and 400 Gb/s IEEE Ethernet standard. We present two system-level PAM4 demonstrations targeting intra-data center optical links. First, we demonstrate, in section 5.2, single polarization PAM4 on a single wavelength in the O-band operating at a net bitrate beyond 150 Gb/s targeting future optical transceivers operating at aggregate bitrates higher than 400 Gb/s. In section 5.3, we present a 400 Gb/s demonstration using a CWDM-TOSA that is compatible with the 400 Gb/s-FR4 MSA. Finally, we conclude in section 5.4.

5.2 Single polarization and wavelength PAM4 demonstration in the O-band

5.2.1 Motivation

In the last few years, several single polarization PAM4 experiments have been reported to cope with the global IP traffic increases. A 140 Gb/s PAM4 transmission over 20 km reach has been demonstrated at a BER of 5×10^{-4} in [127], where more than 100 equalizer taps and a post filter are needed at the receiver. Also, a selector power DAC has been used to enable 128 Gb/s PAM4 transmission over 3 km of SMF below the HD-FEC threshold [128]. In addition, a digital pre-processor, two DACs, and an analog multiplexer have been used to enable 160 Gb/s PAM4 over 20 km of SMF at a BER of 6.2×10^{-3} which is higher than the 3.8×10^{-3} FEC threshold with a significantly high complexity [129].

In this section , we study the BER performance of an O-band PAM4 system versus bitrate, number of receiver equalizer taps, received signal power, and reach. Results reveal that we can achieve up to 168 Gb/s PAM4 transmission over a 10 km reach below the 2×10^{-4} FEC threshold. This result demonstrates a 10 times improvement in the bit-rate-reach product while maintaining a performance below the 2×10^{-4} FEC threshold compared to the results in [130]. Also, we demonstrate 176 Gb/s PAM4 over 10 km reach below the HD-FEC threshold. At the time of the experiment, these results are the highest bitrates reported for O-band, single channel and single polarization PAM4 transmission over 10 km of SMF with DD applicable in DCI. In addition, we explore the BER dependence on the reach for an 84 and 88 Gbaud PAM4 signal at both constant launch power and constant received power representing an increase in signaling rate of 50% and more. We demonstrate that residual chromatic dispersion present at 1325 nm at a symbol rate as high as 88 Gbaud has no impact on the signal performance after as much as 10 km of SMF.

5.2.2 Experimental Setup

Figure 5.1 introduces the experimental setup. First, symbols are generated offline as per the transmitter DSP block diagram (Fig. 5.1(a)). The transmitter DSP includes symbol generation, RF spectral pre-compensation filtering at 1 sample per symbol (sps), clipping, and quantization. The number of taps for the pre-compensation filter are fixed at 75, however 99% of the filter energy is concentrated in only 21 taps. Then, symbols are loaded to an 8-bit DAC running at 1 sps except for Fig. 5.2(a) where pulse shaping is used for

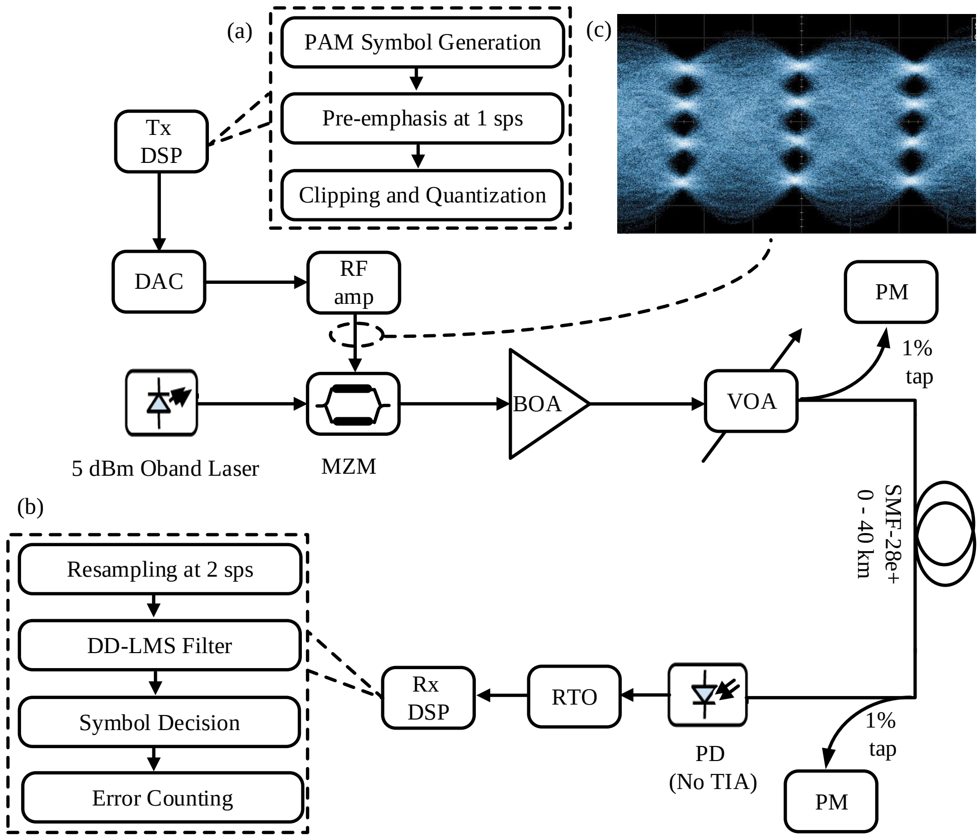

Figure 5.1. Experimental setup block diagram. Insets: (a) Transmitter DSP, (b) Receiver DSP, and (c) 84 Gbaud PAM4 eye diagram of the RF signal driving the MZM.

symbol rates lower than 84 Gbaud. The output RF signal from the DAC is amplified using a 50 GHz RF amplifier before modulating the optical carrier. The driving voltage is approximately 2 V_{pp} out of the amplifier. An 84 Gbaud PAM4 eye diagram after the RF amplifier is shown in Fig. 5.1(c). An O-band laser operating at 1325 nm launches a 5 dBm optical carrier to a 28 GHz lithium niobate MZM. The MZM has 5.5 dB IL, and biased at the quadrature point, giving a signal launch power of approximately -3.5 dBm. A BOA is necessary to provide sufficient received power to the PD, which does not have an inline TIA. A VOA is added after the BOA to sweep the received power. The signal is then launched into various lengths of SMF. Power meters are connected before and after the fiber spool using 1% power taps to monitor the signal power. The optical signal is received using a 50 GHz PD. Then, the signal is sampled at 160 GSa/s by a 63 GHz RTO and stored for offline processing. Finally, offline receiver DSP is applied on the received electrical signal as per Fig. 5.1(b). The DSP consists of resampling at 2 sps, decision directed LMS filtering, symbol decision, and bit error counting.

5.2.3 Results and Discussion

In this subsection, we present the experimental results of the PAM4 modulation format study versus different parameters. We consider two different FEC thresholds. First, according to the 400 Gb/s IEEE standard, KP4-FEC threshold at a BER of 2.4×10^{-4} should be considered. However, the operating BER for the 400 Gb/s standard was 2×10^{-4} at the time of the experiment which we consider in the results shown next. The second FEC is the 7% overhead HD-FEC (3.8×10^{-3}) which is added for fair comparison with results previously reported in the literature.

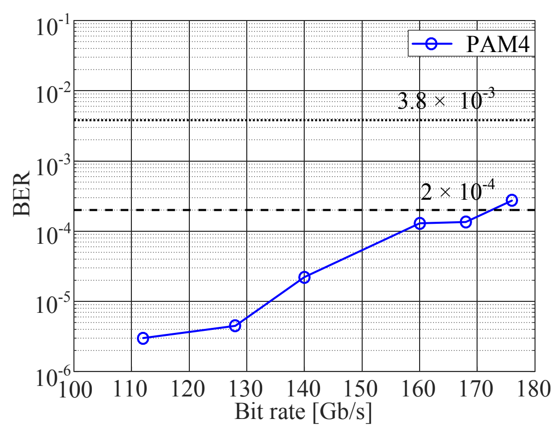

(a)

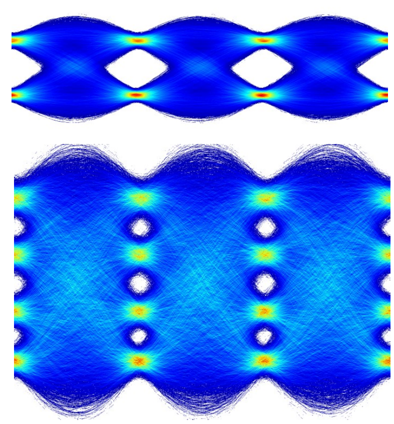

(b)

Figure 5.2. (a) B2B BER performance versus bitrate for PAM4 modulation format at 10 dBm received power. (b) 84 Gbaud PAM2 and PAM4 eye diagrams.

Figure 5.2 shows the B2B BER performance versus bitrate where the received power is fixed at 10 dBm. For symbol rates lower than 84 Gbaud, the DAC sampling rate is fixed at 84 GSa/s, and root raised cosine (RRC) pulse shaping is applied at the transmitter with the corresponding matched filter applied at the receiver. The roll-off factor α is chosen such that Symbol Rate $\times$ $(1+\alpha)=$ DAC Rate. The 168 and 176 Gb/s points are measured with the DAC running at 1 sps without pulse shaping. It can be observed that bitrates up to 172 Gb/s can be achieved below the 2×10^{-4} threshold. Also, we can reach up to 176 Gb/s at a BER of 2.8×10^{-4}. The PAM2 and PAM4 eye diagrams at 84 Gbaud after receiver DSP are shown in Fig. 5.2(b).

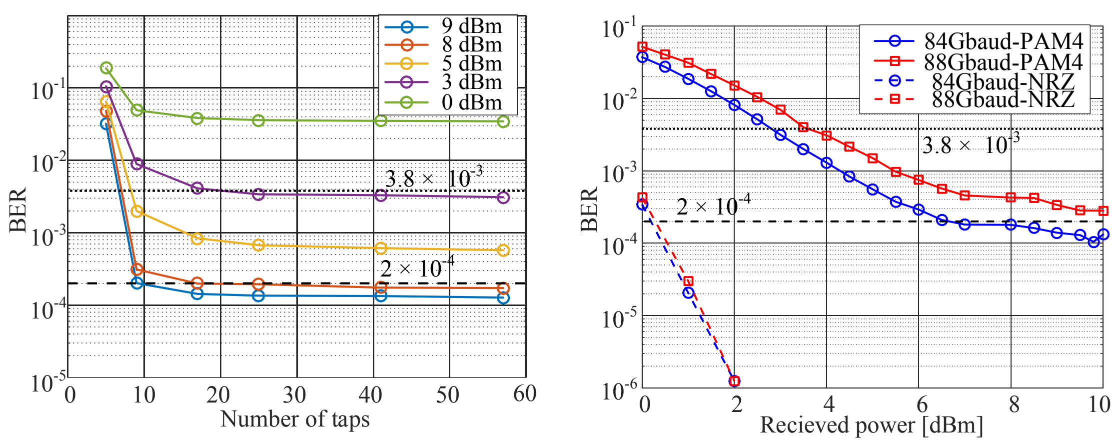

(a)

(b)

Figure 5.3. (a) 84 Gbaud PAM4 B2B BER performance versus number of FFE filtering taps for different received signal power, and (b) BER versus received power for 84 and 88 Gbaud NRZ and PAM4 modulation formats in the B2B configuration.

The BER performance versus receiver FFE taps for different received signal powers is reported in Fig. 5.3(a). Increasing the number of taps improves the BER performance at the expense of increasing the complexity, until reaching the optimal number of taps where further increases do not improve the BER. It can be observed that 17 taps are sufficient to reach an acceptable performance below the 2×10^{-4} threshold at 8 dBm of received signal power. Also, a BER of 2×10^{-4} can be achieved using 9 taps at a higher received signal power of 9 dBm. The number of taps was fixed to 57 taps for the rest of the figures.

Figure 5.3(b) presents the BER performance against the received signal power for both

84 and 88 Gbaud NRZ (PAM2) and PAM4 modulation formats, where the NRZ performance is added for completeness. As expected, the BER decreases with an increase of the received signal power, and approximately 3 dBm and 4 dBm are needed to achieve 168 Gb/s and 176 Gb/s PAM4, respectively, below the 3.8×10^{-3} FEC threshold. Using a PD followed by a high bandwidth TIA will significantly relax the required received power [131]. For NRZ, less than 0.5 dBm is required to achieve the 2×10^{-4} threshold and the BER is lower than 10^{-6} beyond 2 dBm received power.

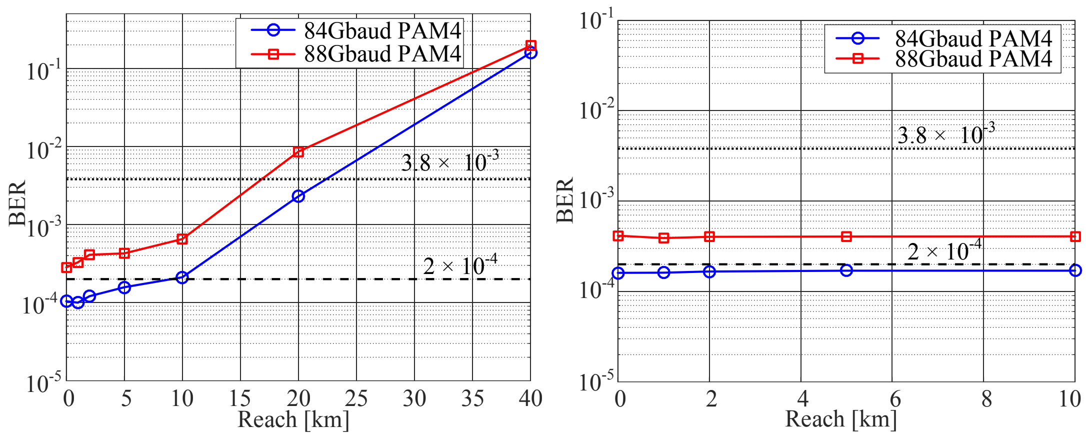

(a) Constant launch power.

(b) Constant received power.

Figure 5.4. BER versus reach for 84 and 88 Gbaud PAM4 at (a) 9.5 dBm launch power to the SMF, and (b) 8 dBm received signal power.

Figures 5.4 represent the BER performance versus the reach for two different scenarios. In Fig. 5.4(a), we fix the launch power at 9.5 dBm such that sufficient power is delivered after 10 km of SMF for the receiver to operate below the FEC threshold. As expected, the BER performance deteriorates with the increased reach. For the 84 Gbaud curve, we can achieve transmission over 10 km at a BER of 2.1×10^{-4}, and up to 22 km below the 3.8×10^{-3} threshold. In addition, 88 Gbaud can reach up to 17 km below the 3.8×10^{-3} threshold. In Fig. 5.4(b), we fix the received signal power at 8 dBm by controlling the launch power using both a BOA and a VOA. The maximum output power of the BOA is approximately 13.5 dBm which limited the transmission to 10 km at 8 dBm received signal power. For longer reaches, a second BOA can be used at the receiver side as a pre-amplifier to maintain the received signal power and avoid fiber non-linear effects. It can be observed that at 8 dBm received signal power the BER for 84 and 88 Gbaud is nearly independent of the reach, operating at 1.6×10^{-4} and 4×10^{-4}, respectively. Hence, the deterioration of the BER performance in Fig. 5.4 is mainly due to the fiber loss with negligible contribution from fiber chromatic dispersion and fiber non-linearity. As a result, the BER performance is dominated by the received power in Fig. 5.3(b), and longer reach values can be attained provided that sufficient signal power is received.

5.3 400 Gb/s CWDM-TOSA

5.3.1 Motivation

As mentioned in Chapter 1, the 400GBase IEEE standard over 2 and 10 km of SMF is: 25 Gbaud, PAM4, and eight WDM lanes with 800 GHz spacing in the O-band [2]. In 2018, the 100G Lambda MSA, supported by a broad industry consortium, has been recently formed providing specifications for 100 Gb/s per lane [3]. Leveraging the 100 Gb/s per lane, the MSA established the 400 Gb/s transceivers technical specifications over 2 km of SMF (400G-FR4): 50 Gbaud PAM4, and four lanes on the CWDM grid [3]. Moreover, a 400 Gb/s MSA targeting the 10 km reach is under discussion.

Table 5.1 summarizes 400 Gb/s demonstrations compared to this work, including [132] which represents a recently published demonstration that is compliant with the IEEE 400GBASE-LR8 specifications. In [133], the first real-time transmission of 400 Gb/s (8 $\times$ 50 Gb/s) PAM-4 signals for DCI up to 100 km of SMF is successfully demonstrated using discrete components and bulk modulation. In [116], eight-channel hybrid multi-chip module comprising InP lasers, SiP modulators, and parallel SMFs, all connected via photonic wire bonds is presented which can achieve 400 Gb/s aggregate bitrate. However, each lane is tested individually using RF probes while cross-talk between the modulators

Table 5.1. Comparison of our work with previous 400 Gb/s demonstrations.

Ref.	Tx structure	Package	Band	No. of channels	Spacing	Reach	Optical Amp.	FEC threshold
[132; 2017]	8 DMLs + Mux	CFP8	O-band	8λ	800 GHz (LWDM)	10 km	No	2.4×10^{-4}
[132; 2017]	8 EMLs + Mux	CFP8	O-band	8λ	800 GHz (LWDM)	10 km	No	2.4×10^{-4}
[133; 2016]	2 MZMs (Bulk mod.)	discrete	C-band	8λ	50 GHz (DWDM)	100 km	Yes	5.2×10^{-5}
[116; 2017]	8 DFBs + 8 SiP MZMs	chip-level	C-band	8 fibers	PSM*	2 km	No	3.8×10^{-3}
[134; 2015]	4 EMLs	TOSA	O-band	4λ	800 GHz (LWDM)	2 km	No	3.8×10^{-3}
This work	**4 EMLs + MUX**	**TOSA**	**O-band**	**4λ**	**20 nm (CWDM)**	**20 km**	**No**	$\mathbf{2.4 \times 10^{-4}}$

* Parallel single mode fibers.

is expected to degrade the performance when operating simultaneously [117]. Also, the module is far from commercial products due to the operating wavelength, performance, size, reliability, and yield. In [134], 465 Gb/s net rate has been achieved using four commercial 25 Gb/s EMLs on the LAN-WDM (LWDM) grid, i.e, 800 GHz spacing. However, equalization, post filtering, and maximum likelihood sequence estimation are needed to compensate for the induced inter-symbol interference due to the EML limited bandwidth.

In this section, we present the first transmission demonstration of a four lane 400 Gb/s CWDM TOSA that meets key 400G-FR4 MSA specifications and can support a QSFP-double density transceiver form factor. Four lanes, each running at 53 Gbaud PAM4, are used to drive the four lane CWDM-TOSA with a net data rate of 400 Gb/s. We report the performance of the TOSA versus received optical modulation amplitude (OMA), number of taps, reach, modulation format, TOSA case temperature, and bitrate. Results reveal that using only a 5-tap T-spaced FFE at the receiver, 400 Gb/s transmission over 2 km of SMF is achieved at a BER below the KP4-FEC threshold of 2.4×10^{-4} at -5 dBm OMA for the worst lane. In addition, we demonstrate 400 Gb/s over up to 20 km reach below the KP4-FEC without optical amplification. Moreover, we report 600 Gb/s over 10 km of SMF at aBER below the HD-FEC of 3.8×10^{-3} using the same CWDM-TOSA enabled by an 11-tap FFE at the receiver. Furthermore, we show that reach can be extended to 40 km using an optical amplifier for the lanes where the dispersion effect is not dominant. The TOSA performance versus operating temperature is also assessed and we show that the TOSA can operate over temperature range from 20°C to 60°C without performance degradation. Finally, we compare the performance of PAM2, PAM4, and PAM8 modulation formats, where we show that 100 Gb/s per lane can be achieved using the same TOSA running at 35 Gbaud PAM8.

5.3.2 Experimental setup

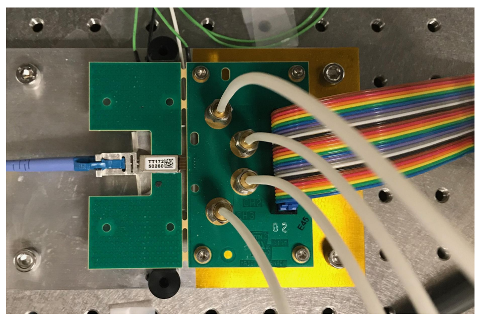

(a)

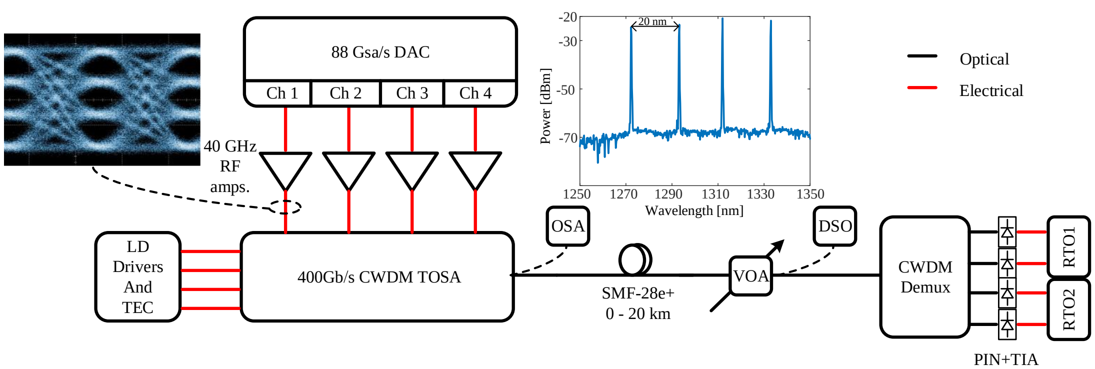

(b)

Figure 5.5. (a) An image for the TOSA soldered to the RF board in the test bed, and (b) experimental setup used for the 400G CWDM-TOSA testing. Insets: 53 Gbaud RF signal out of the amplifier, and optical spectrum out of the TOSA. DAC: digital-to-analog converter, TEC: temperature controller, OSA: optical spectrum analyzer, VOA: variable optical attenuator, DSO: digital sampling oscilloscope, and RTO: real time oscilloscope.

The TOSA is a 400 Gb/s CWDM device based on uncooled InP EML technology and it utilizes four EMLs followed by a CWDM multiplexer. The nominal wavelengths of the EMLs are 1271 nm, 1291 nm, 1311 nm, and 1331 nm. The compact size of the TOSA can support QSFP-DD transceiver form factor. As shown in the photo in Fig. 5.5(a), the TOSA was soldered to an RF board with 2.4 mm RF connectors for the input RF signals, and DC connections for the laser current sources. Also, a temperature controller (TEC) is needed to sweep the TOSA case temperature as shown later in Fig. 5.11(b). Figure 5.5(b) shows the experimental setup. Four lanes of an ILX-3916 laser diode controller are used to drive the lasers. An 8-bit DAC running at 88 GSa/s is used to generate four PAM4 signals. The output RF signals from the four lanes of the DAC are amplified using four 40 GHz RF amplifiers followed by four bias-Ts each with a 3-dB bandwidth of 65 GHz for applying the modulator bias. A 53 Gbaud PAM4 eye diagram after the bias-T for one of the driving lanes is shown in the top-left inset of Fig. 5.5(b). At the transmitter side, we only pre-compensate the response of the DAC and RF amplifier. The optical spectrum of the 400 Gb/s CWDM signal at the output of the TOSA captured using an optical spectrum analyzer (OSA) is shown in the top-right inset in Fig. 5.5(b). The optical signal is then launched into various lengths of SMF (Corning SMF-28e+) covering reaches ranging from 500 m to 20 km without optical amplification. A VOA is added before the receiver to sweep the received signal power, and consequently the received OMA. At the receiver side, a commercial CWDM demultiplexer followed by four 40 GHz photoreceivers (PD+TIA) are added. The four signals out of the photoreceivers are sampled at 160 GSa/s by two 62 GHz RTOs and stored for offline processing. The offline processing includes: resampling, equalization, and bit error counting. In order to minimize the required DSP, we use only 5 tap T-spaced FFE for the 400 Gb/s results which compensates for the combined response of the RF board, TOSA, and the photoreceiver (per above, the response of the DAC and RF amplifier has already been pre-compensated).

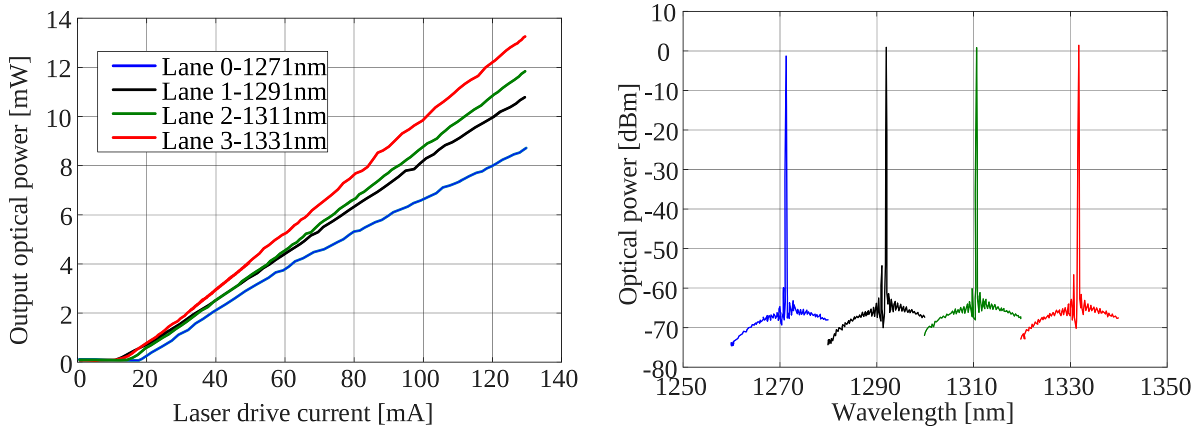

(a) (b)

Figure 5.6. (a) Light-current characteristics, and (b) measured optical spectra for the four CWDM lasers.

5.3.3 Experimental results

Figure 5.6(a) presents the light-current characteristics for the four CWDM lasers at 40 °C. The value of the threshold current for the four lasers ranges from 11.2 to 17.5 mA. The measured optical spectra are shown in Fig. 5.6(b), where the side mode suppression ratio (SMSR) is more than 55 dB for the four lasers.

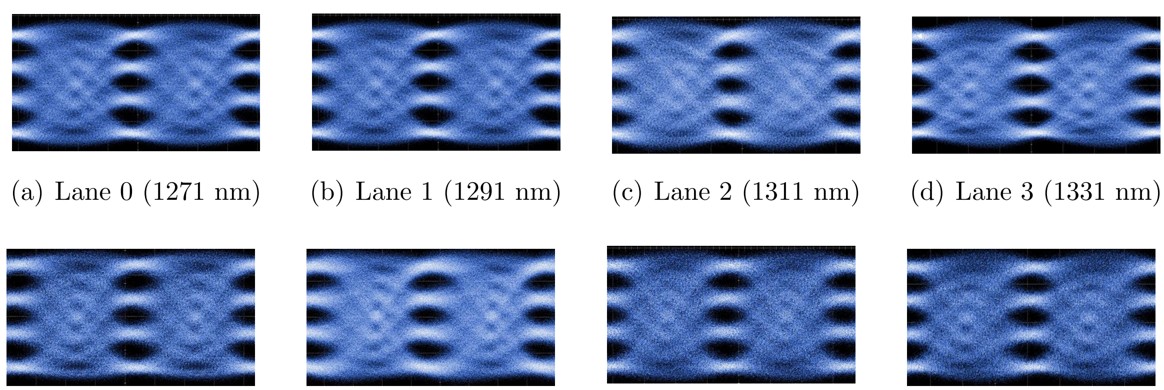

(a) Lane 0 (1271 nm) (b) Lane 1 (1291 nm) (c) Lane 2 (1311 nm) (d) Lane 3 (1331 nm)

(e) Lane 0 (1271 nm) (f) Lane 1 (1291 nm) (g) Lane 2 (1311 nm) (h) Lane 3 (1331 nm)

Figure 5.7. (a)-(h) Optical eye diagrams for the four received lanes at the demultiplexer output equalized using a 5 tap FFE on the digital sampling oscilloscope in the B2B (top) and 2 km (bottom) cases.

Figure 5.7 shows clear open optical eye diagrams captured using a 65 GHz optical

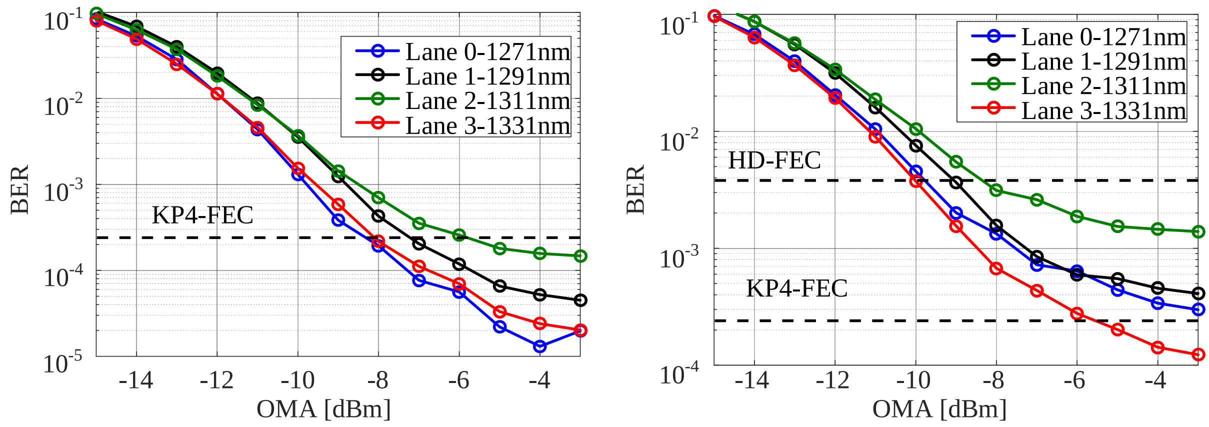

(a) (b)

Figure 5.8. (a) BER performance versus received OMA for the four lanes running at 53 Gbaud each in the B2B case equalized using a 5 tap FFE, and (b) BER performance versus received OMA for the four lanes running at 64 Gbaud each in the B2B case equalized using a 5 tap FFE.

sampling head of a Keysight DSO in the B2B and 2 km cases for all lanes after the demultiplexer. A 5-tap T-spaced FFE is applied to the eye diagrams using the built-in FFE in the DSO.

Figure 5.8(a) presents the B2B BER performance versus OMA for all lanes running at 53 Gbaud PAM4 yielding a net rate of 400 Gb/s. It can be observed that all four lanes can achieve a BER below the KP4-FEC threshold at an OMA of approximately -5 dBm for the worst lane. Lane 2 shows a slightly worse performance compared to the other lanes, which can be attributed to a slightly smaller bandwidth. Similarly, we show in Fig. 5.8(b) the BER performance versus received OMA when the symbol rate is increased to 64 Gbaud while having the same number of taps.

In Fig. 5.9(a), the transmission performance of all lanes over SMF for 400 Gb/s net rate is tested over reaches ranging from 500 m to 20 km without optical amplification. The OMA is fixed at -4 dBm for all points, and the receiver equalizer taps are fixed at 5 taps. It can be observed that 400 Gb/s can be transmitted over as much as 20 km of SMF without optical amplification at a BER below the KP4-FEC threshold. To the best of

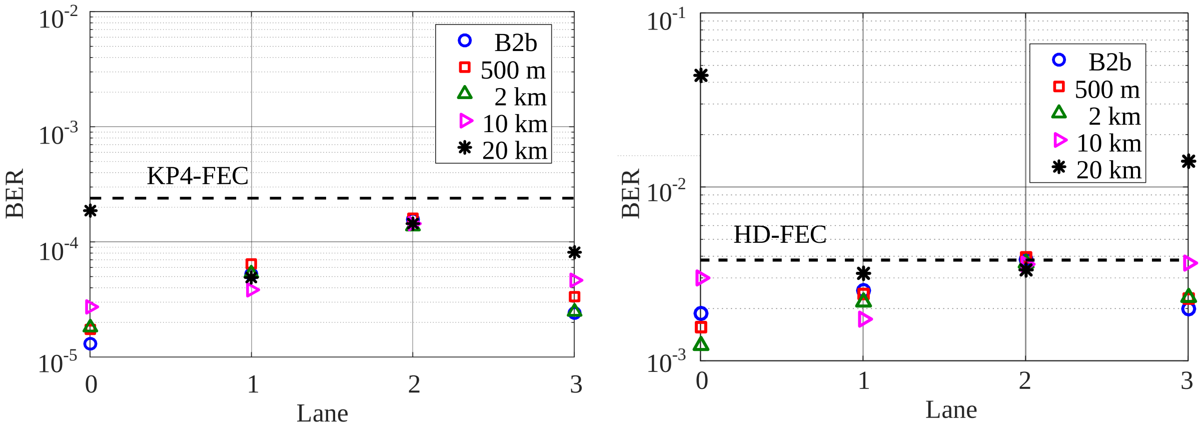

(a) (b)

Figure 5.9. (a) BER performance for all lanes running at 400 Gb/s aggregate net rate over different reaches using 5 tap receiver FFE, and (b) 75 Gbaud per lane (600 Gb/s) BER performance over different reaches using 11 tap FFE.

our knowledge, this is the first experimental demonstration of 400 Gb/s transmission over 20 km of SMF using a four lane CWDM TOSA with all lanes simultaneously modulated. For lane 0 (1271 nm), we see a larger penalty compared to the other lanes after 20 km transmission, which is expected since this lane is more than 40 nm away from the SMF zero dispersion wavelength. However, we can still achieve 20 km transmission on this channel using a 5 tap equalizer, and increasing the equalizer taps can significantly improve the performance. Figure 5.9(b) presents the BER performance for all lanes driven by 75 Gbaud PAM4 signals, yielding 600 Gb/s bitrate (75 Gbaud/lane) over 10 km reach below the HD-FEC threshold (3.8×10^{-3}) using an 11 tap T-spaced FFE.

Figure 5.10(a) presents the performance versus the number of FFE taps for lane 0, which is the lane most affected by fiber dispersion, at 75 Gbaud PAM4 in the B2B and 10 km cases. Increasing the number of taps improves the BER performance until reaching 31 taps where further increases show a small BER improvement. Next, we sweep the bitrate for lane 0 at different reaches using 5 and 31 taps in Fig. 5.10(b). It can be observed that up to 70 Gbaud over 10 km reach can be received below the HD-FEC threshold using only

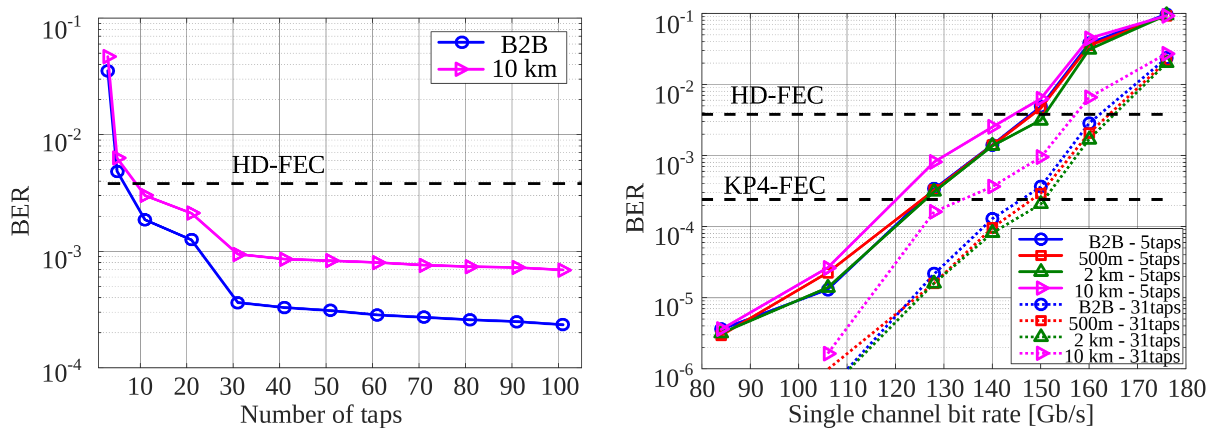

(a) (b)

Figure 5.10. (a) BER performance versus number of receiver FFE taps for lane 0 running at 75 Gbaud in the B2B and 10 km cases, and (b) BER versus bitrate using 5 and 31 receiver FFE taps at -5 dBm received signal power for lane 0.

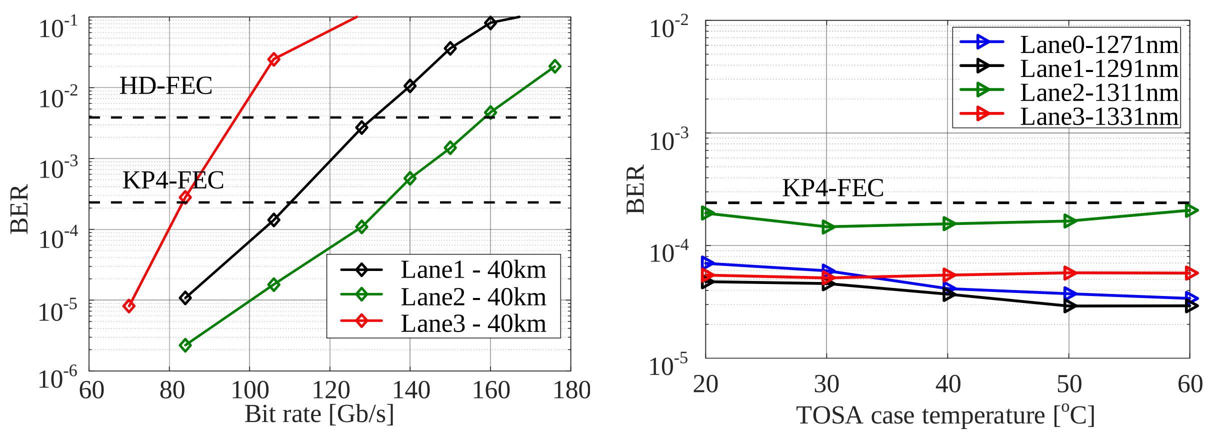

(a) (b)

Figure 5.11. (a) BER versus bitrate after 40 km reach using 31 FFE taps, and (b) BER versus TOSA case temperature at constant received signal power for 400 Gb/s net rate over 10 km reach.

5 taps at the receiver. Increasing the number of taps to 31 taps, 80 Gbaud over 2 km reach can be received at a BER below the HD-FEC threshold.

Next, we extend the reach to 40 km by adding a PDFA as a pre-amplifier. Figure 5.11(a) show the BER performance versus bitrate over 40 km reach for different lanes. The number of taps is increased to 31 FFE taps to compensate for the dispersion over 40 km except lane 0 where the dispersion is more pronounced and more aggressive equalizer is needed (e.g., using maximum likelihood sequence detection). Lane 2 shows the best BER performance where 128 Gb/s can be received after 40 km at a BER below the KP4-FEC since its wavelength is the closest to the fiber's zero dispersion wavelength. Also, the BER performance degrades for lanes 1 and 3 where 128 Gb/s and 90 Gb/s can be received at a BER below the HD-FEC, respectively. Furthermore, we assess the effect of the TOSA case temperature on the BER performance for all lanes running at 53 Gbaud over 10 km reach in Fig. 5.11(b). The temperature is varied from 20°C up to 60°C, where the received power is kept constant using the VOA since the laser power decreases with increasing temperature. It can be observed that varying the temperature over this range has a negligible effect on the BER performance, and 400 Gb/s transmission over 10 km can be achieved over the entire temperature range.

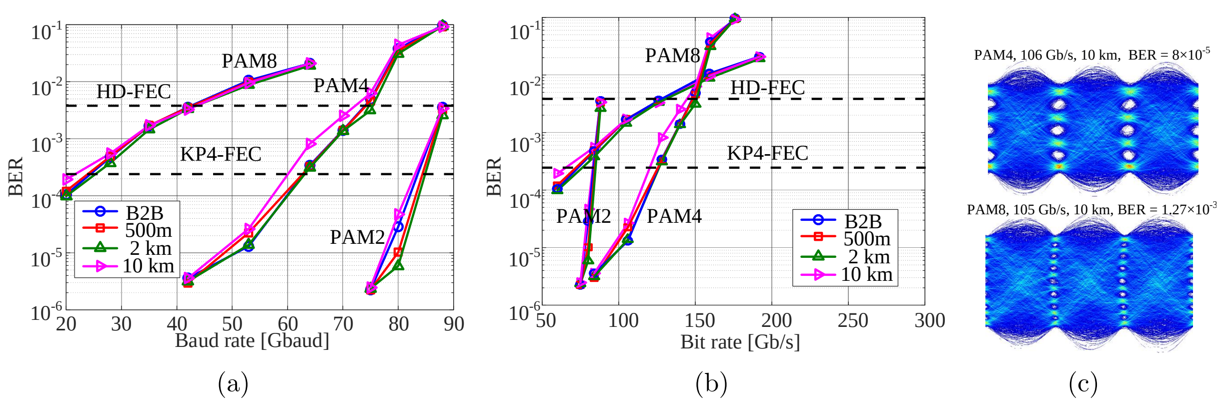

Figure 5.12. BER versus (a) baud rate and (b) bitrate for different modulation formats over different reaches, and (c) eye diagrams after receiver DSP for PAM4 and PAM8 modulation formats running at 53 and 35 Gbaud, respectively.

Finally, we compare the BER performance versus symbol rate for PAM2, PAM4, and PAM8 modulation formats for different reaches for lane 0 in Fig. 5.12(a). Also, we add the BER performance versus bitrate for more clarity in Fig. 5.12(b). To reiterate here, the modulator transfer function is not precompensated at the transmitter side. The number of receiver FFE taps is fixed at 5, 5, and 51 taps for PAM2, PAM4, and PAM8, respectively.

Eye diagrams after receiver DSP for 106 and 105 Gb/s signals after 10 km of SMF using PAM4 and PAM8 modulation formats, respectively, are shown in Fig. 5.12(c). The received signal power was kept at -5 dBm for all curves. For the PAM2 signal, a bitrate up to 88 Gb/s over as much as 10 km can be transmitted at a BER below the HD-FEC threshold. It is interesting to notice that to achieve 100 Gb/s per lane while still having low complexity, PAM4 modulation format is favored over PAM2. However, a higher BER is achieved and a relatively stronger FEC is needed, i.e., KP4-FEC, comparing 50 Gbaud PAM2 and PAM4. Similarly, we can see a crossing point above 150 Gb/s between PAM4 and PAM8 modulation formats which suggests that pushing further will require using PAM8 instead to decrease the bandwidth requirement compared to PAM4. What we forecast in our paper that with the development of better electrical signal generators compared to the limited effective number of bits and bandwidth of our DAC, PAM8 signal generation can be less complex. Also, better modulators with more superior linearity are needed for the PAM8 electrical-to-optical mapping. Hence, operating at lower baud rate can achieve equal and higher net bitrates compared to PAM4 modulation formats at the expense of adopting a stronger FEC.

5.4 Conclusion

In this chapter, we presented two system-level PAM4 demonstrations and the results are summarized below.

- In the first experiment, we experimentally demonstrate 168 Gb/s and 176 Gb/s single polarization PAM4 transmission over 10 km SMF in the O-band below a BER of 2×10^{-4}, and the HD-FEC threshold, respectively. The BER performance of the PAM4 signal is evaluated versus bitrate, number of equalizer taps, received power, and reach. Results reveal that at rates up to 168 Gb/s, PAM4 can be transmitted over 20 km below the HD-FEC threshold at 9.5 dBm launch power. Finally, we report independent BER performance of the reach at constant received power at symbol rates of 84 and 88 Gbaud.

- The first demonstration of 400 Gb/s (4λ× 100 Gb/s) CWDM-TOSA targeting 400G-FR4 requirements is presented in section 5.3. We present a detailed system-level study of the CWDM-TOSA versus several parameters. Four 53 Gbaud PAM4 RF signals are used to drive the TOSA achieving a net rate of 400 Gb/s. Results reveal that 400 Gb/s can be transmitted over up to 2 km of SMF at a BER below the KP4-FEC threshold using only a 5 tap FFE at the receiver at −5 dBm OMA. To the best of our knowledge, this is the first demonstration of 400 Gb/s using a 4λ CWDM TOSA over 2 km of SMF. Also, we show the TOSA is capable of achieving 400 Gb/s over 20 km, and 600 Gb/s over 10 km below the KP4- and HD-FEC thresholds, respectively, without optical amplification. Furthermore, we show the performance of the TOSA against case temperature, where it shows no significant change in the BER performance from 20°C to 60°C. Finally, we compare the performance of PAM2, PAM4, and PAM8 modulation formats where we show the possibility of achieving a higher bitrate using PAM8 modulation format at the expense of utilizing a stronger FEC.

Chapter 6

Conclusion and Future Work

6.1 Overview

Owing to the continuous growth of cloud based services, datacenters have experienced unprecedented traffic increases. To cope with these increases, 100 Gb/s short reach optical transceivers are currently being deployed. The next generation of optical transceiver modules will operate at 200 Gb/s and 400 Gb/s aggregate bitrates. Different material platforms are considered for the PIC design such as InP and SiP. The SiP platform has been accepted as a competitive platform for intra- and inter-datacenter optical transceivers either direct-detection or coherent due to several advantages. The SiP platform has the potential to build compact, high yield, high performance, and low cost CMOS compatible transceivers. The objective of this thesis spans different areas of optical transceivers including passive SiP designs, active SiP designs, PICs, and system-level demonstrations.

6.2 Summary of original contributions

Figure 6.1 presents a summary of the original contributions of this thesis. Hereafter, we highlight the main results for each chapter of this thesis.

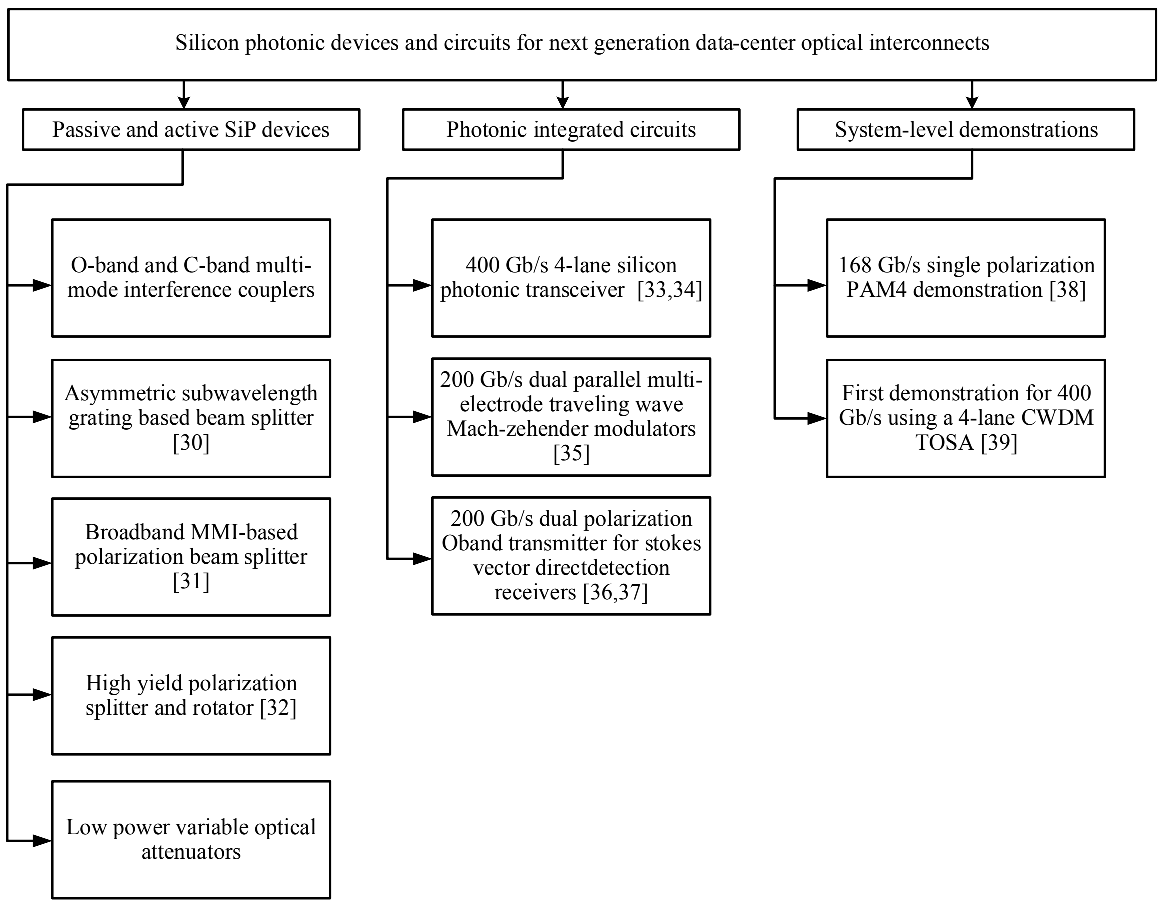

Figure 6.1. Summary of original contributions.

6.2.1 Passive and active silicon photonic devices

In Chapter 3, we presented several SiP passive and active components that are essential in any optical transceiver PIC. The devices include splitters, polarization handling devices, and VOAs. Below, we summarize the function of the designed devices and the key results achieved.

- First, a 2 × 2 MMI based 3-dB coupler operating in the O-band is presented. The device has a simulated bandwidth of more than 80 nm and a power imbalance below 0.2 dB. The MMI was fabricated on a 200 mm wafer, and tested using an automated wafer-tester. The splitting ratio is close to 3 dB over 80 nm bandwidth with a maximum imbalance of ±0.5 dB. Moreover, we presented the wafer-level splitting ratio across more than 45 dies where the coupling ratio has a standard deviation of only 0.042 dB across the entire wafer which shows the high yield of the MMI design.

- Then, we present a modified MMI design to achieve both asymmetric splitting ratios and large bandwidth. Using a cut in one of the MMI sides, the symmetry is broken and different splitting ratios can be achieved. Also, we used SWGs in the MMI slab to design for much larger bandwidth and small foot-print. The AMMI is designed to operate over more than 100 nm including the entire C-band with splitting ratios varying from 50:50 to 90:10 depending on the length of the asymmetry. The AMMI has a compact size of only 23.7 µm × 3 µm. The AMMI is fabricated using EBeam lithography, and tested on a passive test station. Results reveal that different splitting ratios are obtained with a deviation of less than ± 7% over 100 nm bandwidth.

- In section 3.4, we presented a C-band SiP PBS based on cascaded MMIs. Since the effective index is different for the TE and TM polarizations, by adjusting the dimensions of the MMI, the different polarizations can be directed to different MMI ports. Also, by cascading MMIs, residual crosstalk can be filtered to increase the ER. The designed PBS has dimensions of 364 µm × 10 µm, and was fabricated using single etch EBeam. The experimental results show that an ER of approximately 14 dB and 20 dB can be achieved over more than 50 nm including the entire C-band from the upper and lower ports of the PBS, respectively.

- A high yield, low IL, and broadband PSR is demonstrated for C-band and O-band PICs. The design is based on three sections: polarization rotator, adiabatic coupler, and clean-up filters and bends. Simulations shows the robustness of the design for fabrication variations. The PSRs are fabricated on 200 mm wafer in a CMOS foundry. The measured C-band PSR has negligible ILs and ER of more than 20 dB over 90 nm bandwidth. Moreover, more than 10 dB improvement in the ER is achieved by adding the clean-up filter at the output. For the O-band PSR, we can achieve more than 20 dB ER over 80 nm bandwidth including the entire CWDM grid. In addition, we showed wafer scale data for the O-band design where the minimum ER over 80 nm bandwidth has an average of 21.82 dB and 19.05 dB with a standard deviation of 2.42 dB and 1.559 dB for the upper and lower ports, respectively.

- Finally, we demonstrate low power VOA based on a MZI based switch cell which is a crucial component of ICRs and SVRs. Several variations are designed including different splitters, different heater length and width, with and without substrate undercut, and operating wavelength. The designed VOAs were fabricated using EBeam lithography then metal heaters were formed. A substrate undercut process was developed to suspend the MZI waveguides to achieve low power consumption. Experimental results show that the VOA without substrate undercut consumes approximately 18 mW and 27 mW to achieve 5 dB and 20 dB attenuation, respectively. Including the substrate undercut, the power consumption to achieve 5 dB and 20 dB attenuation is improved to be 5 mW and 8 mW, respectively. This represents more than 3X improvement in the power consumption. On the other hand, the 3 dB bandwidth of the VOA is approximately 30 KHz and 6 KHz with and without the substrate undercut, respectively.

6.2.2 Active silicon photonic circuits

In Chapter 4, we present several 200 Gb/s and 400 Gb/s active SiP integrated circuits targeting intra-datacenter optical interconnects. Summary of the designs and experimental results are shown below.

- First, we present the design and experimental demonstration of a SiP MZM based four lane 400 Gb/s for PSM based intra-datacenter optical interconnects. We report the device details, small-signal, and large-signal characterization of the transmitter. The measured EO bandwidth and RF V_π of the MZMs are approximately 30 GHz and 6 V, respectively. Also, we show the EO crosstalk between the four MZMs, and conclude that more than 750 μm spacing is needed for parallel operation. For large-signal modulation, we characterize the performance of the transmitter versus several parameters. Using only a 5-tap receiver FFE, 53 Gbaud PAM4 per lane can be received at a BER below the KP4-FEC threshold without crosstalk from the other MZMs. Moreover, we show that the MZMs can be driven with a driving voltage swing below 1.8 Vpp and still achieve a BER below the KP4-FEC threshold for a 53 Gbaud PAM4 signal. Although, several 100 Gb/s demonstrations have been published to date based on SiP MZMs, we believe this is the best result for a MZM with a lateral PN junction in terms of driving voltage swing and equalization complexity to the best of our knowledge. Moreover, we demonstrate the first demonstration of a simultaneous modulation of a 4-lane transmitter running at an aggregate rate of 400 Gb/s with an average BER of approximately 1×10^{-4} for all lanes.

- Next, we present the design of a 200 Gb/s SiP transmitter using two MEMZMs for intra-datacenter optical interconnects. The MEMZMs have a V_π and EO bandwidth of 5 V and 38 GHz, respectively. Results reveal that up to 128 Gb/s per lane can be achieved using less than 2 Vpp and 1 Vpp voltage swings and 11-tap FFE at a BER below the KP4-FEC threshold. To the best of our knowledge, this presents the lowest drive voltage and number of FFE taps using a MEMZM delivering more than 100 Gb/s reported up to date. Moreover, we drive all segments simultaneously and assess the inter-MZM crosstalk. We observe a degradation in the BER performance due to the EO crosstalk, however, we can still operate at 200 Gb/s net rate over as much as 10 km at a BER below the KP4-FEC threshold using a relatively low voltage swing of 2.8 Vpp on segment 1 and 1.4 Vpp on segment 2, and 11-tap FFE at the receiver. Hence, the demonstrated transmitter presents a potential design for next generation

200 Gb/s intra-datacenter transceivers.

- Finally, we exploit the other polarization where we experimentally demonstrate a dual-polarization O-band SiP transmitter for intra-datacenter optical interconnects. The transmitter has an average $V_{\pi}L$ and a bandwidth at 1.5 V reverse bias voltage of 2.88 V.cm and 24.5 GHz, respectively. We test the transmitter for DP-PAM2 and DP-PAM4 formats using a DD-SVR versus various parameters. Results reveal that 112 Gb/s DP-PAM2 can be transmitted over as much as 10 km of SMF at a BER below 10^{-5} at -1 dBm received signal power and random SOP. Also, 168 Gb/s (42 Gbaud) DP-PAM4 signal can be transmitted over 2 km and 10 km at a BER below the HD-FEC at 0 dBm and 2 dBm, respectively. In addition, 224 Gb/s and 200 Gb/s DP-PAM4 is successfully received at a BER below the 7% HD-FEC in the B2B and 2 km cases, respectively. Finally, we explain the superior performance of the 6×2 MIMO compared to the 4×2 in the presence of SVR imperfections.

6.2.3 System-level demonstrations

Finally, we present two system-level demonstrations using PAM4 modulations format in Chapter 5.

- First, we demonstrate single polarization PAM4 in the O-band, where we study the BER performance versus bit rate, number of receiver equalizer taps, received signal power, and reach. Results reveal that we can achieve up to 168 Gb/s PAM4 transmission over a 10 km reach below the 2×10^{-4} FEC threshold. This result demonstrates a 10 times improvement in the bit-rate-reach product while maintaining a performance below the 2×10^{-4} FEC threshold compared to the results in [130]. Also, we demonstrate 176 Gb/s PAM4 over 10 km reach below the 3.8×10^{-3} FEC threshold. At the time of the experiment, these results are the highest bit rates reported for O-band, single channel and single polarization PAM4 transmission over 10 km of SMF with direct detection applicable in data-center communications. In addition, we explore the BER dependence on the reach for an 84 and 88 Gbaud PAM4 signal at both constant launch power and constant received power. We demonstrate that residual chromatic dispersion present at 1325 nm at a symbol rate as high as 88 Gbaud has no impact on the signal performance after as much as 10 km of SMF.

- Then, we present the first demonstration of 400 Gb/s ($4\lambda\times$ 100 Gb/s) CWDM-TOSA targeting 400G-FR4 requirements. We present a detailed system-level study of the CWDM-TOSA versus several parameters. Four 53 Gbaud PAM4 RF signals are used to drive the TOSA achieving a net rate of 400 Gb/s. Results reveal that 400 Gb/s can be transmitted over up to 2 km of SMF at a BER below the KP4-FEC threshold using only a 5 tap FFE at the receiver at -5 dBm OMA. To the best of our knowledge, this is the first demonstration of 400 Gb/s using a 4λ CWDM TOSA over 2 km of SMF. Also, we show the TOSA is capable of achieving 400 Gb/s over 20 km, and 600 Gb/s over 10 km below the KP4- and HD-FEC thresholds, respectively, without optical amplification. Furthermore, we show the performance of the TOSA against case temperature, where it shows no significant change in the BER performance from 20°C to 60°C. Finally, we compare the performance of PAM2, PAM4, and PAM8 modulation formats where we show the possibility of achieving a higher bit rate using PAM8 modulation format at the expense of utilizing a stronger FEC.

6.3 Future Work

In this thesis, we presented several devices and circuits for optical DCI. We believe that some opportunities for future research exist that are derived from the work presented in this thesis. Below, we list some of the prospective research avenues in the short term and long term.

6.3.1 Short term research

In the short term, we believe the following projects can have a good impact since we already started exploring them and obtained promising results.

RF and optical packaging:

In this thesis, we presented several SiP designs where all the testing was done on the die level, and optical and RF probing is needed. Only DC wirebonding to a chip carrier was used to facilitate the testing. On the other hand, vibrations in the fiber array and RF probes can affect the experimental results. Hence, the next logical step is to fully package the PIC and repeat the testing on a packaged module which will increase the maturity level of the device under test and get closer to a reliable design.

Testing of modified designs:

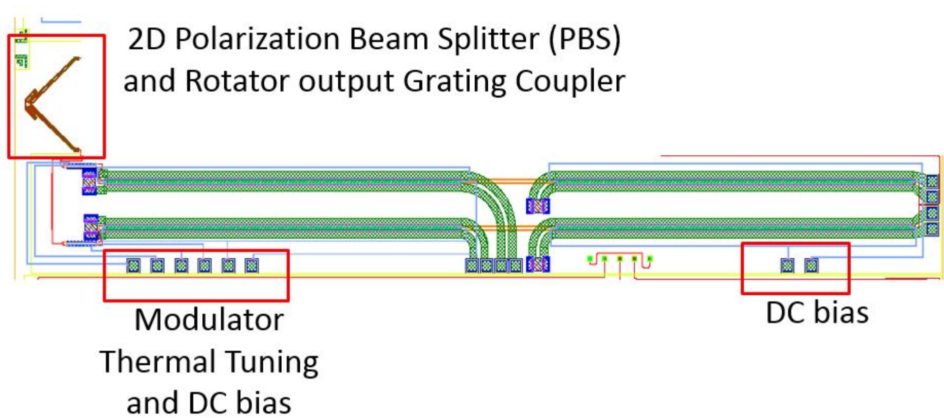

Figure 6.2. Dual Polarization DAC-less PAM4 transmitter

We presented in Chapter 4 few active circuits for intra-data center optical interconnects. For example, the DP-PAM4 is driven by two DACs generating a PAM4 signal each. We propose the design shown in Fig. 6.2 which leverages the usage of two segmented TWMZMs and 2D grating for polarization multiplexing. Compared to the design in Chapter 4, this design can be driven by OOK signals to generate the PAM4 signal which simplifies the driver circuitry. Moreover, it has larger bandwidth due to the segmented electrodes and polarization multiplexing is done on chip.

6.3.2 Long term research

Next, we present other research avenues that can be approached but will require more than a year to reach preliminary results.

Co-design of the driver and transmitters:

In the entire thesis, we focused on the SiP PIC design only. However, designing the CMOS driver can give us an extra degree of flexibility to achieve superior performance. For example, segmented TWMZMs are considered as good choice in the bandwidth and driving voltage trade off. However, a proper design for a distributed driver including voltage swing and delay is needed. Hence, co-design for such driver along a MEMZM design will achieve the best performance for the transmitter module.

Design of SiGe avalanche PDs:

Waveguide coupled PDs using epitaxial grown germanium is one of the advantages of the SiP platform due to their good performance and low cost. Although the SiP platform is relatively low loss, the loss budget is more challenging compared to InP and PLC platforms. Hence, developing avalanche PDs with sufficient gain can relax the IL budget for the SiP transceivers. Moreover, the silicon material has very low excess noise factor which is essential to achieve an APD with high gain. Few APD designs are reported on the SiGe platform, however, we believe much more optimization is needed especially for high speed transceivers operating beyond 100 Gb/s. We believe that a large design space for the silicon and germanium layers, junction orientation, doping, and other factors, exists and optimization will be required to tackle such design.

References

[1] "Cisco Global Cloud Index: Forecast and Methodology, 2016-2021," *White Paper-c11-738085, 2016.* [Online]. Available: *https://www.cisco.com/c/en/us/solutions/collateral/service-provider/global-cloud-index-gci/white-paper-c11-738085.pdf*.

[2] "IEEE Standard for Ethernet," *IEEE Std 802.3-2015.*

[3] "100GLambda MSA," *2018.* [Online]. Available: *http://100glambda.com.*

[4] M. Chagnon, M. Morsy-Osman, M. Poulin, C. Paquet, S. Lessard, and D. V. Plant, "Experimental parametric study of a silicon photonic modulator enabled 112-Gb/s PAM transmission system with a DAC and ADC," *Journal of Lightwave Technology*, vol. 33, no. 7, pp. 1380–1387, 2015.

[5] M. Morsy-Osman, M. Chagnon, M. Poulin, S. Lessard, and D. V. Plant, "224-Gb/s 10-km transmission of PDM PAM-4 at 1.3 μm using a single intensity-modulated laser and a direct-detection MIMO DSP-based receiver," *Journal of Lightwave Technology*, vol. 33, no. 7, pp. 1417–1424, 2015.

[6] A. Dochhan, H. Griesser, N. Eiselt, M. H. Eiselt, and J.-P. Elbers, "Solutions for 80 km DWDM systems," *Journal of Lightwave Technology*, vol. 34, no. 2, pp. 491–499, 2016.

[7] Y. Kai, M. Nishihara, T. Tanaka, T. Takahara, L. Li, Z. Tao, B. Liu, J. C. Rasmussen, and T. Drenski, "Experimental comparison of pulse amplitude modulation (PAM)

and discrete multi-tone (DMT) for short-reach 400-Gbps data communication," in *Proc. European Conference on Optical Communication (ECOC)*, Sept 2013, pp. 1–3.

[8] "IEEE Standard for Ethernet - Amendment 10: Media access control parameters, physical layers, and management parameters for 200 Gb/s and 400 Gb/s operation," pp. 1–372, 2017.

[9] "Ethernet alliance roadmap," *http://www.ethernetalliance.org/roadmap*.

[10] D. Che, A. Li, X. Chen, Q. Hu, Y. Wang, and W. Shieh, "160-Gb/s stokes vector direct detection for short reach optical communication," in *Proc. Optical Fiber Communication Conference (OFC): Postdeadline Papers*, 2014, p. Th5C.7.

[11] D. Ce, A. Li, X. Chen, Q. Hu, Y. Wang, and W. Shieh, "Stokes vector direct detection for short-reach optical communication," *Optics Letters*, vol. 39, no. 11, pp. 3110–3113, 2014.

[12] M. Morsy-Osman, M. Chagnon, M. Poulin, S. Lessard, and D. Plant, "1$\lambda\times$ 224 Gb/s 10 km transmission of polarization division multiplexed PAM-4 signals using 1.3 μm SiP intensity modulator and a direct-detection MIMO-based receiver," in *Proc. European Conference on Optical Communication (ECOC)*, 2014, pp. 1–3.

[13] L. Zhang, Q. Zhang, T. Zuo, E. Zhou, G. N. Liu, and X. Xu, "C-band single wavelength 100-Gb/s IM-DD transmission over 80-km SMF without CD compensation using SSB-DMT," in *Proc. Optical Fiber Communication Conference (OFC)*, 2015, p. Th4A.2.

[14] M. Y. S. Sowailem, T. M. Hoang, M. Morsy-Osman, M. Chagnon, M. Qiu, S. Paquet, C. Paquet, I. Woods, O. Liboiron-Ladouceur, and D. V. Plant, "Impact of chromatic dispersion compensation in single carrier two-dimensional stokes vector direct detection system," *IEEE Photonics Journal*, vol. 9, no. 4, pp. 1–10, 2017.

[15] X. Chen, C. Antonelli, S. Chandrasekhar, G. Raybon, J. Sinsky, A. Mecozzi, M. Shtaif, and P. Winzer, “218-Gb/s single-wavelength, single-polarization, single-photodiode transmission over 125-km of standard singlemode fiber using Kramers-Kronig detection,” in *Proc. Optical Fiber Communication Conference (OFC)*, March 2017, pp. 1–3.

[16] R. Rath, D. Clausen, S. Ohlendorf, S. Pachnicke, and W. Rosenkranz, “Tomlinson–harashima precoding for dispersion uncompensated pam-4 transmission with direct-detection,” *Journal of Lightwave Technology*, vol. 35, no. 18, pp. 3909–3917, 2017.

[17] Optical Internetworking Forum, https://www.oiforum.com/.

[18] What Is 400ZR and Why Is It Important?, https://www.neophotonics.com/what-is-400-zr/.

[19] M. Jacques, A. Samani, D. Patel, E. El-Fiky, M. Morsy-Osman, T. Hoang, M. G. Saber, L. Xu, J. Sonkoly, M. Ayliffe, and D. V. Plant, “Modulator material impact on chirp, DSP, and performance in coherent digital links: comparison of the lithium niobate, indium phosphide, and silicon platforms,” *Optics Express*, vol. 26, no. 17, pp. 22 471–22 490, 2018.

[20] T. Baehr-Jones, T. Pinguet, P. L. Guo-Qiang, S. Danziger, D. Prather, and M. Hochberg, “Myths and rumours of silicon photonics,” *Nature Photonics*, vol. 6, no. 4, p. 206, 2012.

[21] L. B. Soldano and E. C. Pennings, “Optical multi-mode interference devices based on self-imaging: principles and applications,” *Journal of lightwave technology*, vol. 13, no. 4, pp. 615–627, 1995.

[22] P. Dumais, Y. Wei, M. Li, F. Zhao, X. Tu, J. Jiang, D. Celo, D. Goodwill, H. Fu, D. Geng, and E. Bernier, “2×2 multimode interference coupler with low loss using

248 nm photolithography," in *Proc. Optical Fiber Communication Conference (OFC)*, 2016.

[23] J. Wang, D. Liang, Y. Tang, D. Dai, and J. E. Bowers, "Realization of an ultra-short silicon polarization beam splitter with an asymmetrical bent directional coupler," *Optics letters*, vol. 38, no. 1, pp. 4–6, 2013.

[24] T. Liang and H. Tsang, "Integrated polarization beam splitter in high index contrast silicon-on-insulator waveguides," *IEEE photonics Technology Letters*, vol. 17, no. 2, pp. 393–395, 2005.

[25] D. Patel, S. Ghosh, M. Chagnon, A. Samani, V. Veerasubramanian, M. Osman, and D. V. Plant, "Design, analysis, and transmission system performance of a 41 GHz silicon photonic modulator," *Optics Express*, vol. 23, no. 11, pp. 14 263–14 287, 2015.

[26] A. Samani, M. Chagnon, D. Patel, V. Veerasubramanian, S. Ghosh, M. Osman, Q. Zhong, and D. V. Plant, "A low-voltage 35-GHz silicon photonic modulator-enabled 112-Gb/s transmission system," *IEEE Photonics Journal*, vol. 7, no. 3, pp. 1–13, 2015.

[27] J. S. Orcutt, D. M. Gill, J. Proesel, J. Ellis-Monaghan, F. Horst, T. Barwicz, C. Xiong, F. G. Anderson, A. Agrawal, Y. Martin, C. W. Baks, M. Khater, J. C. Rosenberg, W. D. Sacher, J. Hofrichter, E. Kiewra, A. D. Stricker, F. Libsch, B. Offrein, M. Meghelli, N. B. Feilchenfeld, W. Haensch, and W. M. J. Green, "Monolithic silicon photonics at 25 Gb/s," in *Proc. Optical Fiber Communication Conference (OFC)*, 2016, pp. 1–3.

[28] C. R. Doerr, L. Chen, D. Vermeulen, T. Nielsen, S. Azemati, S. Stulz, G. McBrien, X.-M. Xu, B. Mikkelsen, M. Givehchi, C. Rasmussen, and S. Y. Park, "Single-chip silicon photonics 100-Gb/s coherent transceiver," in *Proc. Optical Fiber Communication Conference (OFC): Postdeadline Papers*, 2014.

[29] P. Dong, C. Xie, and L. L. Buhl, "Monolithic polarization diversity coherent receiver based on 120-degree optical hybrids on silicon," *Optics Express*, vol. 22, no. 2, pp. 2119–2125, 2014.

[30] E. El-Fiky, Y. D'Mello, Y. Wang, J. Skoric, M. G. Saber, A. Kumar, A. Samani, L. Xu, R. Li, D. Patel, and D. V. Plant, "Ultra-broadband and compact asymmetrical beam splitter enabled by angled sub-wavelength grating MMI," in *Proc. Conference on Lasers and Electro-Optics (CLEO)*, 2018, p. STh4A.7.

[31] E. El-Fiky, A. Samani, D. Patel, and D. V. Plant, "A high extinction ratio, broadband, and compact polarization beam splitter enabled by cascaded MMIs on silicon-on-insulator," in *Proc. Optical Fiber Communication Conference (OFC)*, 2016, p. W2A.8.

[32] E. El-Fiky, Y. Wang, S. Bernal, C. Gamache, E. Panorel, A. Kumar, A. Samani, M. Jacques, P. Koh, and D. V. Plant, "High extinction ratio and broadband o-band polarization splitter and rotator on silicon-on-insulator," in *Proc. Optical Fiber Communications Conference and Exhibition (OFC)*, 2019, pp. 1–3.

[33] E. El-Fiky, A. Samani, M. S. Alam, M. Sowailem, O. Carpentier, M. Jacques, L. Guenin, D. Patel, and D. V. Plant, "A 4-lane 400 Gb/s silicon photonic transceiver for intra-datacenter optical interconnects," in *Proc. Optical Fiber Communications Conference and Exhibition (OFC)*, 2019.

[34] E. El-Fiky, A. Samani, D. Patel, M. Jacques, M. Sowailem, and D. V. Plant, "400 Gb/s O-band silicon photonic transmitter for intra-datacenter optical interconnects," *Optics Express*, vol. 27, no. 7, pp. 10 258–10 268, 2019.

[35] E. El-Fiky, A. Samani, M. Sowailem, M. Osman, M. Jacques, D. Patel, M. G. Saber, L. Xu, Z. Xing, M. Xiang, and D. V. Plant, "Dual parallel multielectrode traveling

wave Mach–Zehnder modulator for 200 Gb/s intra-datacenter optical interconnects," *IEEE Photonics Journal*, vol. 11, no. 1, pp. 1–9, 2019.

[36] E. El-Fiky, M. Sowailem, A. Samani, M. Osman, D. Patel, M. Chagnon, and D. V. Plant, "Dual polarization O-band silicon photonic intensity modulator for stokes vector direct detection systems," in *Proc. Optical Fiber Communications Conference and Exhibition (OFC)*, 2017, p. Tu2H.5.

[37] E. El-Fiky, M. Osman, M. Sowailem, A. Samani, D. Patel, R. Li, M. G. Saber, Y. Wang, N. Abadia, Y. D'Mello, and D. V. Plant, "200 Gb/s transmission using a dual-polarization O-band silicon photonic intensity modulator for stokes vector direct detection applications," *Optics Express*, vol. 25, no. 24, pp. 30 336–30 348, 2017.

[38] E. El-Fiky, M. Chagnon, M. Sowailem, A. Samani, M. Morsy-Osman, and D. V. Plant, "168 Gb/s single carrier PAM4 transmission for intra data center optical interconnects," *IEEE Photonics Technology Letters*, 2017.

[39] E. El-Fiky, M. Osman, A. Samani, C. Gamache, M. H. Ayliffe, J. Li, M. Jacques, Y. Wang, A. Kumar, and D. V. Plant, "First demonstration of a 400 Gb/s 4λ CWDM TOSA for datacenter optical interconnects," *Optics Express*, vol. 26, no. 16, pp. 19 742–19 749, 2018.

[40] A. Novack, Y. Liu, R. Ding, M. Gould, T. Baehr-Jones, Q. Li, Y. Yang, Y. Ma, Y. Zhang, K. Padmaraju, K. Bergmen, A. E. Lim, G. Lo, and M. Hochberg, "A 30 GHz silicon photonic platform," in *Proc. IEEE International Conference on Group IV Photonics (GFP)*, 2013, pp. 7–8.

[41] L. Chrostowski and M. Hochberg, *Silicon photonics design: from devices to systems*. Cambridge University Press, 2015.

[42] C. Doerr and L. Chen, "Silicon photonics in optical coherent systems," *Proceedings of the IEEE*, vol. 106, no. 12, pp. 2291–2301, 2018.

[43] M. Lee and P. M. Fauchet, "Two-dimensional silicon photonic crystal based biosensing platform for protein detection," *Optics Express*, vol. 15, no. 8, pp. 4530–4535, 2007.

[44] J. Leuthold, C. Koos, and W. Freude, "Nonlinear silicon photonics," *Nature photonics*, vol. 4, no. 8, p. 535, 2010.

[45] C. V. Poulton, A. Yaacobi, D. B. Cole, M. J. Byrd, M. Raval, D. Vermeulen, and M. R. Watts, "Coherent solid-state LIDAR with silicon photonic optical phased arrays," *Optics letters*, vol. 42, no. 20, pp. 4091–4094, 2017.

[46] S. Srinivasan, R. Moreira, D. Blumenthal, and J. E. Bowers, "Design of integrated hybrid silicon waveguide optical gyroscope," *Optics Express*, vol. 22, no. 21, pp. 24 988–24 993, 2014.

[47] W. Zhang and J. Yao, "Silicon-based integrated microwave photonics," *IEEE Journal of Quantum Electronics*, vol. 52, no. 1, pp. 1–12, 2016.

[48] R. E. Camacho-Aguilera, Y. Cai, N. Patel, J. T. Bessette, M. Romagnoli, L. C. Kimerling, and J. Michel, "An electrically pumped germanium laser," *Optics Express*, vol. 20, no. 10, pp. 11 316–11 320, 2012.

[49] J. Liu, X. Sun, D. Pan, X. Wang, L. C. Kimerling, T. L. Koch, and J. Michel, "Tensile-strained, n-type Ge as a gain medium for monolithic laser integration on Si," *Optics Express*, vol. 15, no. 18, pp. 11 272–11 277, 2007.

[50] M. J. Süess, R. Geiger, R. Minamisawa, G. Schiefler, J. Frigerio, D. Chrastina, G. Isella, R. Spolenak, J. Faist, and H. Sigg, "Analysis of enhanced light emission from highly strained germanium microbridges," *Nature Photonics*, vol. 7, no. 6, p. 466, 2013.

[51] S. Keyvaninia, M. Muneeb, S. Stanković, P. J. V. Veldhoven, D. V. Thourhout, and G. Roelkens, "Ultra-thin DVS-BCB adhesive bonding of III-V wafers, dies and multiple dies to a patterned silicon-on-insulator substrate," *Optical Material Express*, vol. 3, no. 1, pp. 35–46, 2013.

[52] J. E. Bowers, J. T. Bovington, A. Y. Liu, and A. C. Gossard, "A path to 300 mm hybrid silicon photonic integrated circuits," in *Proc. Optical Fiber Communications Conference and Exhibition (OFC)*, March 2014, pp. 1–3.

[53] J. . Fedeli, L. Liu, L. Grenouillet, D. Bordel, F. Mandorlo, N. Olivier, T. Spuesens, P. Régreny, P. Grosse, P. Rojo-Romeo, R. Orobtchouk, and D. Van Thourhout, "Towards optical networks-on-chip with 200mm hybrid technology," in *Proc. Optical Fiber Communications Conference and Exhibition (OFC)*, 2011, pp. 1–3.

[54] S. Uvin, S. Kumari, A. De Groote, S. Verstuyft, G. Lepage, P. Verheyen, J. Van Campenhout, G. Morthier, D. Van Thourhout, and G. Roelkens, "1.3 μm InAs/GaAs quantum dot DFB laser integrated on a Si waveguide circuit by means of adhesive die-to-wafer bonding," *Optics Express*, vol. 26, no. 14, pp. 18 302–18 309, 2018.

[55] Y. Zhang, S. Yang, X. Zhu, Q. Li, H. Guan, P. Magill, K. Bergman, T. Baehr-Jones, and M. Hochberg, "Quantum dot SOA/silicon external cavity multi-wavelength laser," *Optics Express*, vol. 23, no. 4, pp. 4666–4671, 2015.

[56] G. Roelkens, L. Liu, D. Liang, R. Jones, A. Fang, B. Koch, and J. Bowers, "III-V/silicon photonics for on-chip and intra-chip optical interconnects," *Laser & Photonics Reviews*, vol. 4, no. 6, pp. 751–779, 2010.

[57] M. J. Heck, M. L. Davenport, S. Srinivasan, J. Hulme, and J. E. Bowers, "Optimization of the hybrid silicon photonic integrated circuit platform," in *Novel In-Plane Semiconductor Lasers XII*, vol. 8640, 2013, p. 86400U.

[58] B. R. Koch, E. J. Norberg, B. Kim, J. Hutchinson, J.-H. Shin, G. Fish, and A. Fang, "Integrated silicon photonic laser sources for telecom and datacom," in *Proc. Optical Fiber Communication Conference (OFC)*, 2013, p. PDP5C.8.

[59] L. Liu, T. Spuesens, D. Van Thourhout, G. Morthier, L. Grenouillet, N. Olivier, J. Fedeli, P. Rojo-Romeo, P. Régreny, F. Mandorlo, and R. Orobtchouk, "200mm wafer scale iii-v/soi technology for all-optical network-on-chip and signal processing," in *IEEE International Conference on Group IV Photonics*, 2010, pp. 7–9.

[60] T. Creazzo, E. Marchena, S. B. Krasulick, P. K. L. Yu, D. V. Orden, J. Y. Spann, C. C. Blivin, L. He, H. Cai, J. M. Dallesasse, R. J. Stone, and A. Mizrahi, "Integrated tunable cmos laser," *Optics Express*, vol. 21, no. 23, pp. 28 048–28 053, 2013.

[61] S. Tanaka, S.-H. Jeong, S. Sekiguchi, T. Kurahashi, Y. Tanaka, and K. Morito, "High-output-power, single-wavelength silicon hybrid laser using precise flip-chip bonding technology," *Optics Express*, vol. 20, no. 27, pp. 28 057–28 069, 2012.

[62] T. Shimizu, M. Okano, H. Takahashi, N. Hatori, M. Ishizaka, T. Yamamoto, M. Mori, T. Horikawa, Y. Urino, T. Nakamura *et al.*, "Multi-channel and high-density hybrid integrated light source by thermal management for low power consumption for ultra-high bandwidth optical interconnection," in *Proc. International Conference on Electronics Packaging (ICEP)*, 2014, pp. 684–688.

[63] N. Hatori, T. Shimizu, M. Okano, M. Ishizaka, T. Yamamoto, Y. Urino, M. Mori, T. Nakamura, and Y. Arakawa, "A novel spot size convertor for hybrid integrated light sources on photonics-electronics convergence system," in *Proc. IEEE International Conference on Group IV Photonics (GFP)*, 2012, pp. 171–173.

[64] T. Chu, N. Fujioka, and M. Ishizaka, "Compact, lower-power-consumption wavelength tunable laser fabricated with silicon photonic wire waveguide micro-ring resonators," *Optics Express*, vol. 17, no. 16, pp. 14 063–14 068, 2009.

[65] A. Zilkie, P. Seddighian, B. Bijlani, W. Qian, D. Lee, S. Fathololoumi, J. Fong, R. Shafiiha, D. Feng, B. Luff *et al.*, “Power-efficient III-V/Silicon external cavity DBR lasers,” *Optics Express*, vol. 20, no. 21, pp. 23 456–23 462, 2012.

[66] P. De Dobbelaere, A. Ayazi, Y. Chi, A. Dahl, S. Denton, S. Gloeckner, K. Hon, S. Hovey, Y. Liang, M. Mack, G. Masini, A. Mekis, M. Peterson, T. Pinguet, J. Schramm, M. Sharp, C. Sohn, K. Stechschulte, P. Sun, G. Vastola, L. Verslegers, and R. Zhou, “Packaging of silicon photonics systems,” in *Proc. Optical Fiber Communications Conference and Exhibition (OFC)*, 2014.

[67] A. E. Lim, J. Song, Q. Fang, C. Li, X. Tu, N. Duan, K. K. Chen, R. P. Tern, and T. Liow, “Review of silicon photonics foundry efforts,” *IEEE Journal of Selected Topics in Quantum Electronics*, vol. 20, no. 4, pp. 405–416, 2014.

[68] G. T. Reed, G. Mashanovich, F. Gardes, and D. Thomson, “Silicon optical modulators,” *Nature photonics*, vol. 4, no. 8, p. 518, 2010.

[69] R. Soref and B. Bennett, “Electrooptical effects in silicon,” *IEEE Journal of Quantum Electronics*, vol. 23, no. 1, pp. 123–129, 1987.

[70] M. Nedeljkovic, R. Soref, and G. Z. Mashanovich, “Free-carrier electrorefraction and electroabsorption modulation predictions for silicon over the 1–14- μm infrared wavelength range,” *IEEE Photonics Journal*, vol. 3, no. 6, pp. 1171–1180, 2011.

[71] S. Liao, N.-N. Feng, D. Feng, P. Dong, R. Shafiiha, C.-C. Kung, H. Liang, W. Qian, Y. Liu, J. Fong, J. E. Cunningham, Y. Luo, and M. Asghari, “36 GHz submicron silicon waveguide germanium photodetector,” *Optics Express*, vol. 19, no. 11, pp. 10 967–10 972, May 2011.

[72] A. Novack, M. Gould, Y. Yang, Z. Xuan, M. Streshinsky, Y. Liu, G. Capellini, A. E.-J. Lim, G.-Q. Lo, T. Baehr-Jones, and M. Hochberg, “Germanium photodetector with

60 GHz bandwidth using inductive gain peaking," *Optics Express*, vol. 21, no. 23, pp. 28 387–28 393, 2013.

[73] T. Liow, K. Ang, Q. Fang, J. Song, Y. Xiong, M. Yu, G. Lo, and D. Kwong, "Silicon modulators and germanium photodetectors on SOI: Monolithic integration, compatibility, and performance optimization," *IEEE Journal of Selected Topics in Quantum Electronics*, vol. 16, no. 1, pp. 307–315, 2010.

[74] H. Chen, P. Verheyen, P. D. Heyn, G. Lepage, J. D. Coster, S. Balakrishnan, P. Absil, W. Yao, L. Shen, G. Roelkens, and J. V. Campenhout, "-1 v bias 67 GHz bandwidth Si-contacted germanium waveguide p-i-n photodetector for optical links at 56 Gbps and beyond," *Optics Express*, vol. 24, no. 5, pp. 4622–4631, 2016.

[75] M. Yang, W. M. Green, S. Assefa, J. Van Campenhout, B. G. Lee, C. V. Jahnes, F. E. Doany, C. L. Schow, J. A. Kash, and Y. A. Vlasov, "Non-blocking 4x4 electro-optic silicon switch for on-chip photonic networks," *Optics Express*, vol. 19, no. 1, pp. 47–54, 2011.

[76] Y. Wang, L. Xu, H. Yun, M. Ma, A. Kumar, E. El-Fiky, R. Li, N. Abadíacalvo, L. Chrostowski, N. A. Jaeger *et al.*, "Polarization-independent mode-evolution-based coupler for the silicon-on-insulator platform," *IEEE Photonics Journal*, vol. 10, no. 3, pp. 1–10, 2018.

[77] Y. Zhang, S. Yang, A. E.-J. Lim, G.-Q. Lo, C. Galland, T. Baehr-Jones, and M. Hochberg, "A compact and low loss Y-junction for submicron silicon waveguide," *Optics Express*, vol. 21, no. 1, pp. 1310–1316, 2013.

[78] R. Halir, I. Molina-Fernandez, A. Ortega-Monux, J. G. Wanguemert-Perez, D. Xu, P. Cheben, and S. Janz, "A design procedure for high-performance, rib-waveguide-based multimode interference couplers in silicon-on-insulator," *Journal of Lightwave Technology*, vol. 26, no. 16, pp. 2928–2936, 2008.

[79] W. Bogaerts, P. De Heyn, T. Van Vaerenbergh, K. De Vos, S. Kumar Selvaraja, T. Claes, P. Dumon, P. Bienstman, D. Van Thourhout, and R. Baets, "Silicon microring resonators," *Laser & Photonics Reviews*, vol. 6, no. 1, pp. 47–73, 2012.

[80] F. Horst, W. M. Green, S. Assefa, S. M. Shank, Y. A. Vlasov, and B. J. Offrein, "Cascaded Mach-Zehnder wavelength filters in silicon photonics for low loss and flat pass-band WDM (de-)multiplexing," *Optics Express*, vol. 21, no. 10, pp. 11 652–11 658, 2013.

[81] F. Fresi, P. Velha, G. Meloni, A. Malacarne, V. Sorianello, M. Midrio, V. Toccafondo, S. Faralli, M. Romagnoli, and L. Poti, "Silicon photonics integrated 16-QAM modulator exploiting only binary driving electronics," *Proc. Optical Fiber Communications Conference and Exhibition (OFC)*, pp. 1–3, 2016.

[82] J. Xing, K. Xiong, H. Xu, Z. Li, X. Xiao, J. Yu, and Y. Yu, "Silicon-on-insulator-based adiabatic splitter with simultaneous tapering of velocity and coupling," *Optics Letters*, vol. 38, no. 13, pp. 2221–2223, 2013.

[83] J. D. Doménech, J. S. Fandiño, B. Gargallo, and P. Muñoz, "Arbitrary coupling ratio multimode interference couplers in silicon-on-insulator," *Journal of Lightwave Technology*, vol. 32, no. 14, pp. 2536–2543, 2014.

[84] A. Zanzi, A. Brimont, A. Griol, P. Sanchis, and J. Marti, "Compact and low-loss asymmetrical multimode interference splitter for power monitoring applications," *Optics Letters*, vol. 41, no. 2, pp. 227–229, 2016.

[85] H. Robert, B. P. J., C. Pavel, O.-M. Alejandro, A.-R. Carlos, S. J. H., L. Jean, X. Dan-Xia, W.-P. J. Gonzalo, M.-F. Íñigo, and J. Siegfried, "Waveguide sub-wavelength structures: a review of principles and applications," *Laser & Photonics Reviews*, vol. 9, no. 1, pp. 25–49.

[86] P. Cheben, J. H. Schmid, S. Wang, D.-X. Xu, M. Vachon, S. Janz, J. Lapointe, Y. Painchaud, and M.-J. Picard, "Broadband polarization independent nanophotonic coupler for silicon waveguides with ultra-high efficiency," *Optics Express*, vol. 23, no. 17, pp. 22 553–22 563, 2015.

[87] Y. Wang, L. Xu, A. Kumar, Y. D'Mello, D. Patel, Z. Xing, R. Li, M. G. Saber, E. El-Fiky, and D. V. Plant, "Compact single-etched sub-wavelength grating couplers for o-band application," *Optics Express*, vol. 25, no. 24, pp. 30 582–30 590, 2017.

[88] L. Chen, C. R. Doerr, and Y.-K. Chen, "Compact polarization rotator on silicon for polarization-diversified circuits," *Optics letters*, vol. 36, no. 4, pp. 469–471, 2011.

[89] D. Dai, Z. Wang, J. Peters, and J. E. Bowers, "Compact polarization beam splitter using an asymmetrical Mach–Zehnder interferometer based on silicon-on-insulator waveguides," *IEEE Photonics Technology Letters*, vol. 24, no. 8, pp. 673–675, 2012.

[90] D. Dai and J. E. Bowers, "Novel ultra-short and ultra-broadband polarization beam splitter based on a bent directional coupler," *Optics Express*, vol. 19, no. 19, pp. 18 614–18 620, 2011.

[91] Y. Huang, Z. Tu, H. Yi, Y. Li, X. Wang, and W. Hu, "High extinction ratio polarization beam splitter with multimode interference coupler on SOI," *Optics Communications*, vol. 307, pp. 46–49, 2013.

[92] W. Yang, Y. Xu, Y. Li, X. Wang, and Z. Wang, "A compact and wide-band polarization beam splitter based on wedge-shaped MMI coupler in silicon-on-insulator," in *Proc. Optical Fiber Communication Conference (OFC)*, 2015, pp. W2A–12.

[93] Y. Jiao, D. Dai, Y. Shi, and S. He, "Shortened polarization beam splitters with two cascaded multimode interference sections," *IEEE Photonics Technology Letters*, vol. 21, no. 20, pp. 1538–1540, 2009.

[94] L. Han, S. Liang, H. Zhu, C. Zhang, and W. Wang, "A high extinction ratio polarization beam splitter with MMI couplers on InP substrate," *IEEE Photonics Technology Letters*, vol. 27, no. 7, pp. 782–785, 2015.

[95] R. J. Bojko, J. Li, L. He, T. Baehr-Jones, M. Hochberg, and Y. Aida, "Electron beam lithography writing strategies for low loss, high confinement silicon optical waveguides," *Journal of Vacuum Science & Technology B, Nanotechnology and Microelectronics: Materials, Processing, Measurement, and Phenomena*, vol. 29, no. 6, p. 06F309, 2011.

[96] S. P. Anderson and M. Webster, "Silicon photonic dual-polarization nanotaper for chip-to-fiber coupling," in *Proc. Optical Fiber Communications Conference and Exhibition (OFC)*, 2015, pp. 1–3.

[97] H. Guan, A. Novack, M. Streshinsky, R. Shi, Y. Liu, Q. Fang, A. E.-J. Lim, G.-Q. Lo, T. Baehr-Jones, and M. Hochberg, "High-efficiency low-crosstalk 1310-nm polarization splitter and rotator," *IEEE Photonics Technology Letters*, vol. 26, no. 9, pp. 925–928, 2014.

[98] K. Tan, Y. Huang, G.-Q. Lo, C. Yu, and C. Lee, "Ultra-broadband fabrication-tolerant polarization splitter and rotator," in *Proc. Optical Fiber Communication Conference (OFC)*, 2017, pp. Th1G–7.

[99] W. D. Sacher, T. Barwicz, B. J. Taylor, and J. K. Poon, "Polarization rotator-splitters in standard active silicon photonics platforms," *Optics Express*, vol. 22, no. 4, pp. 3777–3786, 2014.

[100] A. Martin, J. Luff, D. Feng, and M. Asghari, "Technical challenges for 100gb/s silicon photonics transceivers for data center applications," in *Proc. Optical Fiber Communication Conference (OFC)*, 2016, p. Th1F.1.

[101] C. Marxer, P. Griss, and N. F. de Rooij, "A variable optical attenuator based on silicon micromechanics," *IEEE Photonics Technology Letters*, vol. 11, no. 2, pp. 233–235, Feb 1999.

[102] K. N. Nguyen, J. M. Garcia, E. Lively, H. N. Poulsen, D. M. Baney, and D. J. Blumenthal, "Monolithically integrated dual-quadrature coherent receiver on InP with 30 nm tunable SG-DBR local oscillator," in *Proc. European Conference and Exhibition on Optical Communication (ECOC)*, 2011, pp. 1–3.

[103] P. Runge, S. Schubert, A. Seeger, K. Janiak, J. Stephan, D. Trommer, and M. L. Nielsen, "Monolithic InP receiver chip with a variable optical attenuator for colorless WDM detection," *IEEE Photonics Technology Letters*, vol. 26, no. 4, pp. 349–351, 2014.

[104] S. Tsunashima, F. Nakajima, Y. Nasu, R. Kasahara, Y. Nakanishi, T. Saida, T. Yamada, K. Sano, T. Hashimoto, H. Fukuyama, H. Nosaka, and K. Murata, "Silica-based, compact and variable-optical-attenuator integrated coherent receiver with stable optoelectronic coupling system," *Optics Express*, vol. 20, no. 24, pp. 27 174–27 179, 2012.

[105] C. Doerr, L. Chen, D. Vermeulen, T. Nielsen, S. Azemati, S. Stulz, G. McBrien, X. . Xu, B. Mikkelsen, M. Givehchi, C. Rasmussen, and S. . Park.

[106] T. Tsuchizawa, K. Yamada, T. Watanabe, S. Park, H. Nishi, R. Kou, H. Shinojima, and S. Itabashi, "Monolithic integration of silicon-, germanium-, and silica-based optical devices for telecommunications applications," *IEEE Journal of Selected Topics in Quantum Electronics*, vol. 17, no. 3, pp. 516–525, 2011.

[107] S. Chen, Y. Shi, S. He, and D. Dai, "Variable optical attenuator based on a reflective mach–zehnder interferometer," *Optics Communications*, vol. 361, pp. 55–58, 2016.

[108] M. Jacques, A. Samani, E. El-Fiky, D. Patel, Z. Xing, and D. V. Plant, "Optimization of thermo-optic phase-shifter design and mitigation of thermal crosstalk on the SOI platform," *Optics Express*, vol. 27, no. 8, pp. 10 456–10 471, 2019.

[109] R. Ding, Y. Liu, Y. Ma, Y. Yang, Q. Li, A. E. Lim, G. Lo, K. Bergman, T. Baehr-Jones, and M. Hochberg, "High-speed silicon modulator with slow-wave electrodes and fully independent differential drive," *Journal of Lightwave Technology*, vol. 32, no. 12, pp. 2240–2247, 2014.

[110] M. Pantouvaki, S. Srinivasan, Y. Ban, P. De Heyn, P. Verheyen, G. Lepage, H. Chen, J. De Coster, N. Golshani, S. Balakrishnan *et al.*, "Active components for 50 Gb/s NRZ-OOK optical interconnects in a silicon photonics platform," *Journal of Lightwave Technology*, vol. 35, no. 4, pp. 631–638, 2017.

[111] E. El-Fiky, P. De Heyn, M. Osman, A. Srinivasan, A. Samani, M. Pantouvaki, M. Sowailem, J. Van Campenhout, and D. V. Plant, "112 Gb/s PAM4 Transmission over 2 km SMF Using a C-band GeSi electro-absorption modulator," in *Proc. Optical Fiber Communications Conference and Exposition (OFC)*, 2018, p. W2A.16.

[112] R. Dubé-Demers, S. LaRochelle, and W. Shi, "Ultrafast pulse-amplitude modulation with a femtojoule silicon photonic modulator," *Optica*, vol. 3, no. 6, pp. 622–627, 2016.

[113] R. Li, D. Patel, A. Samani, E. El-Fiky, Z. Xing, M. Sowailem, Q. Zhong, and D. V. Plant, "An 80 Gb/s silicon photonic modulator based on the principle of overlapped resonances," *IEEE Photonics Journal*, vol. 9, no. 3, pp. 1–11, 2017.

[114] C. Hössbacher, A. Josten, B. Baeuerle, Y. Fedoryshyn, H. Hettrich, Y. Salamin, W. Heni, C. Haffner, C. Kaiser, R. Schmid *et al.*, "Plasmonic modulator with > 170 GHz bandwidth demonstrated at 100 GBd NRZ," *Optics Express*, vol. 25, no. 3, pp. 1762–1768, 2017.

[115] P. Dong, J. Lee, Y. Chen, L. L. Buhl, S. Chandrasekhar, J. H. Sinsky, and K. Kim, "Four-channel 100-Gb/s per channel discrete multitone modulation using silicon photonic integrated circuits," *Journal of Lightwave Technology*, vol. 34, no. 1, pp. 79–84, 2016.

[116] M. R. Billah, M. Blaicher, J. N. Kemal, T. Hoose, H. Zwickel, P.-I. Dietrich, U. Troppenz, M. Moehrle, F. Merget, A. Hofmann, J. Witzens, S. Randel, W. Freude, and C. Koos, "8-channel 448 Gbit/s silicon photonic transmitter enabled by photonic wire bonding," in *Proc. Optical Fiber Communication Conference (OFC)*, 2017, p. Th5D.6.

[117] L. Jiang, X. Chen, K. Kim, G. de Valicourt, Z. R. Huang, and P. Dong, "Electro-optic crosstalk in parallel silicon photonic mach-zehnder modulators," *Journal of Lightwave Technology*, vol. 36, no. 9, pp. 1713–1720, 2018.

[118] X. Wu, B. Dama, P. Gothoskar, P. Metz, K. Shastri, S. Sunder, J. Van der Spiegel, Y. Wang, M. Webster, and W. Wilson, "A 20Gb/s NRZ/PAM-4 1v transmitter in 40nm CMOS driving a Si-photonic modulator in 0.13 μm CMOS," in *IEEE International Solid-State Circuits Conference (ISSCC)*, 2013, pp. 128–129.

[119] D. Patel, A. Samani, V. Veerasubramanian, S. Ghosh, and D. V. Plant, "Silicon photonic segmented modulator-based electro-optic DAC for 100 Gb/s PAM-4 generation," *IEEE Photonics Technology Letters*, vol. 27, no. 23, pp. 2433–2436, 2015.

[120] A. Shastri, C. Muzio, M. Webster, G. Jeans, P. Metz, S. Sunder, B. Chattin, B. Dama, and K. Shastri, "Ultra-low-power single-polarization QAM-16 generation without DAC using a CMOS photonics based segmented modulator," *Journal of Lightwave Technology*, vol. 33, no. 6, pp. 1255–1260, 2015.

[121] A. Aimone, F. Frey, R. Elschner, I. G. Lopez, G. Fiol, P. Rito, M. Gruner, A. C. Ulusoy, D. Kissinger, J. K. Fischer, C. Schubert, and M. Schell, "DAC-less 32-GBd

PDM-256-QAM using low-power InP IQ segmented MZM," *IEEE Photonics Technology Letters*, vol. 29, no. 2, pp. 221–223, 2017.

[122] A. Samani, D. Patel, M. Chagnon, E. El-Fiky, R. Li, M. Jacques, N. Abadía, V. Veerasubramanian, and D. V. Plant, "Experimental parametric study of 128 Gb/s PAM-4 transmission system using a multi-electrode silicon photonic mach zehnder modulator," *Optics Express*, vol. 25, no. 12, pp. 13 252–13 262, 2017.

[123] A. Samani, V. Veerasubramanian, E. El-Fiky, D. Patel, and D. V. Plant, "A silicon photonic PAM-4 modulator based on dual-parallel Mach–Zehnder interferometers," *IEEE Photonics Journal*, vol. 8, no. 1, pp. 1–10, 2016.

[124] M.-J. Picard, Y. Painchaud, C. Latrasse, C. Larouche, F. Pelletier, and M. Poulin, "Novel spot-size converter for optical fiber to sub-μm silicon waveguide coupling with low loss, low wavelength dependence and high tolerance to alignment," in *Proc. European Conference on Optical Communication (ECOC)*, 2015.

[125] X. Chen, P. Dong, S. Chandrasekhar, K. Kim, B. Li, H. Chen, A. Adamiecki, A. Gnauck, and P. Winzer, "Characterization and digital pre-compensation of electro-optic crosstalk in silicon photonics I/Q modulators," in *Proc. European Conference on Optical Communication (ECOC)*, 2016.

[126] M. Chagnon, M. Osman, M. Poulin, C. Latrasse, J.-F. Gagné, Y. Painchaud, C. Paquet, S. Lessard, and D. Plant, "Experimental study of 112 Gb/s short reach transmission employing PAM formats and SiP intensity modulator at 1.3 μm," *Optics Express*, vol. 22, no. 17, pp. 21 018–21 036, 2014.

[127] K. Zhong, X. Zhou, Y. Gao, W. Chen, J. Man, L. Zeng, A. P. T. Lau, and C. Lu, "140-Gb/s 20-km transmission of PAM-4 signal at 1.3 for short reach communications," *IEEE Photonics Technology Letters*, vol. 27, no. 16, pp. 1757–1760, 2015.

[128] H. Mardoyan, M. A. Mestre, R. Rios-Müller, A. Konczykowska, J. Renaudier, F. Jorge, B. Duval, J.-Y. Dupuy, A. Ghazisaeidi, P. Jennevé *et al.*, "Single carrier 168-Gb/s line-rate PAM direct detection transmission using high-speed selector power DAC for optical interconnects," *Journal of Lightwave Technology*, vol. 34, no. 7, pp. 1593–1598, 2016.

[129] H. Yamazaki, M. Nagatani, S. Kanazawa, H. Nosaka, T. Hashimoto, A. Sano, and Y. Miyamoto, "160-Gbps Nyquist PAM4 transmitter using a digital-preprocessed analog-multiplexed DAC," in *Proc. European Conference on Optical Communication (ECOC)*, 2015, pp. 1–3.

[130] M. Chagnon, S. Lessard, and D. Plant, "336 Gb/s in direct detection below KP4 FEC threshold for intra data center applications," *IEEE Photonics Technology Letters*, vol. 28, no. 20, pp. 2233–2236, 2016.

[131] R. Smith and S. Personick, "Receiver design for optical fiber communication systems," in *Semiconductor devices for optical communication.* Springer, 1980, pp. 89–160.

[132] M. Birk, L. E. Nelson, G. Zhang, C. Cole, C. Yu, M. Akashi, K. Hiramoto, X. Fu, P. Brooks, A. Schubert, T. Baldwin, R. Luking, and G. Pepper, "First 400GBASE-LR8 interoperability using CFP8 modules," in *Proc. Optical Fiber Communication Conference (OFC)*, 2017, p. Th5B.7.

[133] N. Eiselt, J. Wei, H. Griesser, A. Dochhan, M. H. Eiselt, J.-P. Elbers, J. J. V. Olmos, and I. T. Monroy, "First real-time 400G PAM-4 demonstration for inter-data center transmission over 100 km of SSMF at 1550 nm," in *Proc. Optical Fiber Communication Conference (OFC).* Optical Society of America, 2016, p. W1K.5.

[134] K. Zhong, W. Chen, Q. Sui, J. Man, A. P. T. Lau, C. Lu, and L. Zeng, "Experimental demonstration of 500Gbit/s short reach transmission employing PAM4 signal

and direct detection with 25Gbps device," in *Proc. Optical Fiber Communication Conference (OFC)*, 2015, pp. Th3A–3.